

ALMA MATER STUDIORUM · UNIVERSITÀ DI BOLOGNA

SCUOLA DI SCIENZE

Corso di Laurea Magistrale in Matematica

**NONSMOOTH NONCONVEX
VARIATIONAL RECONSTRUCTION
FOR ELECTRICAL IMPEDANCE
TOMOGRAPHY**

Relatore:

**Chiar.ma Prof.ssa
SERENA MORIGI**

Correlatori:

Dott.

MARTIN HÚSKA

Dott.

ANDREA SAMORÈ

Presentata da:

**GABRIELE L. G.
SCRIVANTI**

Sessione Unica

Anno Accademico 2018-2019

Pensa Libero
Chi Saresti

Contents

Introduction	1
1 Applications of EIT	5
2 Mathematical models in EIT	11
2.1 Forward problem	11
2.1.1 Existence and Uniqueness	15
2.1.2 Stimulation Patterns	16
2.1.3 The Forward Operator and the Sensitivity	18
2.2 Inverse problem	21
2.2.1 On the conditioning of the linear inverse problem	25
3 Numerical Methods for EIT	33
3.1 The spatial domain discretization	33
3.2 Finite Elements Method (FEM) for forward EIT problem	34
3.3 Compute of the Jacobian Matrix in EIDORS	38
3.4 Numerical Methods for inverse EIT problem	40
3.4.1 Truncated Singular Value Decomposition (TSVD)	40
3.4.2 The Gauss-Newton method for NLLS	41
3.4.3 Discretization of the Total Variation penalty term	42
3.4.4 Solving Model EIT-L (RL)	44
3.4.5 Solving Model EIT-NL-R	45
3.4.6 Newton One-Step Error Reconstruction (NOSER)	47
3.4.7 A Primal Method with TV: Lagged Diffusivity	49

3.4.8	A Primal-Dual method with TV: PD-IPM	50
3.5	Numerical Methods in EIDORS	52
4	Numerical Tests	55
4.1	The 2D setup	55
4.2	Error Metric	58
4.3	Experimental results	60
5	A Spatially-Adaptive Variational Method for EIT	79
5.1	Variational Model	80
5.2	Discretization	81
5.3	Spatially varying η function	84
5.4	Applying ADMM to the proposed model	85
5.4.1	Solving the sub-problem for \mathbf{t}	87
5.4.2	Solving the sub-problem for $\boldsymbol{\sigma}$	89
5.4.3	Special Case	90
5.4.4	SAEiT $_{\eta}$: an ADMM-type algorithm	90
6	Numerical Experiments	93
6.1	Adding Noise to the simulated data	94
6.2	Example 1: SAEiT $_0$ vs PDIPM	96
6.3	Example 2: Benefit of η -map	98
6.4	Example 3: SAEiT $_{\alpha}$ vs IGNL	102
6.5	Example 4: Reconstruction of noisy data	103
6.6	Example 5 - Image Fusion	106
	Conclusions	117

Introduction

Electrical Impedance Tomography is an imaging technique that aims to reconstruct the inner conductivity distribution of a medium starting from a set of measured voltages registered by a series of electrodes that are positioned on the surface of the medium. As Bayford reports in [5], such technique was used for the first time in geological studies in 1930 and then applied to industrial procedures such as detection of air bubbles in pipes or monitoring of mixing processes. The first clinical use of EIT dates back to 1987. The promising advantages of this imaging procedure over X-Ray, CT and MRI are the fact that the device can be brought to the patient and no exposition to radiation is required for data collection. Examples of clinical applications where EIT has been applied are: lung ventilation imaging, detection of pulmonary emboli in lungs, cardiac output measuring, detection of breast cancer, localization of epileptic foci and imaging of functional activity in human brain. In 2018 Wu *et alia* validated the use of EIT in tissue engineering as an imaging and monitoring tool for cell distribution (cell growth, differentiation and tissue formation) in 3D scaffolds [38]. The main advantages are the possibility to monitor tissue formation with no need to cut, fix or operate histology staining on the sample (which would make the sample useless for further studies) as state of the art techniques require, and a real-time and label-free valuation of cell growth in large samples.

EIT problem can be split into a Forward and an Inverse problem. The aim of Forward EIT is to define the set of measured voltages starting from a

known conductivity distribution. The model for the forward problem, known as *Complete Electrode Model*, is based on an elliptic partial differential equation subject to a set of constraints and Neumann boundary conditions that account for the fitting with real data, discreteness of the electrodes and the extra parameters defined by the measuring devices. Existence and Uniqueness for the forward problem have been proved by Sommersalo, Cheney and Isaacson [31]. If the forward problem is characterized by a nonlinear mapping, called *Forward Operator*, from the conductivity distribution to the measured voltages, inverse EIT consists of inverting the Forward Operator. This leads to an ill-posed problem which requires regularization, either in the model or in the numerical method that is applied to define the solution. The inverse problem is modelled as a Nonlinear Least Squares problem, where one seeks to minimize the mismatch (generally defined as the L_2 norm of the difference) between the measured voltages and the ones generated by the reconstructed conductivity. Some applications demand the reconstruction of a small conductivity change between two states and they therefore rely on a linearized version of the problem. Reconstruction techniques require the introduction of a regularization term which forces the reconstructed data to stick to certain prior information. Such terms can either be linear or nonlinear. Common choices in the former case are the L_2 norm of the conductivity or L_2 norm of a partial differential operator L applied to conductivity; the most common choice in the latter case is the Total Variation functional.

In this dissertation, some state-of-the-art regularization methods are analyzed and compared via EIDORS [4], a specific software for EIT problems. In particular a Newton one-step algorithm for nonlinear EIT problem (NOSER,[15]), the Gauss-Newton's method with different linear regularization terms, a Primal (IRLS, [8]) and a Primal-Dual (PD-IPM, [9]) approach to Total Variation regularization are considered. The aim is to reconstruct the variation in conductivity within a 2D section of a 3D scaffold. Furthermore a variational formulation on a 2D mesh for a space-variant regularization is

proposed, based on a combination of high order and nonconvex operators, which respectively seek to recover piecewise inhomogeneous and piecewise linear regions.

Keywords: Electrical Impedance Tomography, Inverse Conductivity Problem, Finite Elements, Regularization Methods, Total Variation, Medical Imaging, Tissue Engineering, EIDORS, Alternating Direction Method of Multipliers

Chapter 1

Applications of EIT

Electrical Impedance Tomography (EIT) is an imaging technique that aims to reconstruct the inner conductivity distribution of a medium starting from a set of measured voltages registered by a series of electrodes that are positioned on the surface of the medium. Electrical impedance is defined as the measure of the opposition that a circuit presents to a current when a voltage is applied. EIT is therefore a nondestructive testing technique, meaning that it allows to analyse the property of a material or structure without causing damage. If compared to other tomography techniques, EIT provides lower spatial resolution outputs, but data can be acquired relatively fast (EIT temporal resolution is estimated in the order of millisecond [5]) and the apparatus is more manageable. Its name was agreed in 1986 during the first Sheffield meeting, after electrical impedance measurements being the source data for the images, even though it can be considered a tomographic modality only due the fact that it generates images of the internal features of a body: the diffuse propagation of electric current does not allow for independent slice by slice imaging (as on the contrary holds for true tomographic imaging methods) since a change in conductivity anywhere inside the medium influences all measurements.

The first recorded use of EIT was in geology and dates back to 1930,

when Stefanescu in [32] studied the problem of the distribution of potentials inside horizontal, homogeneous and isotropic layers of land around a punctual electrical grounding. Modern examples of EIT application in geophysics are described in [22]. Rock impedance varies of several orders depending on the rock nature, its porosity and water content: this allows to image the inner structures of geological objects and study e.g. the impact of excavation on clay properties or the hydrothermal conduits inside volcanoes. The different electrical properties of the components of a multiphase flow let EIT be exploited in industrial applications, such as the detection of air bubbles in process pipes or the monitoring of mixing processes. Despite its low spatial resolution, EIT proved to be more suitable than other tomographic techniques in these fields because of the rapidity of data collection, given the necessity to observe a temporally evolving medium.

In this thesis the focus is on the application of EIT in biomedical imaging, based on the measurement of biological tissues impedance. These measurements are dependant on the amount of body fluids on one side and cell size, orientation and membrane thickness on the other. Measurements can be made over a range of low (20 Hz) to high (1 MHz) frequencies and different physiological mechanisms can be identified depending on the frequency range. When current is applied to the electrodes, an electric field is induced inside the biological medium and this causes ions to move: as shown in Figure 1.1, at low frequencies ions travel around cell membranes whereas at high frequencies they move across those membranes at a variety of scales that depend on the wavelength of the field [36]. Hence, the state of the art applications of EIT in biomedical imaging range from clinical imaging for organ monitoring to cell monitoring in tissue engineering.

The first clinical use of EIT was performed in 1987 by the Sheffield group to produce images of pulmonary function [13]. The promising advantages of this imaging technique over X-Ray, CT and MRI are the fact that the device can be brought to the patient and no exposition to radiation is required

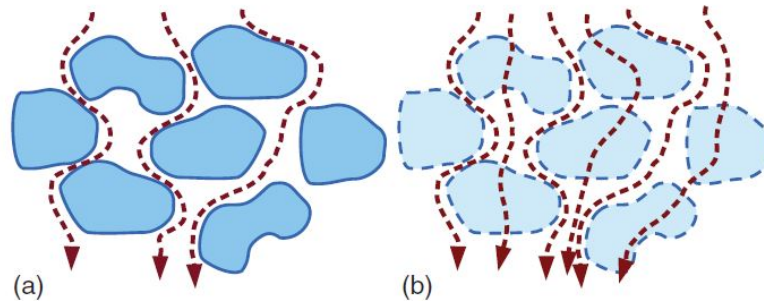


Figure 1.1: Low-frequency (a) and high-frequency (b) current flows through a biological medium following different paths according to the wavelength of the electric field.

for data collection. Bayford summarises in [5] the main clinical application where EIT has been exploited with varying degrees of success:

- **Pulmonary Functions:** EIT can be used to image lung ventilation, to detect blood clots in the lungs or pulmonary emboli and to monitor the drainage of a pneumothorax (abnormal collection of air in the pleural space between the lung and the chest wall) caused by pulmonary lesions;
- **Breast Tumors:** the electrical properties of many tumors, especially those presenting malignancy, differ from the surrounding tissues;
- **Gastrointestinal Function:** monitoring gastric emptying allows to diagnose many functional disorders of the gastrointestinal tract without using radioactive isotopes as required by gamma scintigraphy or make the patient swallow a nasogastric tube as required by intubation;
- **Brain Imaging:** EIT can be used to accurately localize the epileptic focus before surgical excision in patients suffering from intractable epilepsy and to image functional activity in human brain.

Tissue engineering investigates how to generate artificial tissues and organs in order to restore or replace damaged tissues in body. Part of the research is to assess cell viability and proliferation in samples with dimensions at the

millimeter scale. Some of the most popular techniques in this field are Scanning Electron Microscopy (SEM), Transmission Electron Microscopy (TEM) and Micro Computed Tomography. The problem with them is that they require to work on the tissue in a way that make it useless for further research. On the other side, alternative techniques that avoid this issue are time consuming and make use of fluorescent or radioactive labels. One technique for cell differentiation and growth monitoring that meets the requirements of being noninvasive and label-free is Dielectric Spectroscopy (DS): it exploits the electrical properties of cells, from which it is possible to infer cell viability, but it suffers from low spatial resolution since it only provides a lumped impedance value for a whole sample of a cellular culture. Sharing the same theory of DS, EIT was firstly introduced for *in vitro* experiments in tissue engineering in 2006 to monitor cell migration and epithelial stratification [23]. In 2018 Wu *et alia* validated the use of EIT in tissue engineering as an imaging and monitoring tool for sparse cell distribution, growth and tissue formation [38].

In 2019 EIT was suggested for the monitoring of the mineralization and for the non-invasive characterization of tissue engineered bone surrogates as the deposition of calcium during osteogenic differentiation affects the electric properties of the tissues [17]. Figure 1.2 shows a comparison between an analysis conducted via Alizarin red (an existing destructive staining technique for quantifying calcium deposition) and a simulation with EIT: increasing values of Alizarin red concentration showed to reflect a decrease in average conductivity.

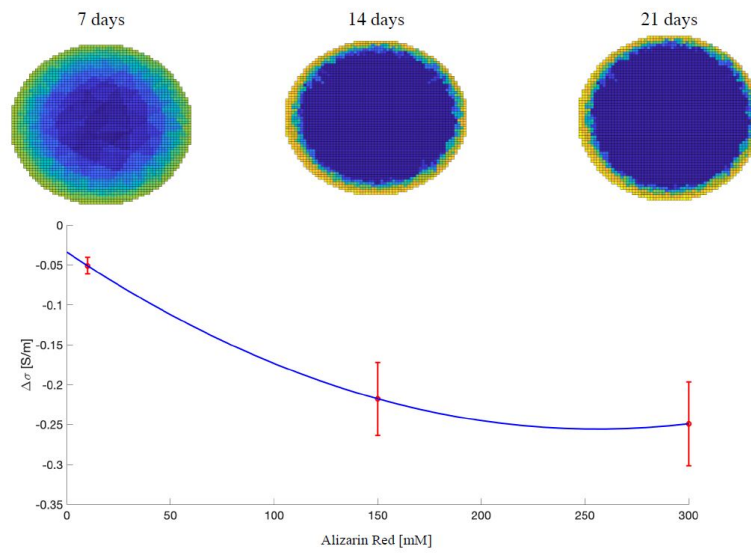


Figure 1.2: Conductivity reconstruction and comparison with Alizarin Red concentration

Chapter 2

Mathematical models in EIT

2.1 Forward problem

Let $\Omega \subset \mathbb{R}^d$, $d = 2, 3$ be a bounded simply connected C^∞ domain and

$$\sigma : \Omega \rightarrow \mathbb{R}$$

a $C^2(\Omega)$ function strictly bounded from below by zero ($\sigma(x) > 0$). The electric potential or voltage u in the body $\Omega \subset \mathbb{R}^d$, $d = 2, 3$ is governed by the elliptic partial differential equation

$$\nabla \cdot (\sigma(x) \nabla u(x)) = 0 \quad \text{on } \Omega \tag{2.1}$$

(where σ represents the electric conductivity), $x \in \Omega$, and can be constrained by the following Dirichlet Boundary Condition on the Ω interface (curve or surface) $\partial\Omega$ of the body

$$u(x) = V(x) \quad \text{on } \partial\Omega. \tag{2.2}$$

Currents are applied to electrodes on $\partial\Omega$ and these currents produce a current density \mathbf{j} on the Ω interface whose inward pointing component is expressed

2. Mathematical models in EIT

as I . Then the Neumann boundary condition is

$$\sigma(x) \frac{\partial u(x)}{\partial n} = I(x) \quad \text{on } \partial\Omega. \quad (2.3)$$

where $-\mathbf{j} \cdot \mathbf{n} = I$ on $\partial\Omega$. The current density \mathbf{j} and the electric potential u are related by Ohm's Law

$$\mathbf{j}(x) = -\sigma(x) \nabla u(x). \quad (2.4)$$

Equations (2.1) and (2.3), together with two additional conditions, namely the *conservation of charge*

$$\int_{\partial\Omega} I dS = 0 \quad (2.5)$$

and the *choice of a reference voltage* (which ensures the existence of a unique solution of the Neumann Boundary Problem)

$$\int_{\partial\Omega} u dS = 0 \quad (2.6)$$

define a model for EIT which is known as *continuum model*. As described in [7], in this framework a pair of maps, namely the Dirichlet to Neumann (DtN) map and the Neumann to Dirichlet (NtD) map are defined to relate $V(x)$ and $I(x)$. The DtN map $\Lambda_\sigma : H^{\frac{1}{2}}(\partial\Omega) \rightarrow H^{-\frac{1}{2}}(\partial\Omega)$ is defined as

$$\Lambda_\sigma V(x) = \sigma(x) \frac{\partial u(x)}{\partial n} \quad \text{on } \partial\Omega \quad (2.7)$$

and has a nullspace $\mathcal{N}(\Lambda_\sigma) = \{V = \text{constant}\}$. On the other side the NtD map is the generalized inverse of the DtN map $(\Lambda_\sigma)^{-1} : \mathfrak{J} \rightarrow H^{\frac{1}{2}}(\partial\Omega)$ defined as

$$(\Lambda_\sigma)^{-1} I(x) = u(x) \quad \text{on } \partial\Omega \quad (2.8)$$

where $\mathfrak{J} = \{I \in H^{-\frac{1}{2}}(\partial\Omega) \mid \int_{\partial\Omega} I dS = 0\}$ is the set of admitted current, in accordance to (2.6).

The problem with the continuum model is that \mathbf{j} is unknown, which makes it unuseful for real experiments. One attempt to overcome this issue is the so called, *shunt model*, where two effects are accounted for: the first one is the discreteness of the L electrodes, which are modelled as a family of subsets of $\partial\Omega$:

- Boundary with electrodes

$$\Gamma = \bigcup_{l=1}^L E_l \subset \partial\Omega, \quad (2.9)$$

- Boundary without electrodes

$$\tilde{\Gamma} = \partial\Omega \setminus \bigcup_{l=1}^L E_l \quad (2.10)$$

where E_l is the measure (length for $n = 2$ or area for $n = 3$) of element l of the boundary $\delta\Omega$.

The quantity $\sigma \frac{\partial u}{\partial n}|_{\partial\Omega}$ represents the current density on the boundary. We then replace (2.3) by two weaker conditions

$$\int_{E_l} \sigma \frac{\partial u}{\partial n} dS = I_l, \quad l = 1, \dots, L \quad \text{on } \Gamma \quad (2.11)$$

and since $\mathbf{j} = 0$ for the current density on the boundaries between the electrodes (on $\tilde{\Gamma}$) we have

$$\sigma \frac{\partial u}{\partial n} = 0 \quad \text{on } \tilde{\Gamma} \quad (2.12)$$

where I_l is the known current that is sent to the l th electrode E_l .

The second effect is the extra conductive material that is added to the set by the electrodes, which is assumed to be a perfect conductor so that the

2. Mathematical models in EIT

potential on the electrode is constant

$$u = V_l \quad \text{on } E_l, l = 1, \dots, L. \quad (2.13)$$

The problem with this second model is that it gives results that do not agree with experimental data: the reason is that there is an extra resistance (due to an electrochemical effect) between the electrode and the tank that has not been accounted for yet, *id est* the formation of a thin, highly resistive layer. The impedance of the layer for the l th electrode is defined by a parameter z_l that is called *effective contact impedance*. Equation (2.13) is therefore replaced by Robin boundary conditions

$$u + z_l \sigma \frac{\partial u}{\partial n} = V_l \quad \text{on } E_l \quad l = 1, \dots, L. \quad (2.14)$$

Eventually the two additional conditions (2.15) and (2.16) that complete the model can be discretely formulated as *conservation of charge*

$$\sum_{l=1}^L I_l = 0 \quad (2.15)$$

and *choice of a reference voltage*

$$\sum_{l=1}^L V_l = 0. \quad (2.16)$$

The resulting model, composed by (2.1), (2.11), (2.12), (2.14), (2.15) and (2.16) is known as *complete electrode model* (CEM) [31].

We notice that I and V are experimentally connected by a linear relation

$$V = RI$$

where matrix $R \in \mathbb{R}^{L \times L}$ is defined as *resistance matrix* [31].

2.1.1 Existence and Uniqueness

Sommersalo, Cheney and Isaacson proved in [31] the existence and uniqueness of the solution to problem (CEM). Such solution needs to be searched in specific functional space that accounts for both the electric potential inside Ω and the voltages on $\partial\Omega$:

$$H = H^1(\Omega) \oplus \mathbb{C}^L.$$

For functions in H it is possible to define a sesquilinear form $B : H \times H \rightarrow \mathbb{C}$

$$B((u, U), (v, V)) = \int_{\Omega} \sigma \nabla u \cdot \nabla \bar{v} d\Omega + \sum_{l=1}^L \frac{1}{z_l} \int_{E_l} (u - U_l)(\bar{v} - \bar{V}_l) dS,$$

for which holds the following result:

Proposition 2.1. $(u, U) \in H$ satisfies

$$B((u, U), (v, V)) = \sum_{l=1}^L I_l \bar{V}_l$$

for any $(v, V) \in H$ if and only if u is a weak solution of (2.1) and (u, U) satisfies the constraints of the problem (2.14).

In order to get uniqueness and existence, Lax-Milgram lemma needs to be applied. To such end it is necessary to remark that voltages are defined up to a constant and that $B((u, U), (u, U)) = 0$ does not imply $(u, U) = 0$ but $u = \text{const} = U_1 = \dots = U_L$, which advise to consider a quotient space

$$\dot{H} = H/\mathbb{C}$$

where two equivalent norms can be defined: the usual quotient norm

$$\|(u, U)\| = \inf_{c \in \mathbb{C}} (\|u - c\|_{H^1(\Omega)}^2 + \|U - c\|_{\mathbb{C}^L}^2)^{1/2} \quad (\text{N1})$$

and a norm which makes it easier to prove that B satisfies Lax-Milgram's

hypothesis

$$\|(u, U)\|_* = (\|\nabla u\|_{L^2(\Omega)} + \sum_{l=1}^L \int_{E_l} |u(x) - U_l|^2 dS)^{1/2} \quad (\text{N2})$$

Theorem 2.2. *Suppose that there are strictly positive constants σ_0 and σ_1 and Z such that*

$$|\sigma| \leq \sigma_1, \quad (2.17)$$

$$\text{Re}\sigma \geq \sigma_0, \quad (2.18)$$

and

$$\text{Re}z_l > Z \text{ for } l = 1, \dots, L. \quad (2.19)$$

Then for a given current pattern $(I_l)_{l=1}^L$ satisfying (2.15) there is a unique (u, U) in \dot{H} satisfying

$$B((u, U), (v, V)) = \sum_{l=1}^L I_l \bar{V}_l \quad (2.20)$$

for all $(v, V) \in \dot{H}$

Corollary 2.3. *If the hypothesis in the previous Theorem are satisfied and if*

$$\sum_{l=1}^L U_l = 0,$$

then the complete electrode model has a unique solution.

2.1.2 Stimulation Patterns

The stimulation pattern is the strategy that chooses on which electrodes pairs current injection and voltage measurements are performed in order to define the boundary conditions of the CEM. The pairs of electrodes in which current is injected are defined as *driving* or *injection pairs* and the ones on which the voltages are measured are defined as *measurement pairs*. Aimig to

provide as much information as possible for the retrieval of the inner conductivity distribution, which is the target of the EIT inverse problem that will be presented in the coming sections, one should consider that reconstruction is better where current density is higher: when current is injected among two opposite electrodes, the procedure is defined as *opposite injection* protocol and the maximum current density is found in the centre of the body Ω , while when current is injected among two neighbouring electrodes, the procedure is defined as *adjacent injection* protocol and the maximum current density is found near the electrodes on $\partial\Omega$.

The same choices of electrode pairs can be applied in the process of acquisition of voltage measurements, yielding the so called *opposite* and *adjacent measurement* protocols. When a pair of electrodes is chosen as driving pair, it is usually excluded from the available measuring pairs. Combining the described injection and measurements protocol generates the following stimulation patterns, with different effects on the reconstruction:

- **opposite injection - opposite measurement:** it is not often used because it generates mirror images when target conductivity variations are not positioned in the centre of Ω ;
- **opposite injection - adjacent measurement:** works fine for the reconstruction of regions that are far from the measuring electrodes;
- **adjacent injection - opposite measurement:** not often used but equivalent to the previous pattern;
- **adjacent injection - adjacent measurement:** it works well for the reconstruction of regions that are close to the electrodes.

Figures 2.1a-2.1b show a typical 2D EIT sensor array with $L = 16$ electrodes, *opp inj / adj meas* and *adj inj/adj meas* stimulation patterns in case Ω has a circular shape and $L=16$, where I is the injected current and the V 's are the measured voltages.

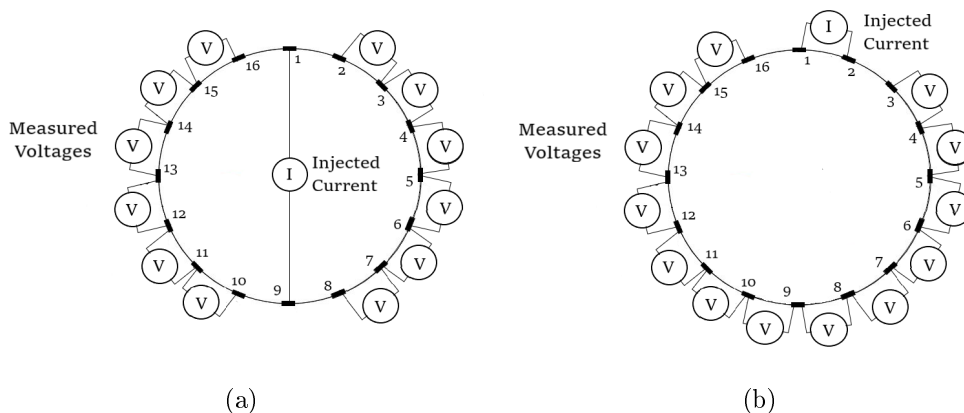


Figure 2.1: EIT sensor arrays with $L = 16$ electrodes. *Opposite injection - adjacent measurement* protocol (a); *Adjacent injection - adjacent measurement* protocol (b).

2.1.3 The Forward Operator and the Sensitivity

The forward problem can be restricted to a relation between the inner conductivity and the boundary voltages and modelled by a mapping which is referred to as *Forward Operator*:

$$\tilde{F}: \mathfrak{S} \rightarrow H \quad (2.21)$$

$$\sigma \mapsto (u, U) \quad (2.22)$$

where $\mathfrak{S} = \{\sigma \in L^\infty(\Omega) \mid \sigma \nabla u = 0\}$. We notice that the operator \tilde{F} is Fréchet differentiable, as stated by Theorem 2.4 from [21]

Theorem 2.4. *The operator \tilde{F} that maps $\sigma \in \mathfrak{S}$ to the solution of the Forward Problem with current vector I is Fréchet differentiable, meaning that*

$$\lim_{\|\delta\sigma\|_\infty \rightarrow 0} \frac{\|\tilde{F}(\sigma + \delta\sigma) - \tilde{F}(\sigma) - \tilde{F}'(\sigma)\delta\sigma\|_H}{\|\delta\sigma\|_\infty} = 0$$

If $\delta\sigma \in L^\infty(\Omega)$ is such that $\sigma + \delta\sigma \in \mathfrak{S}$, then $\tilde{F}'(\sigma)\delta\sigma = (w, W)$ satisfies

the variational problem

$$b((w, W), (v, V)) = - \int_{\Omega} \delta\sigma \nabla u_0 \nabla v d\Omega$$

for all $(v, V) \in H$ where $(u_0, U_0) = \tilde{F}(\sigma)$.

This in particular shows that the mapping $\sigma \mapsto U$ is Fréchet Differentiable for being the second argument of a differentiable mapping [21]. For a given stimulation pattern that yields a total number of measurements n_m , we can therefore define the following experimental version of the Forward Operator:

$$F: \mathfrak{S} \rightarrow \mathbb{R}^{n_m} \quad (2.23)$$

$$\sigma \mapsto V_m[\sigma] \quad (2.24)$$

where $V_m[\sigma]$ is defined as the vector of the measured voltages, whose dimension n_m depends on the choice of a measurement protocol. An adjacent protocol for both measurement and injection is now considered (see Figure 2.1b)

Let the d th injection current be considered, and u_d be the potential subject to it; then u_d satisfies (2.1) and

$$\int_{E_d} \sigma \frac{\partial u_d}{\partial n} dS = I = - \int_{E_{d+1}} \sigma \frac{\partial u_d}{\partial n} dS,$$

where the Neumann boundary conditions are zero for all the boundary regions that are not touched by the driving electrodes. The m th boundary voltage difference related to the d th injection is

$$V_{d,m} = \frac{1}{|E_m|} \int_{E_m} u_d dS - \frac{1}{|E_{m+1}|} \int_{E_{m+1}} u_d dS \quad (2.25)$$

and as a result one can obtain

$$\int_{\Omega} \sigma \nabla u_d \cdot \nabla u_m d\Omega = \int_{\partial\Omega} \sigma u_d \frac{\partial u_m}{\partial n} dS = V_{d,m} \quad (2.26)$$

2. Mathematical models in EIT

where clearly $V_{d,m} = V_{m,d}$: this is due to the reciprocal property of the electric field, for which if $\{d, m\}$ is a data collection pattern, its reciprocal, consisting of interchanged current injection and voltage measurement terminals, is $\{m, d\}$. This property can be helpful for avoiding redundant measurements. In conclusion V_m is uniquely defined by the distribution of σ . The Forward Operator then, for $L = 16$, is

$$F(\sigma) := \left[V_{1,3} \quad V_{1,4} \quad \dots \quad V_{1,15} \quad V_{2,4} \quad V_{2,5} \quad \dots \quad V_{16,14} \right]^T \in \mathbb{R}^{n_m}. \quad (2.27)$$

where $n_m = L(L - 3) = 16 \cdot 13 = 208$.

Any change in σ influences all potential values and the boundary voltages are then entangled with the global structure of the conductivity in a nonlinear way [29]. The influence of a conductivity change in a region of the domain on the potential in another region is weaker and weaker as the distance increases, but is also affected by the conductivity changes in all the other regions.

The *sensitivity* of a boundary voltage to a change in conductivity can be estimated by means of a perturbation procedure, as described in [28]. Let σ be the conductivity distribution on domain Ω that generates the measured data $F(\sigma)$, and σ_0 be a reference conductivity distribution which generates the computed data $F(\sigma_0)$ and minimizes $\|F(\sigma) - F(\sigma_0)\|_2$. If the same current is assumed to be injected in the two domains, then $\delta\sigma = \sigma - \sigma_0$ satisfies

$$\begin{aligned} \int_{\Omega} \delta\sigma \nabla u_m \cdot \nabla u_d^0 d\Omega &= \int_{\Omega} \sigma \nabla u_m \cdot \nabla u_d^0 dx - \int_{\Omega} \sigma_0 \nabla u_m \cdot \nabla u_d^0 d\Omega = \\ &= \int_{\partial\Omega} \sigma \frac{\partial u_m}{\partial n} u_d^0 dS - \int_{\partial\Omega} \sigma_0 u_m \frac{\partial u_d^0}{\partial n} dS = \\ &= -(V_{d,m}[\sigma] - V_{m,d}[\sigma_0]) = \\ &= -(V_{d,m}[\sigma] - V_{d,m}[\sigma_0]). \end{aligned}$$

We therefore defined in this way the Fréchet derivative of the measured

voltages on the electrodes with respect to a perturbation in conductivity.

The computation of the Jacobian matrix require a discretization of the conductivity. Let then Ω be discretized into n_T subdomains $\{T_j\}_{j=1}^{n_T}$ and let σ , σ_0 and $\delta\sigma$ be assumed constant on each of them, so that σ , σ_0 and $\delta\sigma \in \mathbb{R}^{n_T}$, and the previous identity can be assembled into matrix form as

$$J \delta\sigma = -(F(\sigma) - F(\sigma_0)) \quad (2.28)$$

where $J \in \mathbb{R}^{n_m \times n_T}$ is the Jacobian Matrix which is defined as

$$\{J\}_{i,j} = \frac{\partial V_{d,m}}{\partial \sigma_j} = \int_{T_j} \nabla u_d \cdot \nabla u_m d\Omega. \quad (2.29)$$

Index i of the rows of the matrix is defined by the stimulation pattern and depends on the indices of the driving and measuring pair $\{d, m\}$. Index j of the columns of the matrix corresponds to the subdomain T_j .

2.2 Inverse problem

EIT inverse problem aims to define the conductivity σ inside the body Ω starting from the measured voltages V_m on the boundary $\partial\Omega$. Considering the nonlinear relation among V_m and σ defined by the Forward Operator, the simplest way to fit the data is to consider the so called *least squares* approach [19]

$$\sigma^* = \underset{\sigma}{\operatorname{argmin}} f(\sigma), \quad f(\sigma) := \frac{1}{2} \|F(\sigma) - V_m\|_2^2 \quad (\text{EIT-NL})$$

which consists in minimizing the fidelity term $f(\sigma)$. Being F a nonlinear operator Gauss-Newton method is the first method that one might consider to solve (EIT-NL) as a nonlinear least squares problem.

The issue with such technique is that (EIT-NL) is ill posed due to its instability, since small errors in the measured data may generate large errors

2. Mathematical models in EIT

in the reconstructed conductivity, as described by Calderon in [14], where the uniqueness of the EIT inverse problem was discussed for the first time. Such behaviour is caused by the combination of high sensitivity of the measurements to changes in the conductivity in the areas near the surface and, on the other side, low sensitivity to changes in areas deep within the body. It can be labeled as a *severly ill-posed* problem (according to the definition given by [19] based on the decay of the singular values of the operator), which can be seen by considering the behaviour of the singular values of the discrete linear approximation of the Forward Operator. In order to regularize the solution, a penalty term $G(\sigma)$ needs to be added to the objective function so that highly oscillatory conductivities can be handled:

$$\sigma^* = \underset{\sigma}{\operatorname{argmin}} \left\{ f(\sigma) + \alpha G(\sigma) \right\} \quad (\text{EIT-NL-R})$$

This new formulation can be addressed to as the *regularized problem*, where $\alpha > 0$ is the regularization parameter that controls the trade-off amidst data fitting and bounding the derivatives of σ . The penalty term can also be seen as including *a priori* information about the conductivity, so it is generally defined as *prior*. A possible choice for the *prior* is a linear term within a quadratic norm framework

$$G(\sigma) = \|L(\sigma - \sigma_{ref})\|_2^2 \quad (\text{RL})$$

where L is a matrix that approximates a partial differential operator and σ_{ref} a prior estimate of the conductivity distribution. If one assumes independence for image elements and the same expected value for magnitude, then matrix L turns into an identity matrix I , which yields a zeroth-order Tikhonov regularization [1]. Vauhkonen in [35] suggested to consider a discrete Laplacian filter if it is desired to model image smoothness, so that a penalty for nonsmooth regions in the conductivity is gained. A third choice for L could be a discrete high pass Gaussian Filter for spacial frequencies, as suggested by Adler and Guardo in [3]. By doing so, one penalizes high fre-

quency components, thus gaining better conditioning, but at the same time worse resolution for the reconstructed image.

The regularization operator can also be chosen to be nonlinear, where the most common choice in this case is the *Total Variation (TV)* functional as suggested by Borsic [8]:

$$G(\sigma) = TV(\sigma). \quad (\text{RNL})$$

The Total Variation functional of a conductivity function σ is defined as

$$TV(\sigma) = \int_{\Omega} |\nabla\sigma| d\Omega.$$

The use of Total Variation as a l^1 regularization penalty term allows to preserve discontinuities in the reconstructed conductivity. As described in [9], such discontinuities can be found in almost every field where EIT has been applied: in medicine, where they are defined by intern organ boundaries, as each organ has different electric features, or in process tomography where they are defined by the different phase interfaces of a multiphasic fluid. This precision and allowance for discontinuous profiles is though gained at the cost of losing differentiability for the objective function, since penalty term includes an absolute value. Such a framework forces to consider nonsmooth optimization methods.

A linear model for the inverse problem can be built considering the linearization of the nonlinear Forward Operator F for a small change about an initial conductivity distribution σ_0 (which may differ from σ_{ref}) $\delta\sigma := \sigma - \sigma_0$:

$$F(\sigma) \approx F(\sigma_0) + \nabla_{\sigma} F(\sigma_0) \delta\sigma,$$

where $\nabla_{\sigma} F(\sigma_0)$ is the Jacobian matrix at σ_0 $J(\sigma_0)$ defined in (2.29). By defining $\delta V_m := F(\sigma_0) - V_m$ the nonlinear Least Squares model (EIT-NL) can be approximated by the following linear Least Squares model

2. Mathematical models in EIT

$$\delta\sigma^* = \operatorname{argmin}_{\delta\sigma} \bar{f}(\delta\sigma), \quad \bar{f}(\delta\sigma) := \frac{1}{2} \|J\delta\sigma - \delta V_m\|_2^2. \quad (\text{EIT-L})$$

It is important to highlight the fact that the linearization of the problem yields an underdetermined system of equations, which is by definition ill-posed as it either lacks of a solution or allows infinitely many solutions. Regularization is then required. The regularized associated model with linearized fidelity $\bar{f}(\delta\sigma)$ is:

$$\delta\sigma^* = \operatorname{argmin}_{\delta\sigma} \left\{ \bar{f}(\delta\sigma) + \alpha G(\delta\sigma) \right\}, \quad (2.30)$$

which can be classified into two optimization models according to the penalty term being linear

$$\delta\sigma^* = \operatorname{argmin}_{\delta\sigma} \left\{ \|J\delta\sigma - \delta V_m\|_2^2 + \alpha \|L\delta\sigma - L\sigma_{ref}\|_2^2 \right\} \quad (\text{EIT-L (RL)})$$

or nonlinear

$$\delta\sigma^* = \operatorname{argmin}_{\delta\sigma} \left\{ \|J\delta\sigma - \delta V_m\|_2^2 + \alpha TV(\delta\sigma) \right\} \quad (\text{EIT-L (RNL)})$$

Remark 2.5. The different notation σ and $\delta\sigma$ aims to underline the fact that the former represents an absolute conductivity distribution while the latter represents a relative change of conductivity distribution at a posterior state with respect to an initial state with conductivity distribution σ_0 . Linearized models are generally involved in the reconstruction of such conductivity change $\delta\sigma$. The idea of computing the difference in conductivity between two states might be of interest to many applications, as in medical problems. This is known as *difference imaging* and the contrast might though be larger than required by linear approximation [24]. The solution to such issue may be found in iteratively solving a regularized linear approximation of the problem, where at each iteration a small conductivity change $\delta\sigma_n = \sigma_{n+1} - \sigma_n$ is sought and a new computation for the Jacobian

is performed.

Remark 2.6. From this point onwards only *difference imaging* will be considered and for simplicity of notation σ will be regarded to as conductivity difference and V_m as voltage difference.

2.2.1 On the conditioning of the linear inverse problem

The ill-posed nature of the linearized problem arises from the fact that for a given injection current, the number of measurements is limited and generally smaller than the number of subdomains, which corresponds to the number of components of the unknown vector σ . Furthermore, some measurements might be redundant because some of the voltages might be defined by reciprocity and thus be bounded by linear relation. These two facts result in the problem being underdetermined and the jacobian matrix being rank deficient. As the number of subdomains increases, the reconstruction of the conductivity becomes more challenging, so, as stated in [29], given a number L of electrodes, the amount of information is limited and the effort in improving the spacial resolution generally translates into worsening the ill-posedness of the problem.

Let us consider the simplified linear model w.r.t. (EIT-L):

$$\delta\sigma^* = \operatorname{argmin}_{\delta\sigma} \frac{1}{2} \|J\delta\sigma - \delta V_m\|_2^2. \quad (2.31)$$

The Singular Values Decomposition of J (the conditioning of the matrix J can be characterized in terms of this decomposition) is of the form

$$J = U\Sigma V^T = \sum_{i=1}^k u_i s_i v_i^T \quad (2.32)$$

where $U = (U_1, \dots, U_m)$ and $V = (V_1, \dots, V_n)$ are orthonormal matrices $U^T U = I_m$, $V^T V = I_n$ and $\Sigma = \operatorname{diag}(\lambda_1, \dots, \lambda_n)$ is a diagonal matrix with

nonnegative entries ordered such that

$$s_1 \geq s_2 \geq \dots \geq s_n \geq 0.$$

Let r be the rank of J , $r \leq n$. The ill-posedness of the problem is shown by the singular values rapidly decaying to zero without any particular gap in the singular values. We have

$$s_1 \geq \dots \geq s_r \geq \varepsilon \geq s_{r+1} \geq \dots \geq s_n \geq 0.$$

If ε denotes the threshold for which the singular values are numerically zeros, then singular values $\{s_{r+1}, \dots, s_n\}$ are in practice null. This indicates rank deficiency in the matrix J . Additional information is needed to invert data uniquely. A quantitative measure of ill-posedness is given by the condition number of J

$$\text{cond}(J) = \frac{s_1}{s_k}$$

(where s_k is the smallest nonzero singular value of J) which assumes large values for ill-posed problems and tends to infinity for rank deficient matrix J . In this latter case the matrix J is not invertible.

Starting from the previous considerations, the analysis of the singular values of the Jacobian matrix should yield the following results: only a small number of them is highly above machine precision (and such number corresponds to the rank of the matrix) and the ratio between the first and the last singular values increases as the number of subdomains gets higher.

Example 1

The 2D test setup was composed of a tank with one ring of 16 electrodes; *opposite drive pair* was chosen for both injection and measurement pattern and 3 different structured meshes were considered to model the tank, with a different number of elements $n_T = 1024, 2304, 3136$ which increases the num-

ber of columns of J . The injection pattern for the first drive pair is shown in figure 2.2 and the relative 14 measurement pattern are described in figure 2.3. The total number of measurements is then $M = 16 \times 14 = 224$, which corresponds to the number of rows of the Jacobian matrices.

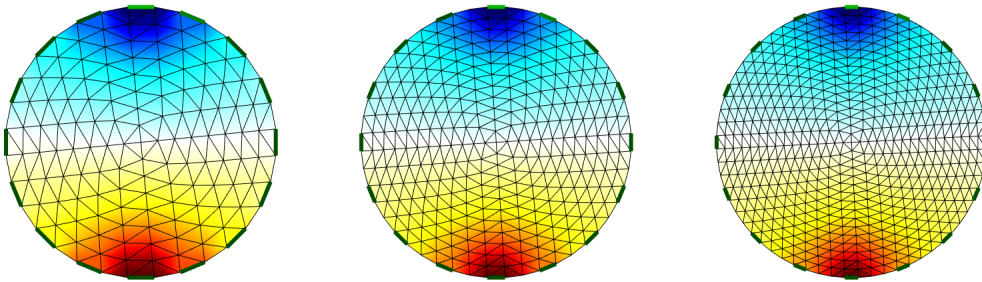


Figure 2.2: **Example 1** Opposite Injection Protocol for the first driving pair. From left to right: $n_T = 1024, 2304, 3136$

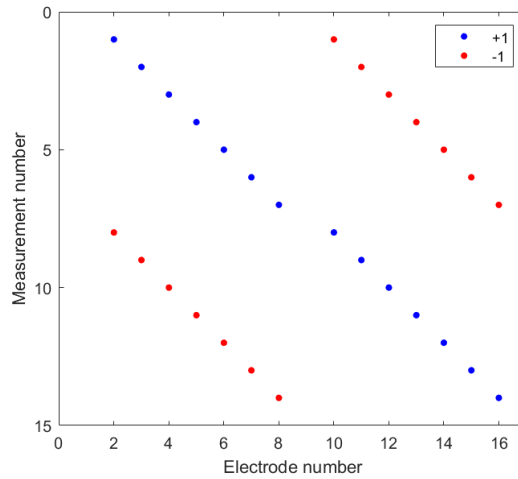


Figure 2.3: **Example 1** Opposite Measurement Protocol for the 14 measurement pairs.

A semicircular object with radius $r = 0.6$ was inserted in the tank, as shown in figure 2.4, with conductivity 1.1 while the background conductivity was set to 1. Voltage measurements were then simulated and the Jacobian

2. Mathematical models in EIT

matrices of the 3 sets were computed. The singular value decomposition performed by function `svd` on the Jacobian matrices of the 3 sets yielded the graphs shown in Figure 2.5 for the singular values. Figure 2.5a shows the decay of all the 224 singular values, which approach 0 before index 50, while Figure 2.5b shows the same values in logarithmic scale and exhibits a clear beforehand jump under machine precision $\epsilon = 0.2204 \times 10^{-16}$. Function `rank` was used to compute the rank of the matrices and yielded $\text{rank}(J_{n_T}) = 28$ for $n_T = 1024, 2304, 3136$ which corresponds to the last index before singular values fall below ϵ . From these results it is possible to conclude that the number n_T of mesh elements does not affect the rank of the Jacobian matrix but it consistently reduces its singular values as it increases.

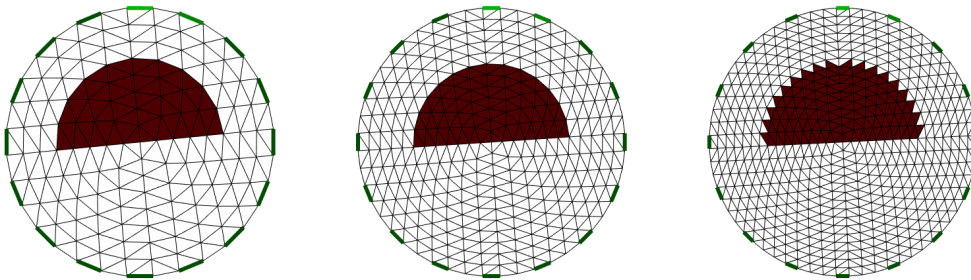
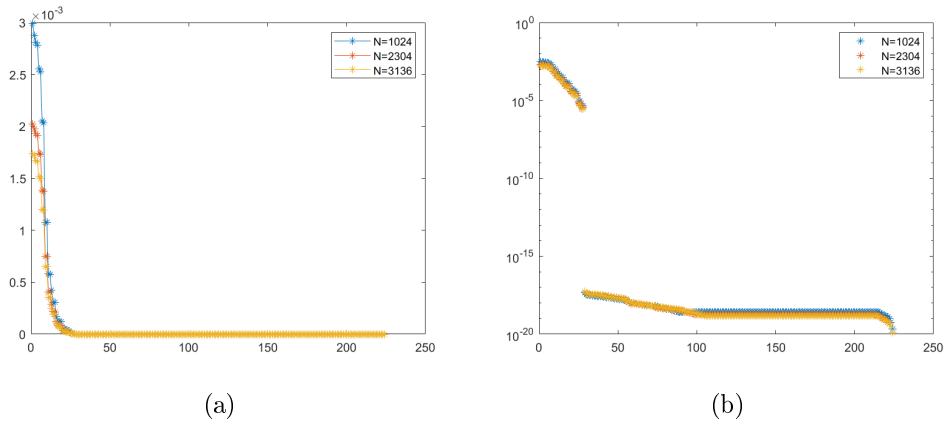


Figure 2.4: **Example 1** Tanks with semicircular element. From left to right: $n_T = 1024, 2304, 3136$.

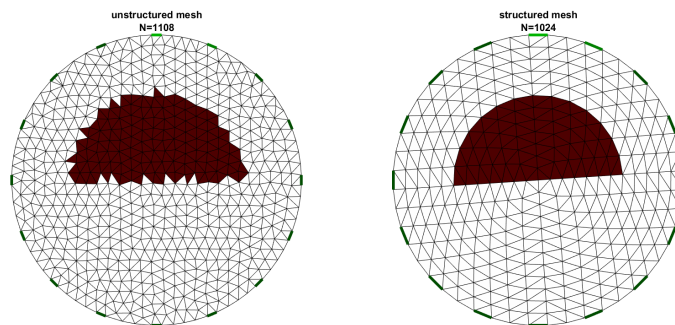
The computation of the condition number for the Jacobian matrices of the 3 sets was carried out by means of MATLAB function `cond`. Values are reported in Table 2.1. Clearly the matrices resulted ill-conditioned and increasing conditioning was found to be correlated with increasing number of elements n_T .

For completeness' sake the setup was also tested on an unstructured mesh with 1108 mesh elements, and for a comparison the third structured mesh case with 1024 elements was considered. The rank of the matrix remained unchanged, thus the choice of the geometry does not seem to affect this prop-

Figure 2.5: **Example 1** Singular Values for the structured meshesTable 2.1: **Example 1** Condition numbers

n_T	$\mathbf{Cond}(J)$
1024	0.1233×10^{36}
2304	0.2087×10^{36}
3136	1.9426×10^{36}

erty of the matrix, while singular values were slightly modified but with no significant changes. The condition number for the unstructured mesh, estimated by MATLAB function `cond`, was 0.18044×10^{36} , which is comparable to the previous case.

Figure 2.6: **Example 1** Tanks with semicircular element.

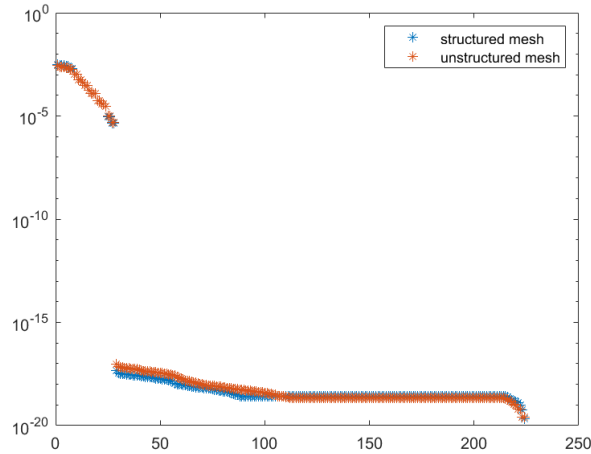
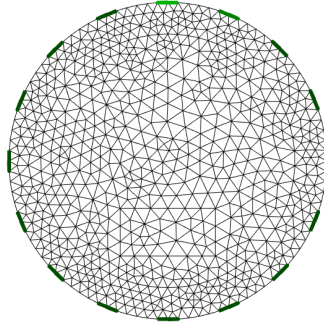


Figure 2.7: **Example 1** Singular values decay.

Example 2

In this example the influence of the number of measurements on the conditioning of matrix $J^T J$ is considered. A stimulation protocol includes the number of electrodes L , the injection pattern, the measurement pattern, and the measurement collection protocol: because of the reciprocity binding the measurements, one might choose to collect only half of them. Different combinations of these features yield different numbers of measurements, hence different numbers of rows for matrix J . For this analysis we consider 6 configurations, given by $L = 8, 16, 32$ and two collection protocols, *half* or *full*, for each of them. *Opposite injection* and *adjacent measurement* protocol are fixed for all the cases and no measurement is performed on the *driving pair*. We work on a mesh with 750 nodes and 1402 triangles, as shown in Figure 2.8, and the Jacobian is computed with respect to a constant conductivity distribution 1 Sm^{-1} .

The results reported in Table 2.2 show that for $L = 8, 16$ choosing half measurements yields better conditioning for the matrix, but this does not hold for the case $L = 32$, so it is only partially correct to state that the more measurements one considers, the worse the conditioning of the matrix becomes.

Figure 2.8: **Example 2**Table 2.2: **Example 2** Condition numbers for matrix $J^T J$ for different numbers of measurements.

L	Coll. protocol	Total meas.	$\text{Cond}(J^T J)$
8	half meas.	16	2.53×10^{20}
	full meas	32	1.89×10^{21}
16	half meas.	96	2.61×10^{20}
	full meas	192	6.26×10^{20}
32	half meas.	448	7.30×10^{21}
	full meas	896	1.53×10^{21}

In general one could infer that $L = 16$ is the least ill conditioned case.

In conclusion, the results on the conditioning of matrix J suggest that one should consider to adopt a regularization technique when tackling the inverse EIT problem in order to obtain reliable solutions.

Chapter 3

Numerical Methods for EIT

3.1 The spatial domain discretization

Let $\Omega \subset \mathbb{R}^d$, $d = 2, 3$ be the region where the conductivity has to be reconstructed. In order to solve the forward and inverse EIT problems one needs to discretize the spatial domain Ω with a suitable geometric structure. A common choice is a $2D/3D$ mesh $\mathcal{M} = (\mathcal{V}, \mathcal{T}, \mathcal{E})$ that can be represented by a graph structure with a set of vertices

$$\mathcal{V} = \{v_1, \dots, v_{n_v}\}, \quad v_i \in \mathbb{R}^2/\mathbb{R}^3,$$

a set of edges

$$\mathcal{E} = \{e_1, \dots, e_{n_e}\}, \quad e_i \in \mathcal{V} \times \mathcal{V},$$

and a set of polygonal or polyhedral elements (*e.g.* triangles in $2D$, tetrahedra in $3D$) connecting them

$$\mathcal{T} = \{T_1, \dots, T_{n_T}\}, \quad T_i \in \mathcal{V} \times \mathcal{V} \times \mathcal{V}(\times \mathcal{V}).$$

Once the surface mesh is defined, it is important to choose a proper data structure to store and handle the geometric model, according to both topological and algorithm requirements. For the purpose of EIT one should consider

that polygonal or polyhedral elements are the most important features to which data are attached, therefore a so called *face-based data structure* is the most common choice. More specifically, We use a *indexed face set* data structure, where vertices coordinates are stored in an array and polygons are stored as sets of indices into this array [11]. The only edges in the $2D$ case, or faces in the $3D$ case, to which data are attached are the ones defining the boundary of the mesh, and for them a specific boundary *indexed face set* structure is defined. The measured voltages V_m are associated to boundary edges e_i . The conductivity σ is described by the piecewise constant elements T_i .

Remark 3.1. The geometric model is represented in EIDORS object `fwd_model` , together with the electrodes model and the stimulation patterns. As reported by Adler and Lionheart in [4], field `nodes` ($n_v \times d$) describes the position of the vertices, field `elems` ($n_v \times (d + 1)$) describes the polygonal elements and field `boundary` ($n_B \times d$) the edges on the boundary (where n_v is the number of vertices, n_T is the number of simplices, n_B the number of simplices with a boundary face and d is the dimension of the model).

3.2 Finite Elements Method (FEM) for forward EIT problem

The usual approach to forward EIT is based on a FEM model to solve (2.1), starting from the weak formulation of (2.1)-(2.14) and applying Green's Identity

$$\int_{\Omega} \sigma \nabla u \cdot \nabla w d\Omega = \int_{\partial\Omega} w \sigma \frac{\partial u}{\partial n} dS \quad (3.1)$$

where w is a test function in a suitable space. As defined in [25], the domain Ω is discretized by a mesh which consists of n_v vertices $x_i \in \Omega$, $i = 1, \dots, n_v$, and n_T triangles T_k , $k = 1, \dots, n_T$, such that

- intersection of two triangles is only allowed to be within faces, i.e. the

convex hull of a set of three vertices the triangles share,

- union $\cup_k T_k$ needs to be a polyhedral approximation of Ω .

Basis functions $\phi_i(x)$ are chosen to be piecewise linear and such that

$$\phi_i(x_j) = \delta_{ij} \text{ for } i, j = 1, \dots, n_v.$$

The piecewise linear approximation of the potential is

$$u(x) \approx u_V(x) = \sum_{i=1}^{n_v} u_i \phi_i(x) \text{ for } u_i \in \mathbb{R},$$

and conductivity is a constant positive definite value σ_i on each triangle.

Within such framework, choosing basis functions ϕ_i for $i = 1, \dots, n_v$ as test functions yields

$$\begin{aligned} \int_{\Omega} \sigma \nabla u \cdot \nabla \phi_i d\Omega &= \int_{\Omega} \sigma \sum_{j=1}^{n_v} u_j \nabla \phi_j \cdot \nabla \phi_i d\Omega = \\ &= \sum_{k=1}^{n_T} \sigma_k \sum_{j=1}^{n_v} u_j \nabla \phi_j \cdot \nabla \phi_i |T_k| = \\ &= \sum_{k:\{x_i, x_j\} \subset T_k} u_j \sigma_k \nabla \phi_j \cdot \nabla \phi_i |T_k| \end{aligned} \quad (\text{NUM})$$

so the FEM matrix, known as *stiffness matrix*, $K \in \mathbb{R}^{n_v \times n_v}$ is defined as

$$K_{ij} = \sum_{k:\{x_i, x_j\} \subset T_k} \nabla \phi_i \cdot \sigma_k \nabla \phi_j |T_k|$$

where $|T_k|$ is the measure of the volume of the considered simplex and $\nabla \phi_i$ is assumed to be constant. Clearly the third identity in (NUM) is given by the fact that basis functions are both nonzero if and only if their nodes belong to the same triangle. This results in matrix K being sparse and having zero

3. Numerical Methods for EIT

elements for each indices pair $\{i, j\}$ defining a couple of vertices that do not belong to the same triangle. A way to build K , as described in [19], is to define a gradient operator $D \in \mathbb{R}^{dn_T \times n_v}$ (where d corresponds to the dimension of the problem) which associates the vector of vertex values of a piecewise linear function ϕ with the vector of its gradient $\nabla\phi$ on each simplex. One then defines the following matrix by means of Kronecker product

$$\Sigma(\sigma) = \text{diag}(\sigma_k |T_k|) \otimes I_d$$

where I_d is the $d \times d$ identity matrix. Thus, the main block of the system matrix is defined as

$$K(\sigma) = D^T \Sigma(\sigma) D. \quad (3.2)$$

Considering the RHS in (3.1), the choice of $\phi_i \quad i = 1, \dots, n_v$ as test functions yields

$$I_i = \int_{\partial\Omega} \sigma \nabla u \cdot n \phi_i dS,$$

so $I \in \mathbb{R}^{n_v}$ is the current vector. The linear system arising from this formulation is then

$$Ku = I. \quad (3.3)$$

In order to obtain a unique solution an additional condition is needed, since one can only determine the voltage up to a constant. The easiest way to do this is to elect a vertex i_g as the *grounded vertex* and force $u_{i_g} = 0$ by removing from the system the corresponding row and column.

System (3.3) implements the *shunt model* and is equivalent to Ohm's and Kirkchoff's law for a resistor network where nodes i and j are connected by a resistor if the corresponding vertices in the mesh structure share a common edge [2].

The implementation of the CEM requires to take the boundary condition into account: (2.14) can be rearranged into

$$\sigma \frac{\partial u}{\partial n} = \frac{1}{z_l} (V_l - u) \quad \text{on } E_l \quad l = 1, \dots, L,$$

thus, if z_l is assumed to be constant on E_l

$$\begin{aligned}
I_i &= \int_{\partial\Omega} \sigma \nabla u \cdot n \phi_i dS = \\
&= \sum_{l=1}^L \int_{E_l} \frac{1}{z_l} (V_l - u) \phi_i dS = \\
&= \sum_{l=1}^L \int_{E_l} \frac{V_l}{z_l} \phi_i dS - \sum_{l=1}^L \int_{E_l} \frac{1}{z_l} \phi_i \left(\sum_{j=1}^{n_v} u_j \phi_j \right) dS = \\
&= \sum_{l=1}^L \frac{V_l}{z_l} \int_{E_l} \phi_i dS - \sum_{l=1}^L \sum_{j=1}^{n_v} u_j \frac{1}{z_l} \int_{E_l} \phi_i \phi_j dS = \\
&= A_i^W V - A_i^Z \underline{u}
\end{aligned}$$

where A_i^W and A_i^Z are the i th rows of matrices $A^W \in \mathbb{R}^{n_v \times L}$ and $A^Z \in \mathbb{R}^{n_v \times n_v}$ such that

$$\begin{aligned}
A_{i,l}^W &= \frac{1}{z_l} \int_{E_l} \phi_i \phi_j dS \\
A_{i,j}^Z &= \sum_{l=1}^L \frac{1}{z_l} \int_{E_l} \phi_i \phi_j dS
\end{aligned}$$

then

$$\begin{bmatrix} K + A^Z & -A^W \end{bmatrix} \cdot \begin{bmatrix} \underline{u} \\ V \end{bmatrix} = 0$$

The known total current is

$$\begin{aligned}
I_l &= \int_{E_l} \frac{1}{z_l} (V_l - u) dS = \\
&= \int_{E_l} \frac{1}{z_l} V_l dS - \sum_{i=1}^V u_i \int_{E_l} \frac{1}{z_l} \phi_i dS = \\
&= \frac{1}{z_l} |E_l| V_l - \frac{1}{z_l} \sum_{i=1}^V u_i \int_{E_l} \phi_i dS = \\
&= [A^D V]_l - [(A^W)^T \underline{u}]_l
\end{aligned}$$

where A^D is the diagonal matrix $A^D = \text{diag}(\frac{|E_i|}{z_i})$. Then

$$\begin{bmatrix} -(A^W)^T & A^D \end{bmatrix} \cdot \begin{bmatrix} u \\ V \end{bmatrix} = I$$

The FEM system for the Complete Electrode Model is then

$$\begin{bmatrix} K + A^Z & -A^W \\ -(A^W)^T & A^D \end{bmatrix} \cdot \begin{bmatrix} u \\ V \end{bmatrix} = \begin{bmatrix} 0 \\ I \end{bmatrix}.$$

3.3 Compute of the Jacobian Matrix in EIDORS

The calculation of the Jacobian Matrix in EIDORS, as described in [18], is based on the idea of using the system matrix K in (3.3) arising from the FEM for the forward problem as the matrix $Y(\sigma) \in \mathbb{R}^{n_v \times n_v}$ which associates each FEM element $k = 1, \dots, n_T$ to its conductivity σ_k and its nodes and is known as *admittance matrix*. The Neumann Boundary conditions can be stored into a matrix $Q \in \mathbb{R}^{n_v \times L}$ such that each column defines which electrodes inject current into the medium and the matrix product

$$V = Y^{-1}(\sigma)Q \tag{3.4}$$

generates matrix $V \in \mathbb{R}^{n_v \times L}$ known as *nodal potential difference matrix* from which voltage measurements in V_m can be defined by means of elementwise subtractions. Equation (3.4) can be considered as a discrete version of the Neumann to Dirichlet map (2.8).

A variation in the voltages due to a change in the conductivity yields the computation of

$$\frac{\partial V}{\partial \sigma_k} = \frac{\partial}{\partial \sigma_k} (Y^{-1}Q) = \frac{\partial}{\partial \sigma_k} (Y^{-1}) Q. \tag{3.5}$$

The derivative of the inverse matrix can be computed as follows:

$$\begin{aligned}
\frac{\partial}{\partial \sigma_k} (Y^{-1}) &= -Y^{-1} \frac{\partial Y}{\partial \sigma_k} Y^{-T} = \\
&= -Y^{-1} \frac{\partial}{\partial \sigma_k} (D^T \Sigma(\sigma) D) Y^{-T} = \\
&= -Y^{-1} D^T \frac{\partial \Sigma(\sigma)}{\partial \sigma_k} D Y^{-T} = \\
&= -Y^{-1} D^T \frac{\partial \Sigma(\sigma)}{\partial \sigma_k} D Y^{-T} = \\
&= -Y^{-1} D^T \frac{\partial}{\partial \sigma_k} (\text{diag}(\sigma) \otimes I_{(d)}) D Y^{-T} = \\
&= -Y^{-1} D^T \frac{\partial}{\partial \sigma_k} (\text{diag}(\sigma)) \otimes I_{(d)} D Y^{-T},
\end{aligned}$$

where a decomposition similar to (3.2), $Y(\sigma) = D^T \Sigma(\sigma) D$ with $\Sigma(\sigma) = \text{diag}(\sigma) \otimes I_d$ is considered. By defining $\Xi_k = \frac{\partial}{\partial \sigma_k} (\text{diag}(\sigma)) \in \mathbb{R}^{n_v \times n_v}$, i.e. the matrix with only one nonzero element s.t. $(\Xi_k)_{k,k} = 1$, Equation (3.5) can be rewritten as

$$\frac{\partial V}{\partial \sigma_k} = -Y^{-1} D^T \Xi_k \otimes I_d D Y^{-T} Q = -Y^{-1} D^T \Xi_k \otimes I_d D V. \quad (3.6)$$

Given matrix in (3.6), the Jacobian matrix is assembled defining a subcomponent $J_j \in \mathbb{R}^{M \times n_T}$ $1 \leq j \leq L$ for each stimulation pattern (M corresponds to the stated number of measurement per injection pattern as specified in the measurement protocol):

$$J = \begin{bmatrix} J_1 \\ \vdots \\ J_L \end{bmatrix} \quad (3.7)$$

where the sensitivity matrix for each stimulation j is defined using column j of (3.6) for all elements $k = 1, \dots, n_T$, and the j th subcomponent of the Jacobian is obtained by means of an operator \mathbb{M} which selects the jacobian rows corresponding to an available pair of electrodes during the j th stimulation,

as stated in the measurement protocol:

$$J_j = \mathbb{M} \left[\frac{\partial V_j}{\partial \sigma_1}, \dots, \frac{\partial V_j}{\partial \sigma_T} \right]. \quad (3.8)$$

3.4 Numerical Methods for inverse EIT problem

3.4.1 Truncated Singular Value Decomposition (TSVD)

A commonly used numerical method in linear inverse problems resolution is the Truncated Singular Value Decomposition. It is designed to solve a linear least squares problem and allows to define a regularized solution when the coefficient involved matrix is ill-conditioned and rank deficient. In EIT it can be used to solve the linearized problem (EIT-L) model. The method is based on the fact that matrix $J \in \mathbb{R}^{M \times n_T}$ allows a Singular Value Decomposition

$$J = U \Sigma V^T = \sum_{i=1}^r s_i u_i v_i^T,$$

where $r = \min(M, N)$, from which the minimum norm solution of the least squares problem (EIT-L) can be defined as

$$\sigma = \sum_{i=1}^r \frac{\langle u_i, V_m \rangle}{s_i} v_i. \quad (\text{SVD})$$

As Holder describes in [19], singular vectors v_i can be interpreted as stating the components $\langle v_i, \sigma \rangle$ of a conductivity change become more and more hard to determine as i increases, because they produce voltage changes $s_i \langle u_i, \sigma \rangle$. A relative error ϵ in the measured voltages allows to reliably recover the components $\langle v_i, \sigma \rangle$ of the image only when $s_i/s_1 > \epsilon$. The procedure of TSVD requires to stop the assembling of the solution in (SVD) to an index $k \leq r$ up to which the components can be reliably recovered and s_i 's are not

small enough to generate high oscillations:

$$\sigma_k = \sum_{i=1}^k \frac{\langle u_i, V_m \rangle}{s_i} v_i. \quad (\text{TSVD})$$

The number k of admitted singular values s_i represents in TSVD the regularization parameter.

3.4.2 The Gauss-Newton method for NLLS

By means of the Gauss-Newton method for nonlinear least squares (NLLS) one seeks to minimize a nonlinear objective function [27]

$$f(x) = \frac{1}{2} \sum_{k=1}^m r_k^2(x) = \|r(x)\|_2^2$$

where $x \in \mathbb{R}^n$, n is the number of variables and $r(x)$ is a vector of *residuals* $r : \mathbb{R}^n \rightarrow \mathbb{R}^m$, where $m \geq n$. For $r(x) = Ax - b$ this reduces to *linear least squares*. For a nonlinear $r(x)$, by defining the Jacobian matrix of $r(x)$

$$[J(x)]_{i,j} = \frac{\partial r_i(x)}{\partial x_j}$$

one has gradient and Hessian respectively

$$\nabla f(x) = \sum_k r_k(x) \nabla r_k = J(x)^T r(x)$$

$$\begin{aligned} \nabla^2 f(x) &= \sum_n \nabla r_k(x) \nabla r_k(x)^T + \sum_k r_k(x) \nabla^2 r_k(x) = \\ &= J(x)^T J(x) + \sum_k r_k(x) \nabla^2 r_k(x) \approx \\ &\approx J(x)^T J(x). \end{aligned}$$

From considering the second-order Taylor approximation of function $f(x)$:

$$f(x + p) = f(x) + \nabla f(x)^T p + \frac{1}{2} p^T \nabla^2 f(x) p, \quad (3.9)$$

and imposing optimality condition

$$\frac{\partial f(x + p)}{\partial p} = \nabla f(x)^T + \nabla^2 f(x) p = 0, \quad (3.10)$$

follows

$$p = -(\nabla^2 f(x))^{-1} \nabla f(x). \quad (3.11)$$

The search direction p^{NR} is given by

$$\nabla^2 f(x) p^{NR} = -\nabla f(x). \quad (\text{Newton-Raphson})$$

When the search direction p is obtained by dropping the second order term $\sum_k r_k(x) \nabla^2 r_k(x)$ from $\nabla^2 f(x)$ we get

$$J^T J p^{GN} = -J^T r(x). \quad (\text{Gauss-Newton})$$

GN method is an iterative method which, starting from an initial guess x_0 , computes x_{k+1} at the iteration $k + 1$ as

$$x_{k+1} = x_k + p_k^{GN} = x_k - (J_k^T J_k)^{-1} J_k^T r(x_k) \quad (3.12)$$

Matrix $J_k^T J_k$ is invertible only for $m \geq n$. The reason behind dropping $\sum_k r_k(x) \nabla^2 r_k(x)$ is that as a minimum is approached the second derivative becomes negligible.

3.4.3 Discretization of the Total Variation penalty term

The use of total variation as a regularization term involves the minimization of TV functional, which means that optimality condition (vanishing

of the partial derivatives) needs to be met [8]. It is possible to show that gradient of TV functional is

$$\nabla TV(\sigma) = -\nabla \cdot \frac{\nabla \sigma}{|\nabla \sigma|} \quad (3.13)$$

which is clearly nonlinear and nondifferentiable. As described in detail by Borsic in [8], many modification to the choice of the absolute value have been suggested to overcome the nondifferentiability of TV , and the most recurring one (which is also going to be used in this dissertation) is

$$TV_\beta(\sigma) = \int_{\Omega} \sqrt{|\nabla \sigma|^2 + \beta} dx \quad (3.14)$$

for a small β parameter.

For what concerns the discretization of the TV term

$$TV(\sigma) = \int_{\Omega} |\nabla \sigma| d\Omega,$$

since conductivity is defined as piecewise constant elements, the TV operator of a 2D function can be discretized on a mesh \mathcal{M} where $\mathcal{M} = (\mathcal{V}, \mathcal{T})$ (\mathcal{T} is the set of elements and \mathcal{V} the set of vertices) via a weighted summation of the total variation of each edge k in the mesh, where each weight is defined as the length l_k of the corresponding edge:

$$TV(\sigma) = \sum_k l_k |\sigma_{m(k)} - \sigma_{n(k)}|$$

where index k ranges over all the edges, while $m(k)$ and $n(k)$ represent the indices of the mesh elements on the opposite sides of the considered edge. In order to gain a more compact definition, it is possible to build a sparse matrix D such that each row D_k has two nonzero elements, l_k and $-l_k$, whose

column indices are $m(k)$ and $n(k)$:

$$TV(\sigma) = \sum_k |D_k \sigma| = \|D\sigma\|_1 \quad (3.15)$$

The generalization to the 3D case is straightforward, one only needs to consider that the weights correspond to the areas of the faces connecting two adjacent tetrahedra instead of the lengths of the edges, index k is applied to faces and $m(k)$ and $n(k)$ represent the indices of the mesh elements on the opposite sides of the considered face.

The use of absolute value guarantees convexity (positivity) but makes the penalty function non-differentiable whenever $\sigma_{m(k)} - \sigma_{n(k)} = 0$. The correction, similarly to (3.14), in this case is

$$TV_\beta(\sigma) = \sum_k \sqrt{|D_k \sigma|^2 + \beta}$$

Remark 3.2. Matrix D which discretizes the regularized operator defined in (3.14) can be defined in EIDORS by setting *TV priors*: it is indeed a model-regularization matrix.

3.4.4 Solving Model EIT-L (RL)

The least squares method applied to problem (EIT-L (RL)) where the fidelity term is linearized and optimization is run on the conductivity change, can easily be defined as follows:

$$\begin{aligned} \mathcal{J}_L(\sigma) &:= \|J\sigma - V_m\|_2^2 + \alpha \|L\sigma - L\sigma_{ref}\|_2^2 = \\ &= \left\| \begin{bmatrix} J \\ \alpha L \end{bmatrix} \sigma - \begin{bmatrix} V_m \\ \alpha L\sigma_{ref} \end{bmatrix} \right\|_2^2 = \\ &= \|\tilde{J}\sigma - \tilde{V}_m\|_2^2. \end{aligned}$$

Assuming \tilde{J} is full rank, the solution is

$$\sigma = (\tilde{J}^T \tilde{J})^{-1} \tilde{J}^T \tilde{V}_m$$

that is the regularized least squares solution

$$(J^T J + \alpha^2 L^T L) \sigma = (J^T V + \alpha^2 L^T L \sigma_{ref}). \quad (3.16)$$

This kind of approach actually leads to a One-Step Gauss-Newton method and the optimal conductivity change is directly determined as the solution of the linear system (3.16).

3.4.5 Solving Model EIT-NL-R

As already mentioned, applying the Gauss-Newton method to problem (EIT-NL) yields bad solutions due to ill-conditioning of matrix $J^T J$: as a matter of fact the solution lies in a long narrow valley of the objective function, one could instead apply the same method to (EIT-NL-R) where G as in (RL) is chosen to be a linear operator, since it is possible to assume that for a well chosen G the residual function

$$\mathcal{J}_{NL}(\sigma) = \|F(\sigma) - V_m\|_2^2 + \alpha \|L(\sigma - \sigma_{ref})\|_2^2$$

will have a critical point corresponding to the minimum, for which $\nabla \mathcal{J}_{NL}(\sigma) = 0$ [19]. Gradient and Jacobian matrix of the objective function \mathcal{J}_{NL} are respectively:

$$\nabla \mathcal{J}_{NL}(\sigma) = J(\sigma)^T (F(\sigma) - V_m) + \alpha L^T L (\sigma - \sigma_{ref})$$

$$\nabla^2 \mathcal{J}_{NL}(\sigma) = \nabla^2 F(\sigma) (F(\sigma) - V_m) + J(\sigma)^T J(\sigma) + \alpha L^T L$$

In order to implement Gauss Newton methods the second order term in the Hessian of the objective function needs to be neglected and search

3. Numerical Methods for EIT

direction p^{GN} is to be defined at the n th iteration as the solution of:

$$\begin{aligned} (J_k^T J_k + \alpha L^T L) p_k^{GN} &= -J(\sigma_k)^T (F(\sigma_k) - V_m) - \alpha L^T L(\sigma_k - \sigma_{ref}) \\ &= J(\sigma_k)^T (V_m - F(\sigma_k)) + \alpha L^T L(\sigma_{ref} - \sigma_k) \end{aligned} \quad (3.17)$$

so that

$$\sigma_{k+1} = \sigma_k + p_k^{GN} \quad (3.18)$$

In order to solve the nonlinear problem EIT-NL-R with nonlinear regularization term (RNL)

$$\mathcal{J}_{NL}(\sigma) := \|F(\sigma) - V_m\|_2^2 + \alpha TV(\sigma)$$

the idea is to set the gradient of the objective function \mathcal{J}_{NL} to zero:

$$\begin{aligned} \nabla \mathcal{J}_{NL}(\sigma) &= J^T (F(\sigma) - V_m) - \alpha \nabla \cdot \frac{\nabla \sigma}{\sqrt{|\nabla \sigma|^2 + \beta}} = \\ &= J^T (F(\sigma) - V_m) + \alpha \mathcal{L}_\beta(\sigma) \sigma = \\ &= 0 \end{aligned}$$

where $\mathcal{L}_\beta(\sigma)$ is the *Diffusion operator* regularized by a small parameter $\beta > 0$ that is defined as

$$\mathcal{L}_\beta(\sigma)v = \nabla \cdot \frac{\nabla v}{\sqrt{|\nabla \sigma|^2 + \beta}}.$$

Since $F(\sigma) \approx J\sigma$ is linearized, the equation can then be rearranged into the form

$$(J^T J + \alpha \mathcal{L}_\beta(\sigma))\sigma = J^T V_m$$

from which the fixed point iteration at the iterative step k follows

$$\sigma_{k+1} = [J^T J + \alpha \mathcal{L}_\beta(\sigma_k)]^{-1} J^T V_m.$$

Under specific conditions on J , such as linearity, bounded condition number, injectivity [8], this iteration converges to the minimum. The name Lagged

Diffusivity comes from the fact that each iteration involves the evaluation of the *diffusion operator* at the preceding step.

In [8] Borsic describes an equivalent numerical method that results in a IRLS (Iterative reweighted least squares) method which can be derived from the Newton's Method by dropping the negative semidefinite matrix $\mathcal{L}'_{\beta}(\sigma)$ from the Hessian matrix of the objective function:

$$\nabla^2 \mathcal{J}_{NL}(\sigma) = J^T J + \alpha \mathcal{L}_{\beta}(\sigma) + \alpha \mathcal{L}'_{\beta}(\sigma) \sigma$$

where

$$\mathcal{L}'_{\beta}(\sigma)v = \nabla \cdot \frac{\nabla \sigma \cdot \nabla v}{\sqrt{(|\nabla \sigma|^2 + \beta)^3}} \nabla \sigma.$$

The Gauss-Newton iteration is then

$$\sigma_{k+1} = \sigma_k + p_k^{GN}$$

where p_k^{GN} is obtained by solving the linear system

$$(J^T J + \alpha \mathcal{L}_{\beta}(\sigma_k)) p_k^{GN} = \nabla \mathcal{J}_{NL}(\sigma_k). \quad (3.19)$$

3.4.6 Newton One-Step Error Reconstruction (NOSER)

One of the earliest methods specifically designed to address the nonlinear inverse conductivity problem as formulated in (EIT-NL) is NOSER (Newton One-step Error Reconstructor) [15]. It was designed for two dimensional problems where the body $\Omega \subset \mathbb{R}^2$ is a disk of radius r_0 and an even number L of electrode is used.

The idea behind the method is similar to the one that leads to the Gauss-Newton's method for NLLS, because the nonlinear system of N equations in N variables is solved by means of one step of a modified version of Newton-Raphson's Method, starting from an assumption of constant conductivity

σ_0 :

$$\sigma = \sigma_0 - [\nabla^2 f(\sigma_0)]^{-1} \nabla f(\sigma_0)$$

The difference with Gauss-Newton's method is that the second order term arising in $\nabla^2 f(\sigma)$ is not simply dropped but substituted in order to gain positive definiteness for the matrix. To such end the authors in [15] considered the fact that the elements on the diagonal of matrix $J^T J$ are all positive and thus generate a well conditioned diagonal matrix. In conclusion the regularization matrix of NOSER method is

$$L = \text{diag}(\text{diag}(J^T J)) \tag{3.20}$$

and the Gauss-Newton method (3.12) is regularized as follows

$$\sigma = \sigma_0 - (J^T J + \alpha L)^{-1} J^T (F(\sigma) - V_m)$$

where α is the regularization term and is supposed to be chosen as small as possible, but at the same time large enough to make the modified matrix not only diagonally dominant but also positive definite, which results in improved conditioning.

Remark 3.3. EIDORS does not distinguish between model-regularization matrices, i.e. the ones that are defined within the construction of a regularized model, as in (EIT-L (RL)), and method-regularization matrices, i.e. the ones that arise in the construction of the numerical method, as in NOSER: this is why they are all generally defined as *priors*.

NOSER *prior*, which corresponds to the diagonal matrix in (3.20), can then also be used as a regularization term for a *One-step Gauss-Newton* (OGN) solver such as `@inv_solve_diff_GN_one_step`, which is though used when the linearized problem is concerned.

The proper way to implement the algorithm for the nonlinear problem

is to manually define the reconstruction matrix and generate a solution by means of a matrix-vector multiplication:

$$RM = (J^T J + \alpha L)^{-1} J^T$$

$$\sigma - \sigma_0 = RM(F(\sigma) - V_m)$$

with L defined in (3.20). This latter multiplication can be carried out by means of function `@solve_use_matrix`.

3.4.7 A Primal Method with TV: Lagged Diffusivity

The discretized form of the *Diffusion operator* is defined as follows:

$$\mathcal{L}_\beta(\sigma) = D^T E^{-1} D$$

where D is defined as in 3.15 and $E = \text{diag}(\eta_i)$, $\eta_i = \sqrt{|D_i \sigma|^2 + \beta}$. Then the discrete Quasi-Newton iteration is

$$\sigma_{k+1} = \sigma_k - p_k$$

where p_k is obtained by solving the linear system

$$[J^T J + \alpha D^T E^{-1} D] p_k = [J^T (F(\sigma) - V_m) + \alpha D^T E^{-1} D \sigma_k].$$

Remark 3.4. This reminds of the normal equations of problem (EIT-L (RL)), with the fundamental difference that E depends on σ , which makes the equation nonlinear.

It is though possible to think this Newton's iteration as an IRLS method applied to the penalty term *TV* [8]. IRLS is an iterative method that allows to solve l_p -norm problems such as

$$\min_x \frac{1}{p} \|Ax - y\|_p^p$$

by considering the following set of nonlinear normal equations

$$A^T W A x = A^T W y$$

where weighting matrix W depends on x and is updated at each iteration.

3.4.8 A Primal-Dual method with TV: PD-IPM

The Primal Dual Interior Point Method was designed to address problems that can be modelled as a Minimization of a Sum of Norms (MSN) [9] [26]. It is based on the idea of considering two equivalent formulations for the problem, a *primal problem* (P), which is a minimization problem with specific primal variables and primal feasible region, and a *dual problem*, which is a maximization problem with specific dual variables and dual feasible region. The difference between primal and dual objective function is called *primal-dual gap*, it involves both primal and dual variables, it is always nonnegative and vanishes only for optimal points for both the primal and dual problem, in case a specific condition, called *complementary condition* is satisfied. Primal feasibility condition, dual feasibility condition and the complementary condition define the set of equation that need to be solved in order to solve the problem.

For the inverse problem with linearized Forward perator and discretized TV operator

$$TV(x) = \sum_k |D_k x| = \|Dx\|_1, \quad (3.21)$$

the primal problem is

$$\min_x \frac{1}{2} \|Ax - b\| + \alpha \|Dx\|_1 \quad (P)$$

and the dual can be derived from (P) by considering $\|Dx\|_1 := \max_{y: \|y\| \leq 1} y^T Dx$

$$\max_{y: \|y\| \leq 1} \min_x \frac{1}{2} \|Ax - b\| + \alpha y^T Dx. \quad (D1)$$

The optimal point for the minimization problem in (D1) is given by the first order condition $A^T(Ax - b) + \alpha D^T y = 0$, so (D1) can be written deleting the minimization part and imposing a new constraint on x and y

$$\max_{\substack{y: \|y\| \leq 1 \\ A^T(Ax-b) + \alpha D^T y = 0}} \frac{1}{2} \|Ax - b\| + \alpha y^T Dx. \quad (\text{D2})$$

The *primal-dual gap* for (P) and (D2) is then $\|Dx\| - y^T Dx$, which vanishes when $Dx = 0$ or when $y = \frac{Dx}{\|Dx\|}$; this second case leads to the *complementary condition*

$$Dx - \|Dx\|y = 0$$

which is not differentiable for $Dx = 0$ so $\|Dx\|$ is generally replaced by $(\|Dx\|^2 + \beta)^{\frac{1}{2}}$. By defining $E = \text{diag}(\sqrt{|D_i s|^2 + \beta})$, the set of equation of the PDIPM is then

$$\|y\| \leq 1 \quad (\text{C1})$$

$$A^T(Ax - b) + \alpha D^T y = 0 \quad (\text{C2})$$

$$Dx - Ey = 0 \quad (\text{C3})$$

As declared in [19] and [9], this method was implemented for inverse problems with linear Forward Operators, but with small modification it was possible to apply it to the EIT inverse problem (EIT-NL-R) with $G(\sigma) = TV(\sigma)$. To this end, the *primal* and *dual EIT problems* are formulated as

$$\min_{\sigma} \frac{1}{2} \|F(\sigma) - V_m\| + \alpha \|D\sigma\|_1 \quad (\text{EIT P})$$

$$\max_{\substack{y: \|y\| \leq 1 \\ J^T(F(\sigma) - V_m) + \alpha D^T y = 0}} \frac{1}{2} \|F(\sigma) - V_m\| + \alpha y^T D\sigma. \quad (\text{EIT D})$$

The system of nonlinear equations is

$$\|y\| \leq 1 \quad (\text{EIT C1})$$

3. Numerical Methods for EIT

$$J^T(F(\sigma) - V_m) + \alpha D^T y = 0 \quad (\text{EIT C2})$$

$$D\sigma - Ey = 0, \quad (\text{EIT C3})$$

and it can be solved by means of Newton's Method, for which partial differential of (EIT C2) and (EIT C3) are needed:

$$\frac{\partial}{\partial \sigma}(J^T(F(\sigma) - V_m) + \alpha D^T y) = J^T J$$

$$\frac{\partial}{\partial \sigma}(D\sigma - Ey) = D - E^{-1} D \text{diag}(y_i D_i \sigma)$$

$$\frac{\partial}{\partial y}(J^T(F(\sigma) - V_m) + \alpha D^T y) = \alpha D^T$$

$$\frac{\partial}{\partial y}(D\sigma - Ey) = -E.$$

In order to update σ and y the following system is to be considered:

$$\begin{bmatrix} J^T J & \alpha D^T \\ HD & -E \end{bmatrix} \begin{bmatrix} \sigma \\ \delta y \end{bmatrix} = \begin{bmatrix} J^T(F(\sigma) - V_m) + \alpha D^T y \\ D\sigma - Ey \end{bmatrix}$$

where $H = I - \frac{\text{diag}(y_i D_i \sigma)}{E_{i,i}}$

Remark 3.5. The original PDIPM requires the update of the Jacobian matrix at every iteration, but the authors in [9] suggest not to follow this procedure because it only increases the computational time without yielding any better result.

Remark 3.6. The PDIPM scheme is general and allows to use the method even for 3D EIT problems.

3.5 Numerical Methods in EIDORS

EIDORS offers a variety of functions that implement the previously described numerical methods. They are constantly reviewed and updated and an online documentation can be consulted. For the purposes of this work

functions in Table 3.1 have been used.

Table 3.1: Numerical Methods in Eidders

Model	Reg	Method	Function
EIT-NL	none	NOSER	@solve_use_matrix
EIT-NL-R	LR	IGN	@inv_solve_gn
	NLR	IRLS	@inv_solve_TV_irls
		PD-IPM	@inv_solve_abs_pdipm
EIT-L	none	TSVD	@inv_solve_TSVD
EIT-L-R	LR	OGN	@inv_solve_diff_GN_one_step
	NLR	PD-IPM	@inv_solve_diff_pdipm @inv_solve_TV_PDIPM

Chapter 4

Numerical Tests

4.1 The 2D setup

The case tests consisted of a circular tank of radius $r_0 = 1$ with 1 ring of 16 electrodes; the chosen current pattern was *opposite injection* and *adjacent measurement* with no measurements performed on current carrying electrodes, which results in 12 measuring pairs for each driving pair and yields 192 total measurements. Drive current level in Ampere was set to 0.1. The conductivity of the background liquid was set to 1 Sm^{-1} . This first setting was named *Empty Measurement Chamber* and was used as a baseline for time difference reconstruction. Different kinds of inclusions inside the scaffold were then considered in order to test the different performances of the methods: piecewise constant, smooth and piecewise smooth.

E-test A scaffold of radius $r_1 = 0.8$ and conductivity $\sigma = 1.1 \text{ Sm}^{-1}$ was positioned in the middle of the measurement chamber and this represented the first executive model, called *Empty Scaffold*, on which time difference reconstruction was performed with respect to the *Empty Measurement Chamber* model.

PC-test The *Piecewise Constant* (PC) phantom consists of

- a small circular shape of conductivity $\sigma = 1.05 \text{ Sm}^{-1}$ (0.05 Sm^{-1})

below scaffold level) with centre at $(0.4, 0.2)$, radius $r_2 = 0.03$;

- a large squared shape of conductivity $\sigma = 1.15 \text{ Sm}^{-1}$ (0.05 Sm^{-1} above scaffold level) with edge length $l = 0.4$ and corners in $(0, 0.2)$, $(-0.4, -0.2)$, $(-0.4, -0.6)$, $(0, -0.6)$.

SM-test The *Smooth* (SM) phantom included 2 circular shapes of radius $r_3 = 0.03$ generated by means of a Gaussian density function with standard deviation $s = 0.19$

- one with centre in $(0.4, 0.2)$ and smoothly decreasing conductivity (w.r.t scaffold level) to $\sigma = 1.05 \text{ Sm}^{-1}$;
- one with centre in $(-0.4, -0.2)$ and smoothly increasing conductivity (w.r.t scaffold level) to $\sigma = 1.15 \text{ Sm}^{-1}$.

PS-test The *Piecewise Smooth* (PS) phantom consists of a circular shape with radius $r_3 = 0.65$ and centre corresponding to the centre of the scaffold. The conductivity distribution was generated by considering a Gaussian distribution with centre at $(0, 0)$ (which was scaled so that the central conductivity peak reached value $\sigma = 1.150 \text{ Sm}^{-1}$) and then adding 0.02 Sm^{-1} to all the values within a central squared region with edge length 0.6 .

PCSM-test The *Piecewise Constant & Smooth* (PCSM) phantom consists of:

- a circular shape of smoothly decreasing (w.r.t the scaffold level) conductivity down to value $\sigma = 1.075 \text{ Sm}^{-1}$, with centre in $(0, 0.25)$, radius $r_2 = 0.4$, generated by a Gaussian distribution with standard deviation $s = 0.4$;
- a rectangular shape of constant conductivity $\sigma = 1.15 \text{ Sm}^{-1}$ with corners in $(-0.3, -0.6)$, $(-0.3, -0.3)$, $(0.3, -0.6)$, $(0.3, -0.3)$.

The configurations are shown in Table 4.1, both as EIDORS images (first column) and bivariate functions (where z -axis represents the conductivity

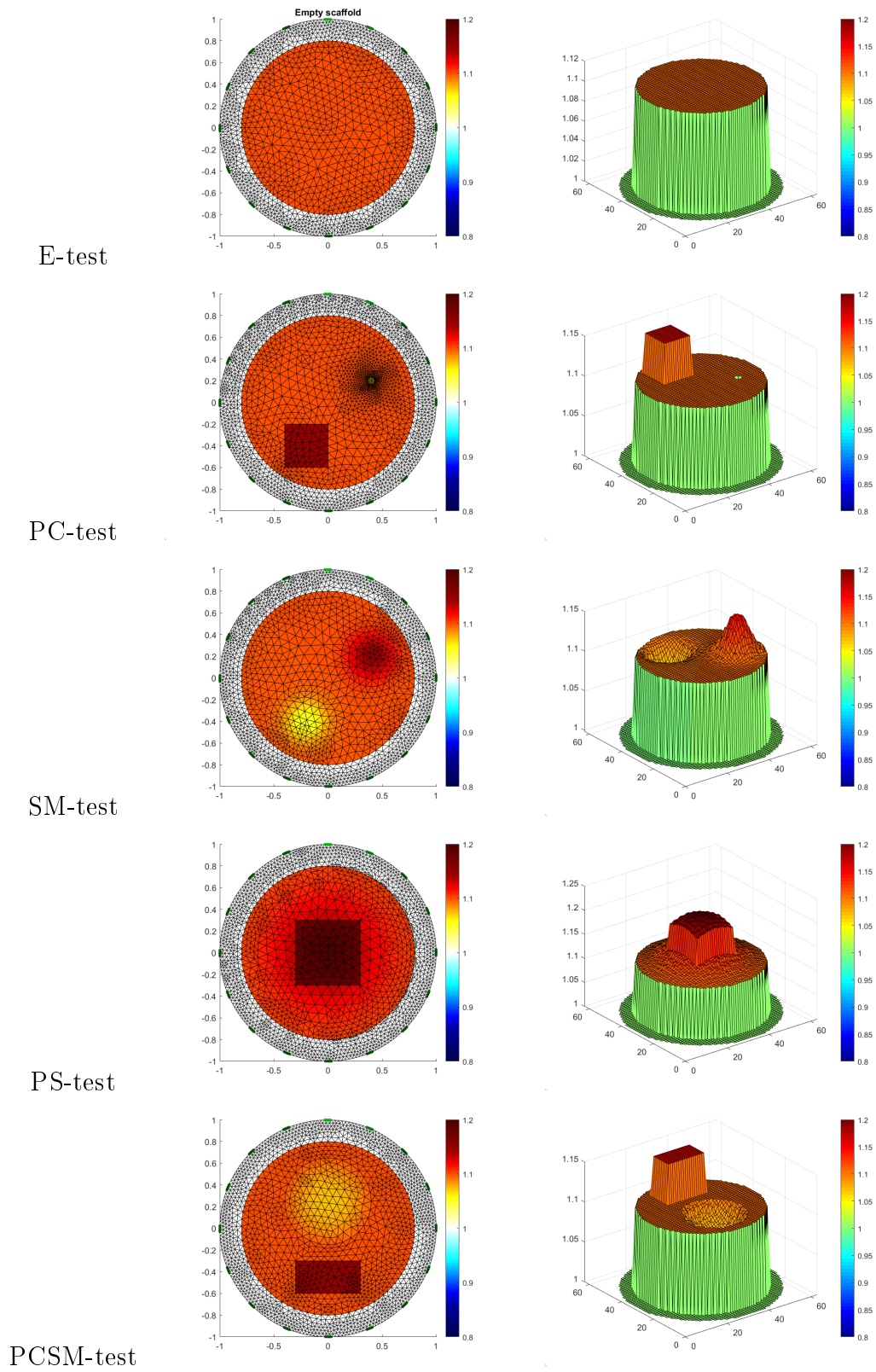


Table 4.1

value), to better visualize the difference between the piecewise constant inclusions and the smooth ones. The different meshes were generated by means of MATLAB pdetoolbox which allowed to design the *ad hoc* geometries. This was purposely arranged in order to provide the methods with the prior information they needed to exactly reconstruct the different features of the inclusions, as a way to test their performance. For each phantom, two meshes were generated: a *coarse* mesh, which was used for the resolution of the inverse problem, and a *fine* mesh, which was used as a framework for a Forward Operator in order to calculate the electric potentials and simulate the data for the inverse calculation. The *fine* mesh was generated by applying MATLAB function `refinemesh` to the *coarse* mesh with refinement method `regular` which divides each triangle into four triangles of the same shape.

4.2 Error Metric

In order to assess the performance of the different algorithms and the goodness of the results, a notion of relative error with respect to a ground truth conductivity distribution needed to be defined. Ground Truth (GT) for the *Empty Scaffold* phantom is the difference between the conductivity distribution of the phantom itself and the conductivity distribution of the *Empty Measurement Chamber* phantom, while for the remaining tests GT is given by the difference between the conductivity distribution of the phantoms and the conductivity distribution of the *Empty Scaffold* phantom. Two metrics have been defined to compute the relative error, that are going to be addressed to as *Slice metric* and *Coarse-to-fine metric*.

- *Slice Metric* is based on EIDORS function `calc_slices` which defines the slices of an EIDORS image structure by means of a rendering algorithm which turns it into a 64×64 matrix of doubles. By doing so it is possible to compare the results of the reconstruction algorithms and

the corresponding GT even if they are defined on two different meshes. Relative error is then defined as the ratio among the Frobenius norm of the mismatch slice-matrix and the Frobenius norm of the GT. If GT_{slice} is the slice of the ground truth and I_{slice} is the slice of the reconstructed conductivity, then relative error ϵ_{slice} is:

$$\epsilon_{slice} = \frac{\|GT_{slice} - I_{slice}\|_F^2}{\|GT_{slice}\|_F^2}.$$

- *Coarse-to-fine metric* uses the coarse-to-fine linear transformation that allows to map a coarse finite elements mesh onto a finer one. Matrix CF of the transformation is computed by EIDORS function `@mk_coarse_fine_mapping` so that $CF_{i,j}$ is the fraction of element i of the finer mesh which is contained in element j of the coarser mesh. This is used to map from data on the reconstruction mesh to the finer mesh as

$$\sigma_{fine} = CF\sigma^*.$$

Relative error is then defined as the ratio among the norm 2 of the mismatch-between-elements-data vector and the norm 2 of the Ground Truth elements data vector. If σ_{GT} is the elements data vector of the Ground Truth on the finer mesh and σ^* is the reconstructed image elements data vector on the coarse mesh, the relative error ϵ_{c2f} is:

$$\epsilon_{c2f} = \frac{\|\sigma_{GT} - CF\sigma^*\|_2^2}{\|\sigma_{GT}\|_2^2}.$$

A third metric which only involved the available data in a realistic simulation could be considered. At this aim, EIDORS function `@calc_solution_error` was considered, as it calculates the residual error for a solution σ^* . If V_s are the simulated voltage measurements based on the calculated solution and V_m are the given voltage measurements, the *relative solution error* ϵ_{sol} is defined

as:

$$\epsilon_{sol} = \frac{\|V_m - V_s\|_2^2}{\|V_m\|_2^2}.$$

4.3 Experimental results

The set of tests was conducted with no additional noise on measured voltages. The considered methods are:

OGNT One-step Gauss-Newton with Tikhonov priors, which belongs to class EIT-L-LR; (see (3.16) where $L = I_n$ with I_n identity matrix);

IGNL Iterative Gauss-Newton with Laplace priors, which belongs to class EIT-NL-LR (see (3.17)-(3.18) with $L = \text{Laplace operator}$);

NOSER Newton One-Step Error Reconstruction which belongs to class EIT-NL;

PDIPM Primal-Dual Interior Point Method which is an iterative method belonging to class EIT-L-NLR;

IRLS Iterative Reweighted Least Squares, which belongs to class EIT-NL-NLR (see (3.19) with TV regularizer).

The regularization parameters for each method and each test were manually chosen among integer powers of 10 as the ones that generated the average best solution according to the considered norms.

The stopping criterion for the three iterative methods is based on the relative change of the linearized objective function $\mathcal{J}(\sigma)$ between two iterations. All methods were assigned tolerance 10^{-16} and the maximum number of iterations was set to 20 for PDIPM, 10 (default) for IGNL and 1000 for IRLS. PDIPM always converged right before the 20th iteration, while IGNL always converged before the 5th iteration. The EIDORS built-in function for IRLS does not provide any information about the iterations.

The Empty Scaffold phantom

All models managed to reconstruct the circular shape of the scaffold, but PD-IPM was the only one to reproduce the step change in conductivity, while all the others performed a quite smooth reconstruction. As far as conductivity magnitude is concerned, all algorithms performed well with no significant loss, but if the precise value is to be considered, all tended to define a solution that oscillates around the ground truth, as shown in Figure 4.1. This resulted in an annulus of values higher than 0.1 and a central concavity of values smaller than 0.1. PD-IPM solution was the only one which remained steadily below the Ground Truth level.

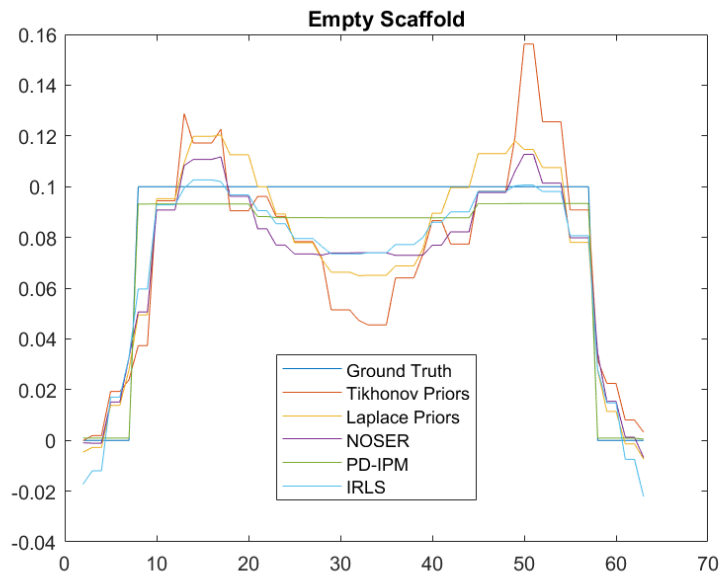


Figure 4.1: 1D section of the 3D surface of the reconstruction of the Empty Scaffold

4. Numerical Tests

E: OGNT			
α	ϵ_{slices}	ϵ_{c2f}	ϵ_{sol}
0.0001	0.3004	0.3428	0.00686
1.0e-5	0.3001	0.3388	0.006729
1.0e-6	0.3218	0.3592	0.006755
1.0e-7	1.679	1.571	0.0523
1.0e-8	2.971	2.782	0.2319
E: IGNL			
α	ϵ_{slices}	ϵ_{c2f}	ϵ_{sol}
0.0001	0.2394	0.294	0.0005302
1.0e-5	0.2426	0.2953	0.0001627
1.0e-6	0.2589	0.3141	0.0001576
1.0e-7	0.9628	1.086	0.0001621
E:NOSER			
α	ϵ_{slices}	ϵ_{c2f}	ϵ_{sol}
0.01	320.7	520.8	16.38
0.001	0.2522	0.3369	0.009631
0.0001	0.2358	0.2854	0.006568
1.0e-5	0.2435	0.292	0.006548
E:PDIPM			
α	ϵ_{slices}	ϵ_{c2f}	ϵ_{sol}
1.0e-7	0.2479	0.354	0.06874
1.0e-8	0.08929	0.1005	0.0692
1.0e-9	0.08622	0.09078	0.06935
1.0e-10	0.08638	0.09031	0.06938
E:IRLS			
α	ϵ_{slices}	ϵ_{c2f}	ϵ_{sol}
1.0e-5	0.3302	0.451	0.06922
1.0e-6	0.249	0.3294	0.06708
1.0e-7	0.2337	0.3232	0.0668
1.0e-8	0.236	0.3304	0.06683

Table 4.2: Model E

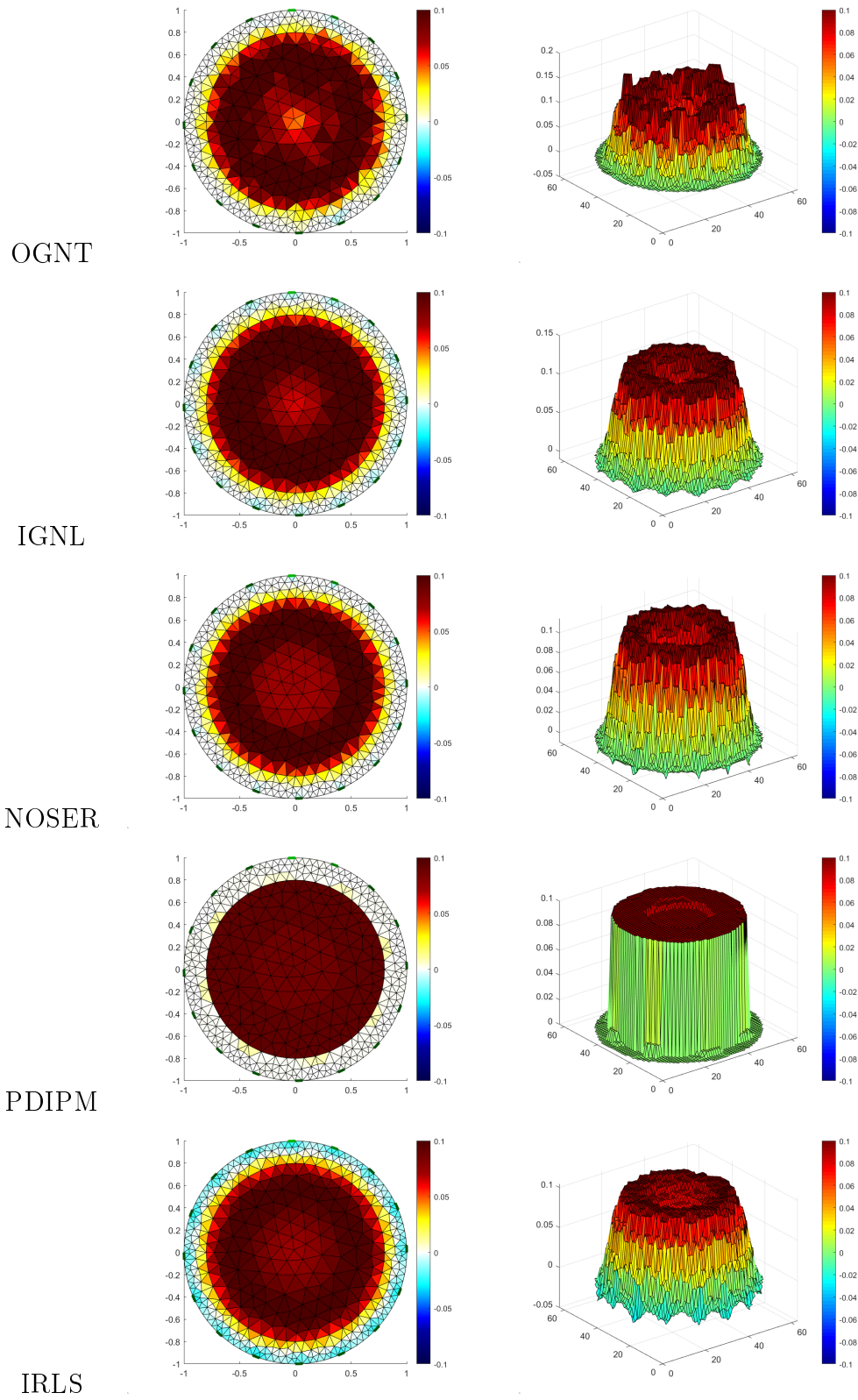


Table 4.3: Reconstruction for the E-test case.

The Piecewise Constant phantom

All methods fail to reconstruct the small circular negative variation and tend to delete it, though a certain subsidence in all reconstructions (as can be seen in Figure 4.2) around that region suggests that some kind of variation was detected. PD-IPM is again the only method which successfully reproduces the step change of the positive inclusion (while all the other methods provided smoothly increasing solutions). None recover the sharpen shape of the positive feature.

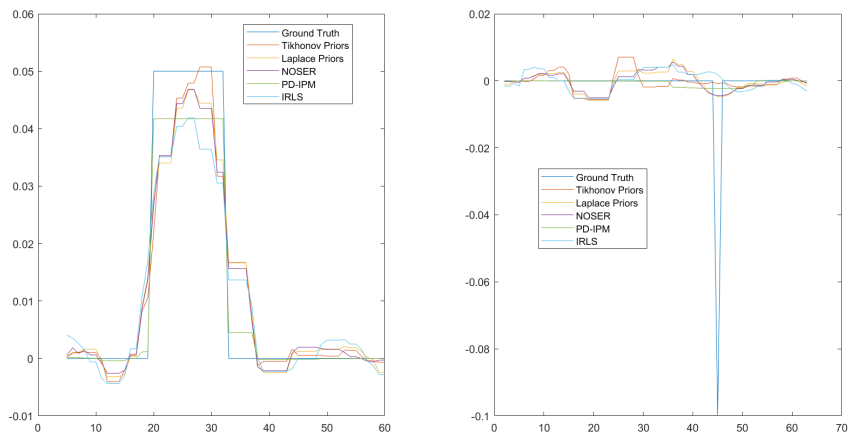


Figure 4.2: 1D section of the 3D surface reconstruction of the PC model

PC: OGNT			
α	ϵ_{slices}	ϵ_{c2f}	ϵ_{sol}
0.0001	0.585	0.8919	0.00334
1.0e-5	0.5476	0.8821	0.0009172
1.0e-6	0.5401	0.8803	0.001002
1.0e-7	0.539	0.8791	0.00114
1.0e-8	0.5564	0.8824	0.001487
PC: IGNL			
α	ϵ_{slices}	ϵ_{c2f}	ϵ_{sol}
0.0001	0.6052	0.8826	0.003167
1.0e-5	0.5567	0.8732	0.0001919
1.0e-6	0.5484	0.8729	1.35e-5
1.0e-7	0.5446	0.8604	6.657e-6
1.0e-8	0.5576	0.858	1.035e-7
PC:NOSER			
α	ϵ_{slices}	ϵ_{c2f}	ϵ_{sol}
0.01	0.6407	0.888	0.0145
0.001	0.5658	0.8685	0.001652
0.0001	0.5496	0.8696	0.00134
1.0e-5	0.5442	0.8595	0.001406
1.0e-6	0.5526	0.8495	0.001872
PC:PDIPM			
α	ϵ_{slices}	ϵ_{c2f}	ϵ_{sol}
1.0e-7	0.8376	0.9578	0.1689
1.0e-8	0.654	0.9076	0.03926
1.0e-9	0.5509	0.8742	0.01849
1.0e-10	0.4845	0.8523	0.01905
1.0e-11	0.4496	0.8443	0.01962
PC: IRLS			
α	ϵ_{slices}	ϵ_{c2f}	ϵ_{sol}
1.0e-6	0.6839	0.8869	0.01993
1.0e-7	0.6485	0.8795	0.01442
1.0e-8	0.5956	0.8828	0.01496
1.0e-9	0.581	0.9038	0.01607
1.0e-10	0.5797	0.9181	0.01634

Table 4.4: Model PC

4. Numerical Tests

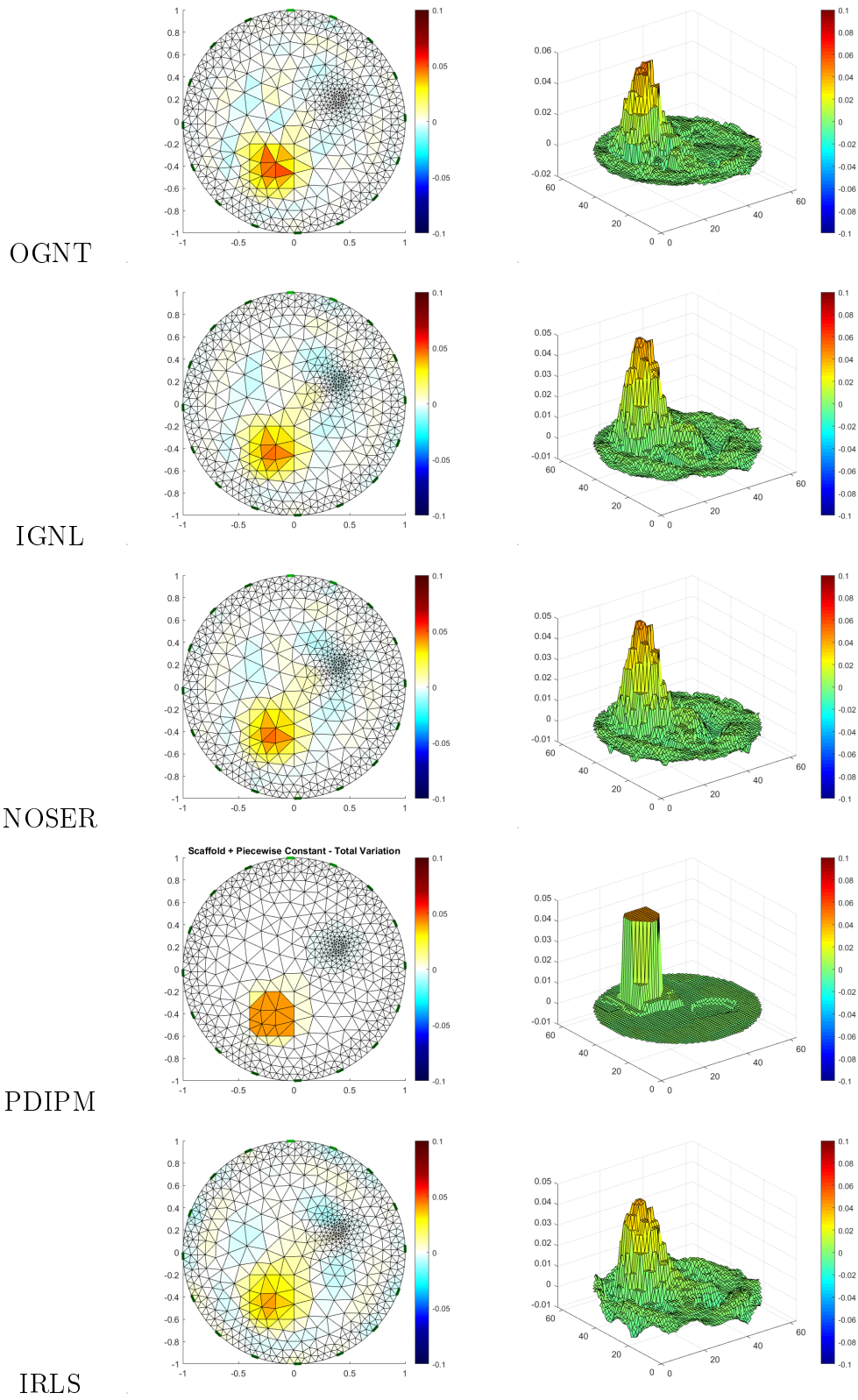


Table 4.5: Reconstruction for the PC-test case.

The Smooth Phantom

All methods in this case test managed to detect the correct regions, the correct shapes and the smooth behaviour of the inclusions. PD-IPM gained good quantitative values as reported in Table but it actually failed to detect the smoothness of the variations, defining a staircase-like solution, and reduced the highest reconstructed values.

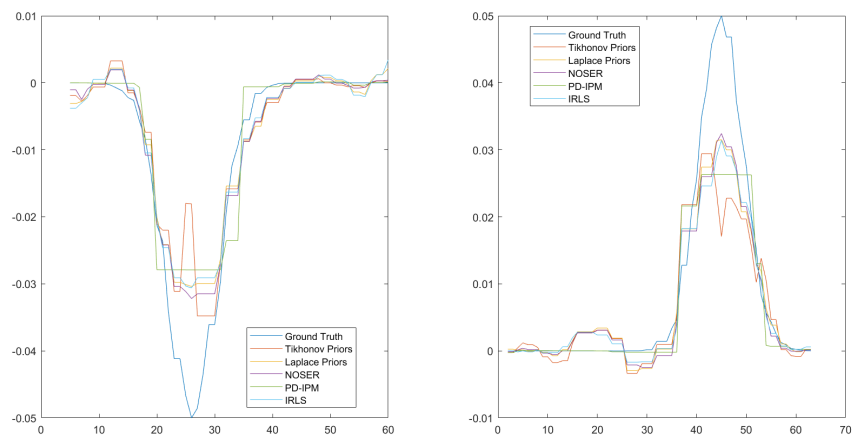


Figure 4.3: 1D section of the 3D surface reconstruction of the SM model

4. Numerical Tests

SM: OGNT			
α	ϵ_{slices}	ϵ_{c2f}	ϵ_{sol}
0.001	0.5818	0.6083	0.06796
0.0001	0.4313	0.4698	0.01311
1.0e-5	0.3895	0.4227	0.01407
1.0e-6	0.3989	0.4302	0.01422
1.0e-7	0.4476	0.461	0.01457
SM: IGNU			
α	ϵ_{slices}	ϵ_{c2f}	ϵ_{sol}
0.001	0.5178	0.5182	0.0335
0.0001	0.4045	0.4071	0.002644
1.0e-5	0.3428	0.3382	0.0001599
1.0e-6	0.3371	0.3358	1.834e-5
1.0e-7	0.363	0.3623	4.23e-6
SM:NOSER			
α	ϵ_{slices}	ϵ_{c2f}	ϵ_{sol}
0.01	0.443	0.4385	0.01726
0.001	0.34	0.3299	0.01317
0.0001	0.3226	0.3118	0.0138
1.0e-5	0.3406	0.3306	0.01398
1.0e-6	0.4403	0.4086	0.01473
SM:PDIPM			
α	ϵ_{slices}	ϵ_{c2f}	ϵ_{sol}
1.0e-10	0.4478	0.4542	0.0149
1.0e-11	0.3904	0.3898	0.01498
1.0e-12	0.3687	0.3698	0.01508
5.0e-13	0.3718	0.3756	0.01511
1.0e-13	0.4161	0.4194	0.0153
SM:IRLS			
α	ϵ_{slices}	ϵ_{c2f}	ϵ_{sol}
1.0e-8	0.3829	0.3846	0.01302
1.0e-9	0.3676	0.3789	0.0137
1.0e-10	0.3611	0.3739	0.01384
1.0e-11	0.3508	0.3621	0.01384
1.0e-12	0.355	0.3701	0.01389

Table 4.6: Model SM

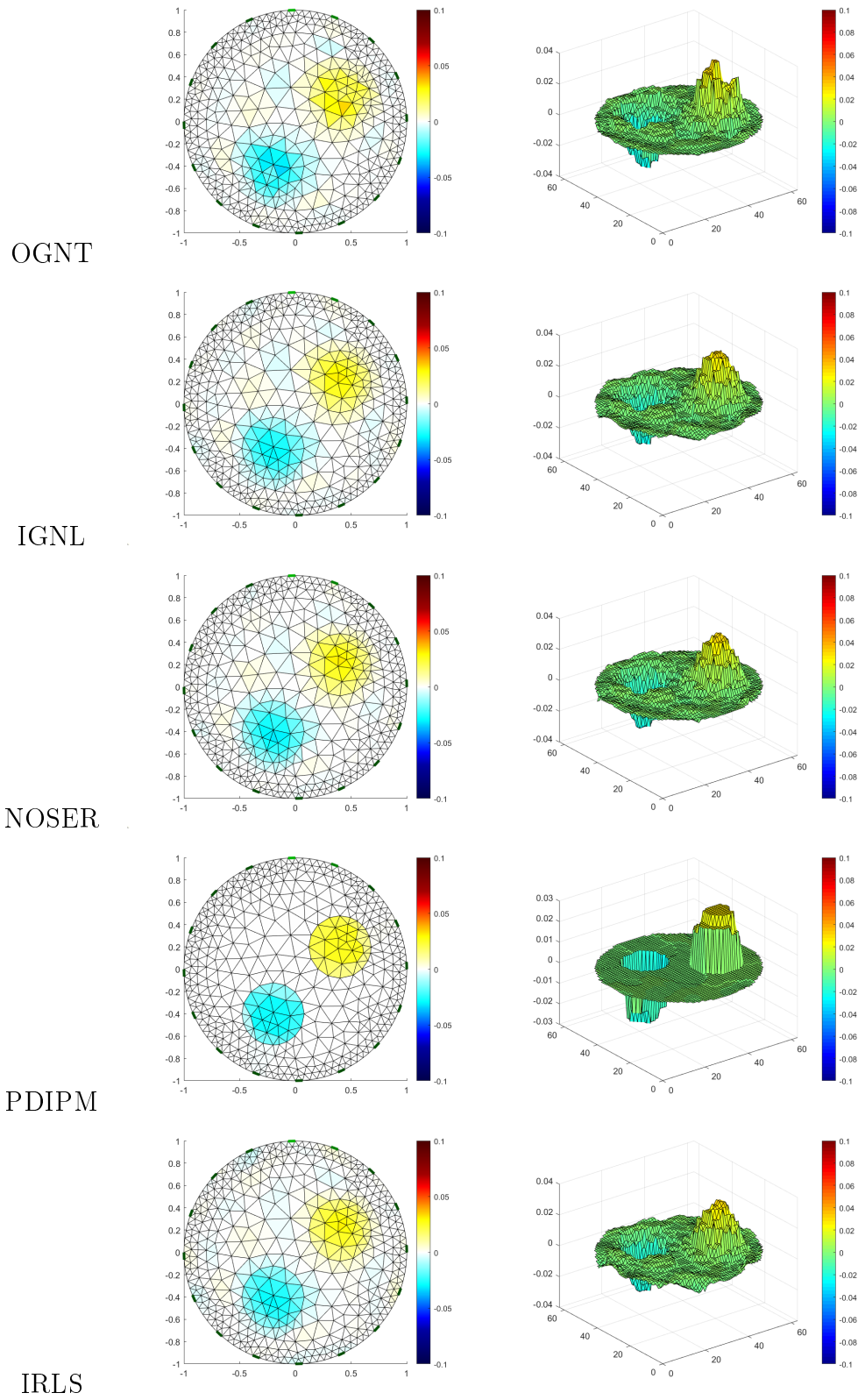


Table 4.7: Reconstruction for the SM-test case.

The Piecewise Smooth Phantom

All methods manage to detect the smooth inclusion with smooth slope, apart from PDIPM which as expected produces a staircase-like reconstruction. The inner squared variation was only detected by IGNL, NOSER and IRLS, as shown in Figure 4.4; PD-IPM only reported a small increase in the central region and OGNT defined an oscillating solution. None of the methods managed to accurately reconstruct the magnitude of the values of the conductivity change inside the squared region.

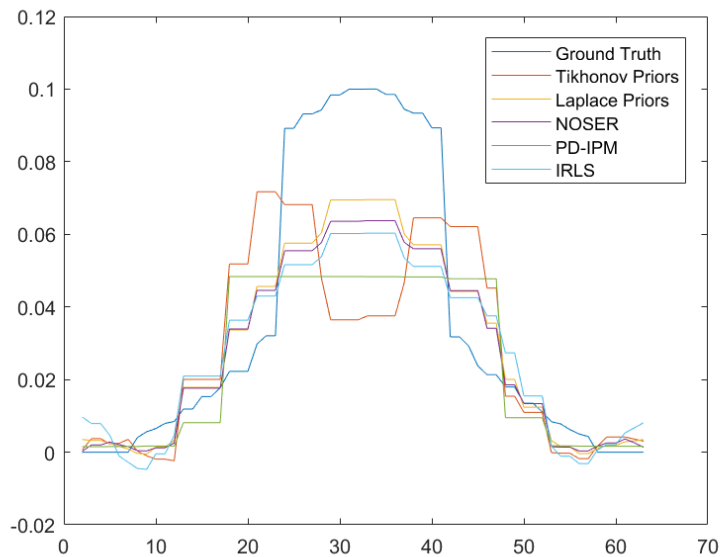


Figure 4.4: 1D section of the 3D surface reconstruction of the PS model

PS: OGNT			
α	ϵ_{slices}	ϵ_{c2f}	ϵ_{sol}
0.01	0.658	0.6734	0.1282
0.001	0.582	0.5764	0.01478
0.0001	0.5294	0.5261	0.00217
1.0e-5	0.5248	0.5225	0.001902
1.0e-6	0.5217	0.5191	0.001903
PS: IGNL			
α	ϵ_{slices}	ϵ_{c2f}	ϵ_{sol}
0.01	0.6161	0.6476	0.1581
0.001	0.456	0.4665	0.01116
0.0001	0.3669	0.3777	0.0004056
1.0e-5	0.3646	0.3775	1.004e-5
1.0e-6	0.3645	0.3779	1.087e-6
PS:NOSER			
α	ϵ_{slices}	ϵ_{c2f}	ϵ_{sol}
0.1	0.5252	0.5328	0.08515
0.01	0.4143	0.4128	0.006057
0.001	0.3784	0.3847	0.002009
0.0001	0.3779	0.3845	0.001983
1.0e-5	0.3779	0.3845	0.001982
PS:PDIPM			
α	ϵ_{slices}	ϵ_{c2f}	ϵ_{sol}
1.0e-8	0.5478	0.552	0.02736
1.0e-9	0.5414	0.5432	0.0274
1.0e-10	0.5393	0.5407	0.02738
1.0e-11	0.5364	0.5371	0.02735
1.0e-12	0.5347	0.5351	0.02734
PS:IRLS			
α	ϵ_{slices}	ϵ_{c2f}	ϵ_{sol}
1.0e-5	0.5676	0.6262	0.0315
1.0e-6	0.482	0.4867	0.02598
1.0e-7	0.45	0.4914	0.02639
1.0e-8	0.4473	0.5014	0.02671
1.0e-9	0.4472	0.5028	0.02675

Table 4.8: Model PS

4. Numerical Tests

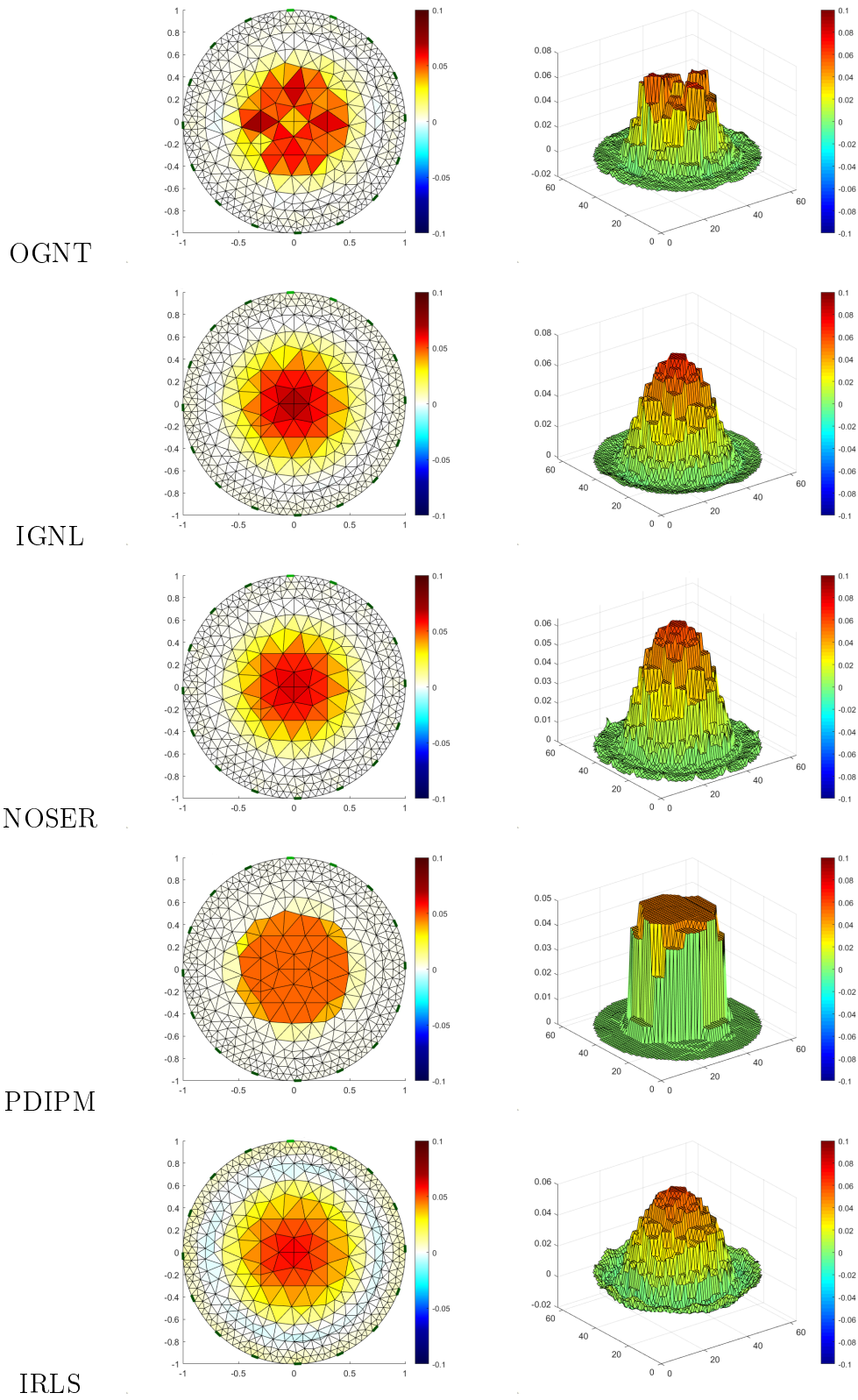


Table 4.9: Reconstruction for the PS-test case.

The Piecewise Constant & Smooth phantom

The two inclusions were detected by all the algorithms but PD-IPM was the only one that almost perfectly fitted the solution inside the shapes. As usual PD-IPM defined only piecewise constant values, while all the other algorithms tended to rather smooth variations. The smooth inclusion was the better reconstructed one, not only in terms of shape and behaviour but also in terms of values. Table 4.11 clearly shows that PD-IPM generated the best reconstruction in terms of mismatch with the conductivity ground truth, while IGNL defined the best fitting to the measured data.

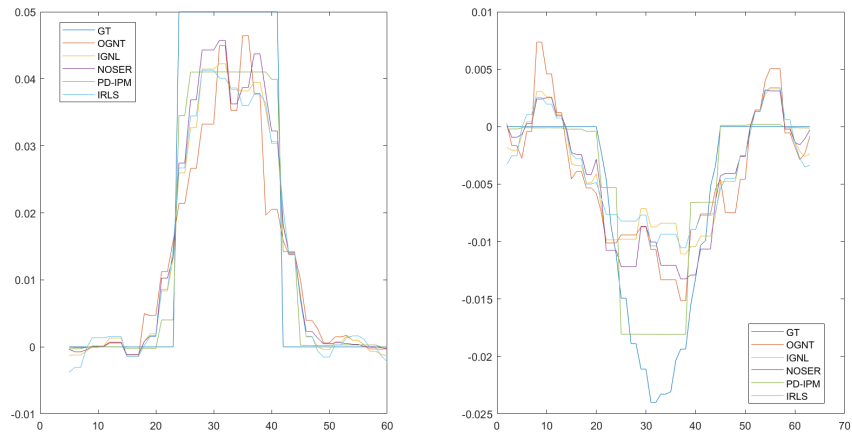


Figure 4.5: 1D section of the 3D surface reconstruction of the PCSM model: piecewise constant (left), smooth (right)

4. Numerical Tests

PCSM: OGNT			
α	ϵ_{slices}	ϵ_{c2f}	ϵ_{sol}
1.0e-5	0.5441	0.6247	0.01655
1.0e-6	0.5356	0.6088	0.0168
1.0e-7	0.5278	0.5933	0.01705
1.0e-8	0.5338	0.5931	0.0175
1.0e-9	0.534	0.5932	0.01752
PCSM: IGNL			
α	ϵ_{slices}	ϵ_{c2f}	ϵ_{sol}
0.0001	0.539	0.5951	0.003365
1.0e-5	0.4902	0.5388	0.0001818
1.0e-6	0.4829	0.5283	1.703e-5
1.0e-7	0.4749	0.5124	3.749e-6
1.0e-8	0.4822	0.5122	1.101e-7
PCSM:NOSER			
α	ϵ_{slices}	ϵ_{c2f}	ϵ_{sol}
0.0001	0.4918	0.5285	0.01927
1.0e-5	0.4845	0.5166	0.0194
1.0e-6	0.4845	0.5098	0.01984
1.0e-7	0.486	0.5105	0.01992
1.0e-8	0.4884	0.5125	0.01993
PCSM:PDIPM			
α	ϵ_{slices}	ϵ_{c2f}	ϵ_{sol}
1.0e-10	0.405	0.4386	0.02191
1.0e-11	0.3131	0.3402	0.02421
1.0e-12	0.2791	0.303	0.0247
1.0e-13	0.2664	0.2729	0.02447
1.0e-14	0.2945	0.3107	0.02372
PCSM:IRLS			
α	ϵ_{slices}	ϵ_{c2f}	ϵ_{sol}
1.0e-10	0.4959	0.5437	0.01942
1.0e-11	0.4833	0.5279	0.01948
1.0e-12	0.4744	0.5142	0.0196
1.0e-13	0.4662	0.5012	0.01964
1.0e-14	0.4631	0.4923	0.01985

Table 4.10: Model PCSM

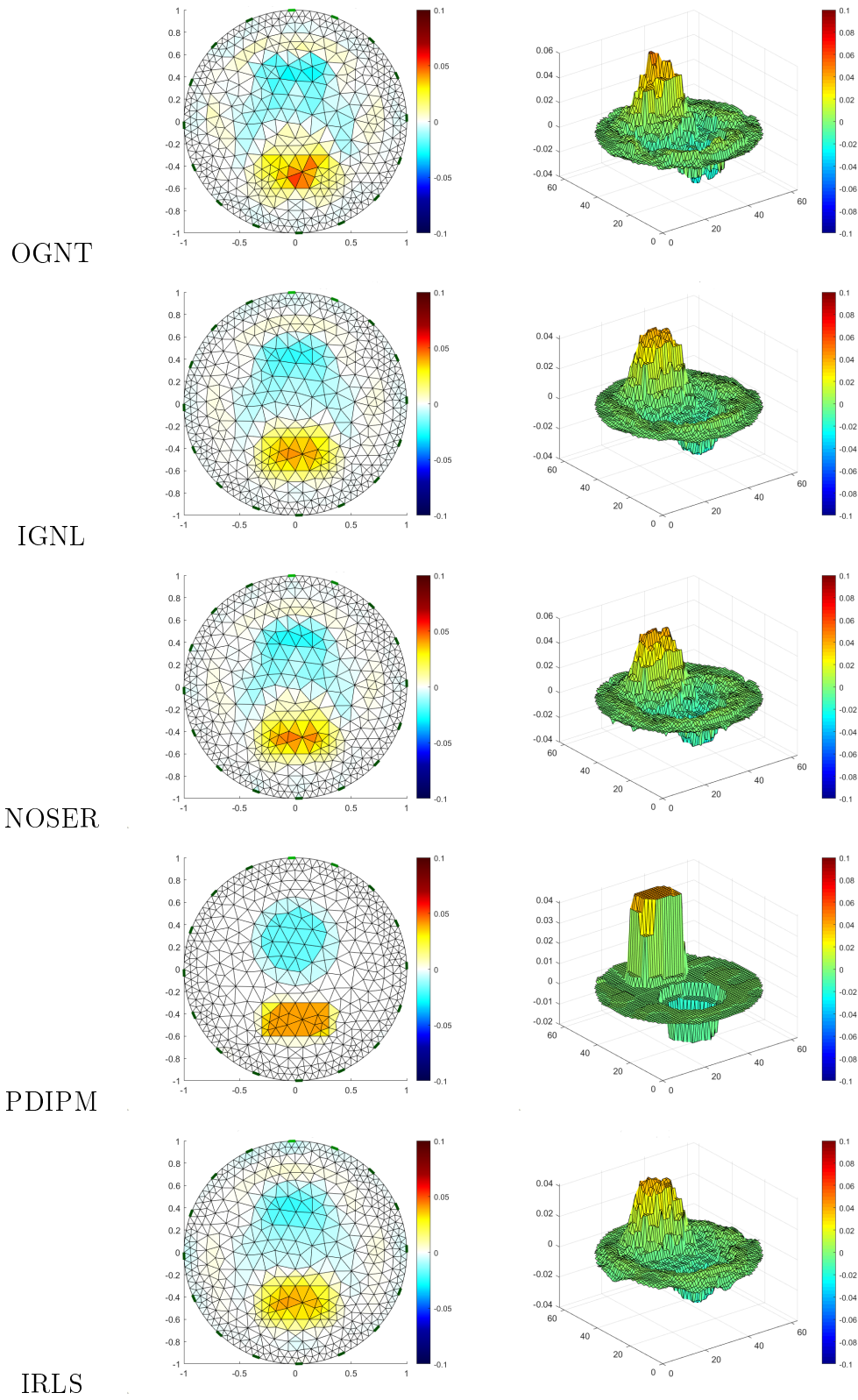


Table 4.11: Reconstruction for the PCSM-test case.

PD-IPM

The iterative algorithm for the PD-IPM method in EIDORS allows to keep the solution for each iteration, which might be interesting in order to investigate the properties of the method and its behaviour with respect to the different case tests. Figure 4.6 shows the evolution of the relative change for the Linearized Objective Function

$$\mathcal{J} = \|J\sigma - V_m\|_2^2 + \alpha TV(\sigma)$$

on which the stopping criterion of the algorithm is based. The stopping tolerance value was set to 10^{-16} and the maximum number of iterations `maxit` was set to 20. All models showed the same pattern for both parameters, with the first two iterations being the ones with highest relative change (10^0), then the third iteration lost 2 or 3 orders of magnitude. Starting from this point, the relative change started to increase until 10^{-1} (which was reached around iteration 10) and then slowly degraded until convergence. This pattern is evident in Figure 4.7 where the *slice projections* of 12 iterative solutions for each case test are shown. Clearly the detection of the regions and the general behaviour of the different conductivity distribution happened already in the first iteration and the successive iterations helped to lead to piecewise constant solutions and remove artefacts. Shown slices 2 to 5 (corresponding to iterations 2,4,6 and 7) are almost equivalent. Shown slice 6 and 7, corresponding to iteration 9 and 11, represent the steps where artefacts were almost completely removed and regions defined. The last slices are the ones corresponding to the decrease until convergence of the relative change and no modification can be visually detected.

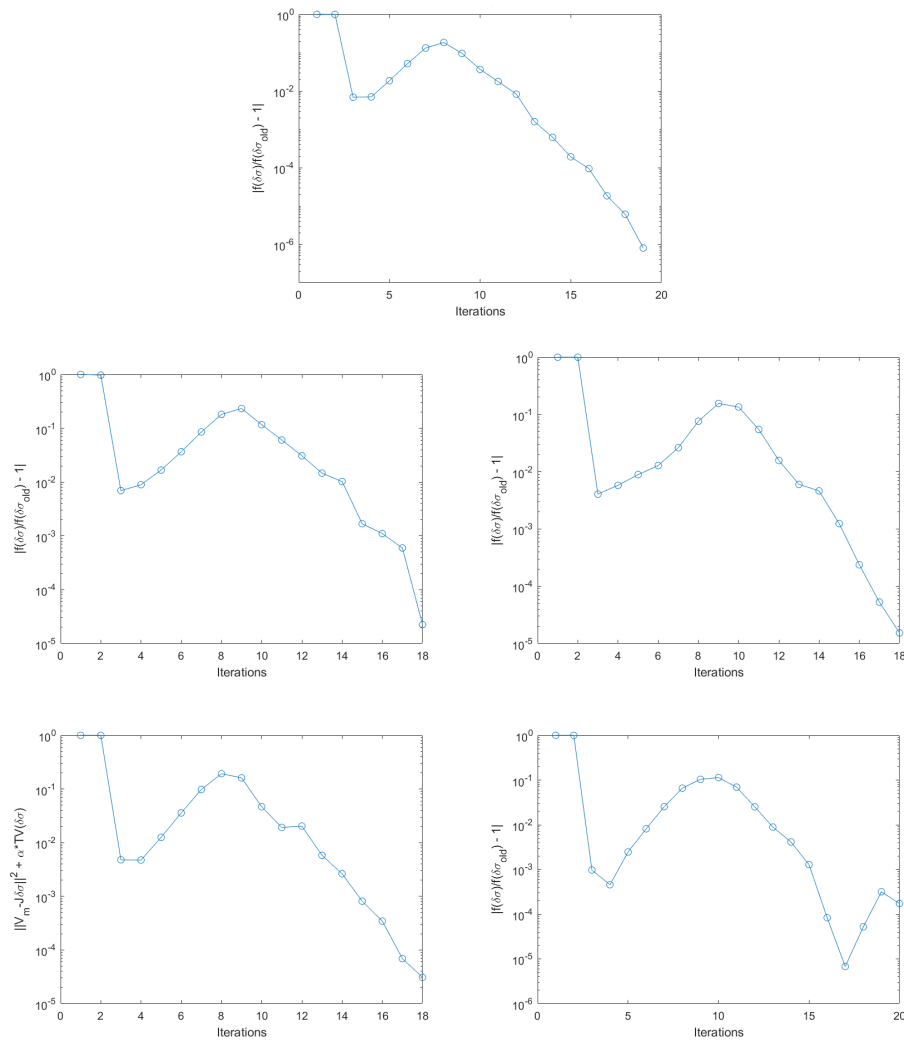


Figure 4.6: Relative change for the Objective Function $\mathcal{J}(\sigma)$ for the algorithm PDIPM: E-test, PC-test, SM-test, PS-test, PCSM-test.

4. Numerical Tests

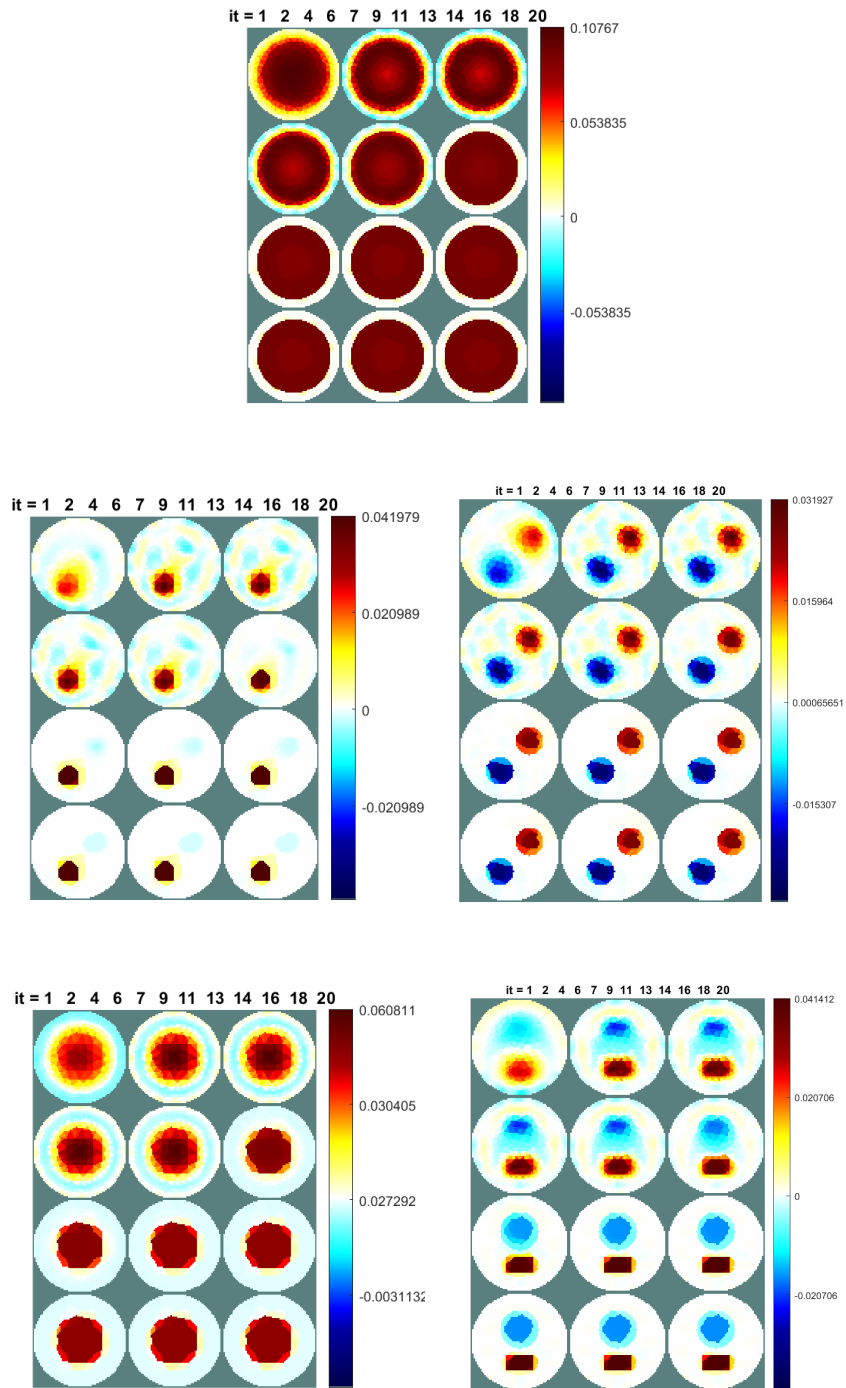


Figure 4.7: Evolution of the PDIPM algorithm's solutions: E-test, PC-test, SM-test, PS-test, PCSM-test.

Chapter 5

A Spatially-Adaptive Variational Method for EIT

In this chapter we present a new variational method for the resolution of the EIT inverse problem with difference imaging. The model belongs to the class EIT-L-NLR as it is built on a functional that includes the linearized version of the fidelity term and two nonlinear regularization terms. In particular we consider a smooth convex generalized Tikhonov regularization operator, consisting of a L_2 norm for the gradient of the conductivity, and a nonsmooth nonconvex TV-like operator for strong sparsity promotion. The action of these two penalties is weighted by a space variant function which locally defines whether to favour smoothing or sparsification. This variational model is nonconvex and nonsmooth so it deserves challenging solutions. We propose an ADMM-based iterative algorithm for the minimization of the introduced model. The idea behind this method comes from the Convex-Nonconvex approach [6], whose principle, as described in [20], is to define a functional which includes both smooth convex and non-smooth non-convex penalty terms, so that the total cost function is convex. Such result is achieved by offsetting the negative second derivatives of the nonconvex penalty term with the positive second derivatives of the convex terms. The advantage lies in the possibility to promote sparsity more strongly than it

can be achieved by only including convex terms and simultaneously maintain convexity of the general problem, so that one can rely on convex minimization approaches to determine the solution.

5.1 Variational Model

The proposed variational method solves the EIT inverse problem relying on the following minimization problem:

$$\begin{aligned} \min_{\sigma} \mathcal{J}(\sigma; \lambda, \eta, a) , \\ \mathcal{J}(\sigma; \lambda, \eta, a) := \frac{\lambda}{2} \int_{\Omega} (J\sigma - V_m)^2 d\Omega + \int_{\Omega} \frac{\eta(x)}{2} (\nabla\sigma)^2 d\Omega \\ + \int_{\Omega} \frac{(1 - \eta(x))}{2} \phi(|\nabla\sigma|; a) d\Omega , \end{aligned} \quad (5.1)$$

where $\lambda > 0$ is a weighting parameter for the fidelity term,

$$\eta : \Omega \subset \mathbb{R}^2 \rightarrow [0, 1]$$

is a space variant function that works as a trade-off for the smooth convex quadratic regularization term and the nonconvex nonsmooth regularization term, $\nabla\sigma$ is the conductivity gradient defined on Ω and

$$\phi(\cdot; a) : [0, +\infty) \rightarrow \mathbb{R}$$

is a parameterized, non-convex penalty function with parameter $a \geq 0$, which controls the degree of non-convexity and will be referred to as the *concavity parameter*. As function ϕ , a rescaled and reparameterized version of the minmax concave penalty function [37] was chosen, yielding the following piecewise quadratic function:

$$\phi(t; a) = \begin{cases} -\frac{a}{2}t^2 + \sqrt{2}at & \text{for } t \in [0, \sqrt{2/a}) \\ 1 & \text{for } t \in [\sqrt{2/a}, \infty) \end{cases} \quad (5.2)$$

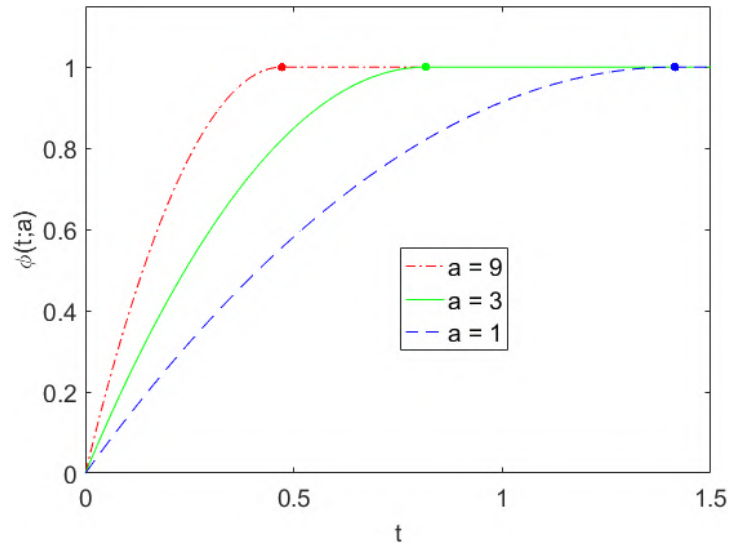


Figure 5.1: Plots of the penalty $\phi(t; a)$ in (5.2) for different a values. Solid dots indicate points separating, on each penalty graph, the two pieces associated with sub-domains $[0, \sqrt{2/a})$, $[\sqrt{2/a}, \infty)$

Figure 5.1 illustrates $\phi(t; a)$ for different values of the concavity parameter $a \in \{1, 3, 9\}$. In this setting, function ϕ assigns a different value to each entry of the gradient.

5.2 Discretization

Let $\mathcal{M} = (\mathcal{V}, \mathcal{T}, \mathcal{E})$ be the triangle mesh approximating the planar domain $\Omega \subset \mathbb{R}^2$ which is defined in Section 3.1. Conductivity difference $\sigma : \Omega \rightarrow \mathbb{R}$ is approximated by a piecewise constant function which is sampled over the triangles of the mesh.

The fidelity term in (5.1)

$$\int_{\Omega} (J\sigma - V_m)^2 d\Omega \quad (5.3)$$

is discretized considering the features of the Forward Operator F described in section 2.1.3, of which J represents a linear approximation. The first

5. A Spatially-Adaptive Variational Method for EIT

property to consider is the fact that the Forward Operator relates the inner conductivity and the boundary voltages, thus defining a function that is nonzero only on the boundary with electrodes Γ as in (2.9) and vanishes elsewhere. This allows to reformulate (5.3) as:

$$\int_{\Omega} (J\sigma - V_m)^2 d\Omega = \int_{\partial\Omega} (J\sigma - V_m)^2 dS = \int_{\Gamma} (J\sigma - V_m)^2 dS. \quad (5.4)$$

A further consideration is the fact that the image of the Forward Operator in the CEM is sampled and vectorized following two steps: the first one corresponds to the choice of an opposite injection pair d and the second step corresponds to the choice of an available adjacent measuring pair m_d (in the considered stimulation pattern, electrodes involved in the injection pair are not included in the measuring pairs). This leads to the following identities:

$$\int_{\Gamma} (J\sigma - V_m)^2 dS = \sum_{d=1}^L \int_{\Gamma} ([J\sigma]_d - [V_m]_d)^2 dS = \quad (5.5)$$

$$= \sum_{d=1}^L \sum_{m_d=1}^M \int_{\Gamma} ([J\sigma]_{d,m_d} - [V_m]_{d,m_d})^2 dS. \quad (5.6)$$

where $L = 16$ is the number of electrodes and $M = 12$ corresponds to the number of measurements for each injecting pair. Notice that the integrand of every term in the summation in (5.6) is only defined on the corresponding pair of measuring electrodes, on which the functions are assumed to be constant. Let $\{E_{m_d}, E_{m_d+1}\}$ be the pair of measuring electrodes and $E_{m_d} \cup E_{m_d+1}$ be their union as a portion of the boundary with electrodes Γ . Assuming $|E|$ is the measure of each electrode and this is assumed to be equal for all electrodes, then we can define a factor $2|E|$ for all $d = 1, \dots, L$ and $m_d = 1, \dots, M$.

$$\begin{aligned}
& \sum_{d=1}^L \sum_{m_d=1}^M \int_{\Gamma} ([J\sigma]_{d,m_d} - [V_m]_{d,m_d})^2 dS = \\
& = \sum_{d=1}^L \sum_{m_d=1}^M \int_{G_{m_d}} ([J\sigma]_{d,m_d} - [V_m]_{d,m_d})^2 dS = \\
& = \sum_{d=1}^L \sum_{m_d=1}^M 2|E| ([J\sigma]_{d,m_d} - [V_m]_{d,m_d})^2 = \\
& = 2|E| \|J\sigma - V_m\|_2^2.
\end{aligned}$$

In the respect of the discrete setting, the gradient operator is discretized as matrix $D \in \mathbb{R}^{n_e \times n_T}$ which is the same operator defined in (3.15) that assigns to each edge the value of the absolute difference between the conductivity values of the two triangles sharing that edge, weighted by the length of the edge itself. It can be defined as the product of two matrices: a diagonal matrix $\Lambda \in \mathbb{R}^{n_e \times n_e}$, whose j -th diagonal element is equal to the length of the corresponding edge, and a matrix $\tilde{D} \in \mathbb{R}^{n_e \times n_T}$ in which each row d_j corresponding to the j th edge is

$$d_j = (0, \dots, -1, 0, \dots, 0, 1, \dots, 0),$$

and the nonzero elements correspond to two adjacent triangles sharing the j th edge. Hence, in the respect of the discretization, the model is anisotropic.

The Jacobian operator J is discretized with respect to the domain decomposition and the subsequent piecewise constant approximation of σ , according to Equation (2.29). It is computed with respect to an initial guess for the conductivity distribution and it is not updated throughout the procedure.

Since conductivity is defined as piecewise constant on the elements in \mathcal{T} and $\eta(x)$ is sampled on the edges in \mathcal{E} , the discretization for the smooth

5. A Spatially-Adaptive Variational Method for EIT

convex quadratic and the nonconvex nonsmooth penalty terms is

$$\int_{\Omega} \frac{\eta(x)}{2} (\nabla \sigma)^2 d\Omega = \sum_{j=1}^{n_e} l_j \frac{\eta_j}{2} (D\sigma)_j^2$$

$$\int_{\Omega} \frac{(1 - \eta(x))}{2} \phi(|\nabla \sigma|; a) d\Omega = \sum_{j=1}^{n_e} l_j \frac{(1 - \eta_j)}{2} \phi(|(D\sigma)_j|; a)$$

where l_j is the length of e_j .

In conclusion, the discretized functional on \mathcal{M} becomes

$$\mathcal{J}(\sigma; \lambda, \eta, a) := \lambda |E| \|J\sigma - V_m\|^2 + \sum_{j=1}^{n_e} l_j \left\{ \frac{\eta_j}{2} (D\sigma)_j^2 + \frac{(1 - \eta_j)}{2} \phi(|(D\sigma)_j|; a) \right\}. \quad (5.7)$$

5.3 Spatially varying η function

In this section the idea of using a space varying weighting function $\eta(t)$ for the penalty terms in the CNC model (5.1) is described. The aim is to define a way to distinguish the regions where to prioritize the action of the smoothing term and the ones where to promote sparsity instead, so that mixed conductivity configurations such as the *PCSM phantom* from Chapter 4 can be accurately reconstructed. To this end, a certain prior knowledge about the solution is then required, but unlike what happens in restoration problems, where the input data is a degraded version of the solution that is looked for and can therefore provide some information about e.g. the boundaries of the regions, in EIT solution and data are defined on different spaces. Two scenarios can thus be identified: (a) the configuration inside the tank is known or visible, which allows to construct an *ad hoc* mesh and manually assign the values of the weighting function η in the different regions; (b) the setup is *blind*, meaning no information is provided about the content of the tank.

A possible procedure in case (b) is to consider the solution σ_0 obtained by a preliminary step of the proposed method with $\eta(x) \equiv 0 \quad x \in \Omega$ as the starting point for the space-variant approach. This generates a piecewise constant reconstruction σ_0 where sharp edges and step changes are more promoted than smooth variations. The idea is then to compute the gradient $\nabla\sigma_0$ of the reference conductivity difference and obtain a η -map by applying the bounded nonnegative continuous and monotonically descending function

$$\eta(t) = \frac{1}{(1 + (t/\kappa)^2)} \quad (5.8)$$

where $t = \|\nabla\sigma_0\|_2^2$. The function (5.8) is used in image processing as an edge detector.

5.4 Applying ADMM to the proposed model

In order to minimize the functional in model (5.1), the alternating direction method of multipliers (ADMM) is applied on the triangulated mesh domain \mathcal{M} . Considering the discretizations described in the previous section and introducing the auxiliary variable $t \in \mathbb{R}^{n_e}$, problem (5.1) is reformulated in the following equivalent discrete form:

$$\{\sigma^*, t^*\} \leftarrow \arg \min_{\sigma, t} \left\{ |E|\lambda \|V_m - J\sigma\|_2^2 + \sum_{j=1}^{n_e} l_j \left[\frac{\eta_j}{2} t_j^2 + \frac{(1 - \eta_j)}{2} \phi(|t_j|; a) \right] \right\} \quad (5.9)$$

$$\text{subject to : } \quad t = D\sigma, \quad (5.10)$$

where Jacobian J is computed with respect to an initial conductivity distribution $\sigma^{(0)}$ and not updated throughout the iterative scheme.

To solve the constrained optimization problem (5.9)-(5.10) the augmented

5. A Spatially-Adaptive Variational Method for EIT

Lagrangian functional is defined as

$$\begin{aligned} \mathcal{L}(\sigma, t; \rho; \lambda, \eta, a) = & |E|\lambda\|V_m - J\sigma\|_2^2 + \sum_{j=1}^{n_e} l_j \left\{ \frac{\eta_j}{2} t_j^2 + \frac{(1-\eta_j)}{2} \phi(|t_j|; a) \right\} \\ & - \langle \rho, t - D\sigma \rangle + \frac{\beta}{2} \|t - D\sigma\|_2^2, \end{aligned} \quad (5.11)$$

where $\beta > 0$ is a scalar penalty parameter and $\rho \in \mathbb{R}^{n_e}$ is the vector of Lagrange multipliers associated with the linear constraint $t = D\sigma$ in (5.11). The following saddle-point problem is then considered:

$$\begin{aligned} \text{Find } & (\sigma^*, t^*; \rho^*) \in \mathbb{R}^{n_T} \times \mathbb{R}^{n_e} \times \mathbb{R}^{n_e} \\ \text{s.t. } & \mathcal{L}(\sigma^*, t^*; \rho; \lambda, \eta, a) \leq \mathcal{L}(\sigma^*, t^*; \rho^*; \lambda, \eta, a) \leq \mathcal{L}(\sigma, t; \rho^*; \lambda, \eta, a) \\ & \forall (\sigma, t; \rho) \in \mathbb{R}^{n_T} \times \mathbb{R}^{n_e} \times \mathbb{R}^{n_e}. \end{aligned} \quad (5.12)$$

Given vectors $\sigma^{(k)}$ and $\rho^{(k)}$ computed at the k -th iteration (or initialized if $k = 0$), the $(k+1)$ -th iteration of the ADMM-based iterative scheme applied to the solution of the saddle-point problem (5.11)–(5.12) is splitted into the following three sub-problems:

$$t^{(k+1)} \leftarrow \arg \min_{t \in \mathbb{R}^{n_e}} \mathcal{L}(\sigma^{(k)}, t; \rho^{(k)}; \lambda, \eta, a) \quad (5.13)$$

$$\sigma^{(k+1)} \leftarrow \arg \min_{\sigma \in \mathbb{R}^{n_T}} \mathcal{L}(\sigma, t^{(k+1)}; \rho^{(k)}; \lambda, \eta, a) \quad (5.14)$$

$$\rho^{(k+1)} \leftarrow \rho^{(k)} - \beta (t^{(k+1)} - D\sigma^{(k+1)}) \quad (5.15)$$

Remark 5.1. The minimization sub-problems are all strictly convex and admit a unique solution under proper conditions (see Prop. 5.3), but this is not sufficient to guarantee the convergence of the overall ADMM algorithm. We will further investigate this topic in a future work.

In the following sections the methods to tackle the two minimization sub-problems (5.13) and (5.14) for the primal variables will be described in

detail.

5.4.1 Solving the sub-problem for t

Sub-problem (5.13) can be reformulated as follows:

$$t^{(k+1)} \leftarrow \arg \min_{t \in \mathbb{R}^{n_e}} \sum_{j=1}^{n_e} \left\{ l_j \frac{\eta_j}{2} t_j^2 + l_j \frac{(1-\eta_j)}{2} \phi(|t_j|; a) - \rho_j^{(k)} t_j + \frac{\beta}{2} (t_j - (D\sigma^{(k)})_j)^2 \right\}. \quad (5.16)$$

Considering the last two terms of each summation and adding the constant terms $(D\sigma^{(k)})_j \rho_j^{(k)}$ and $\frac{1}{2\beta} (\rho_j^{(k)})^2$ yields:

$$\begin{aligned} \arg \min_{t \in \mathbb{R}} \left\{ -\rho_j^{(k)} t + \frac{\beta}{2} (t - (D\sigma^{(k)})_j)^2 \right\} &= \\ &= \arg \min_{t \in \mathbb{R}} \left\{ -\rho_j^{(k)} t + \frac{\beta}{2} (t - (D\sigma^{(k)})_j)^2 + (D\sigma^{(k)})_j \rho_j^{(k)} + \frac{1}{2\beta} (\rho_j^{(k)})^2 \right\} = \\ &= \arg \min_{t \in \mathbb{R}} \left\{ \frac{\beta}{2} (t - (D\sigma^{(k)})_j - \frac{1}{\beta} \rho_j^{(k)})^2 \right\} = \\ &= \arg \min_{t \in \mathbb{R}} \left\{ \frac{\beta}{2} (t - r_j^{(k)})^2 \right\} \end{aligned}$$

where

$$r_j^{(k)} = (D\sigma^{(k)})_j + \frac{1}{\beta} \rho_j^{(k)}, \quad r_j^{(k)} \in \mathbb{R}.$$

This leads to the following formulation for each of the n_e subproblems:

$$t_j^{(k+1)} \leftarrow \arg \min_{t \in \mathbb{R}} \left\{ l_j \frac{\eta_j}{2} t^2 + l_j \frac{(1-\eta_j)}{2} \phi(|t|; a) + \frac{\beta}{2} (t - r_j^{(k)})^2 \right\} \quad (5.17)$$

and equivalently, defining

$$\tilde{\beta}_j = \frac{\beta}{l_j}, \quad \tilde{\beta}_j \in \mathbb{R}$$

one obtains

$$t_j^{(k+1)} \leftarrow \arg \min_{t \in \mathbb{R}} \left\{ \frac{\eta_j}{2} t^2 + \frac{(1-\eta_j)}{2} \phi(|t|; a) + \frac{\tilde{\beta}_j}{2} (t - r_j^{(k)})^2 \right\}. \quad (5.18)$$

5. A Spatially-Adaptive Variational Method for EIT

Lemma 5.2. *Let $k_1, k_2 \in \mathbb{R}$ and $z_1, z_2 \in \mathbb{R}^m$. Then, for any $z \in \mathbb{R}^m$ we have*

$$\begin{aligned} \frac{k_1}{2} \|z - z_1\|_2^2 + \frac{k_2}{2} \|z - z_2\|_2^2 &= \frac{k_1 + k_2}{2} \left\| z - \frac{1}{k_1 + k_2} (k_1 z_1 + k_2 z_2) \right\|_2^2 \\ &+ \frac{k_1 k_2}{2(k_1 + k_2)} \|z_1 - z_2\|_2^2. \end{aligned} \quad (5.19)$$

Using Lemma 5.2, the problem (5.18) can be rewritten as

$$t_j^{(k+1)} \leftarrow \arg \min_{t \in \mathbb{R}} \left\{ \frac{\alpha_j}{2} (t - \tilde{r}_j^{(k)})^2 + \phi(|t|, a) \right\} \quad (5.20)$$

with

$$\alpha_j := 2 \left(\frac{\eta_j + \tilde{\beta}_j}{1 - \eta_j} \right), \quad \tilde{r}_j^{(k)} := \left(\frac{\tilde{\beta}_j}{\eta_j + \tilde{\beta}_j} \right) r_j^{(k)}. \quad (5.21)$$

Following proposition 5.3 the problem in (5.20) is strongly convex if and only if the following conditions hold:

$$\tilde{\beta}_j > \frac{a(1 - \eta_j) - 2\eta_j}{2} \quad \text{for } j = 1, \dots, n_e \quad (5.22)$$

$$\beta > l_j \left(\frac{a(1 - \eta_j) - 2\eta_j}{2} \right) \quad \text{for } j = 1, \dots, n_e \quad (5.23)$$

In case condition (5.23) is satisfied, the unique solutions of the strongly convex problems in (5.20) can be obtained using the soft-thresholding operator defined in (5.29)–(5.30) of Proposition 5.3, that is:

$$t_j^{(k+1)} = \xi^{(k+1)} \tilde{r}_j^{(k+1)} = \min \left\{ \max \left\{ \nu_j - \zeta_j / |\tilde{r}_j^{(k+1)}|, 0 \right\}, 1 \right\} \tilde{r}_j^{(k+1)}, \quad (5.24)$$

where

$$\nu_j = \frac{\alpha_j}{\alpha_j - a}, \quad \zeta_j = \frac{\sqrt{2a}}{\alpha_j - a}. \quad (5.25)$$

Proposition 5.3. *Let $\phi(\cdot; a) : \mathbb{R}_+ \rightarrow \mathbb{R}$ be the penalty function defined in (5.2), $r \in \mathbb{R}^m$ a given constant vector and $a \in \mathbb{R}_+$, $\alpha \in \mathbb{R}_+^*$ two (free)*

parameters. Then, the function

$$\theta(z) := \phi(\|z\|_2; a) + \frac{\alpha}{2} \|z - r\|_2^2, \quad z \in \mathbb{R}^m, \quad (5.26)$$

is strongly convex if and only if the following condition is satisfied:

$$\alpha > a. \quad (5.27)$$

Moreover, in case that (5.27) holds, the strongly convex minimization problem

$$\arg \min_{z \in \mathbb{R}^m} \theta(z) \quad (5.28)$$

admits the unique solution $z^* \in \mathbb{R}^m$ given by the following shrinkage operator:

$$z^* = \xi^* r, \quad \text{with } \xi^* \in [0, 1], \text{ in particular :} \quad (5.29)$$

$$\xi^* = \min \{ \max \{ \nu - \zeta / \|r\|_2, 0 \}, 1 \}, \quad (5.30)$$

where

$$\nu = \frac{\alpha}{\alpha - a}, \quad \zeta = \frac{\sqrt{2a}}{\alpha - a}. \quad (5.31)$$

5.4.2 Solving the sub-problem for σ

The minimization sub-problem for σ in (5.14), if constants are omitted, can be rewritten as follows:

$$\sigma^{(k+1)} \leftarrow \arg \min_{\sigma \in \mathbb{R}^{n_T}} \left\{ |E|\lambda| \|V_m - J\sigma\|_2^2 + \langle \rho^{(k)}, D\sigma \rangle + \frac{\beta}{2} \|t^{(k+1)} - D\sigma\|_2^2 \right\}, \quad (5.32)$$

The quadratic minimization problem (5.32) has the following first-order optimality conditions

$$2|E|\lambda|(-J)^T(V_m - J\sigma) + D^T\rho + \beta(-D^T)(t - D\sigma) = 0 \quad (5.33)$$

5. A Spatially-Adaptive Variational Method for EIT

which lead to the following linear system:

$$\left(J^T J + \frac{\beta}{2|E|\lambda} D^T D \right) \sigma = J^T V_m + \frac{\beta}{2|E|\lambda} D^T \left(t^{(k+1)} - \frac{1}{\beta} \rho^{(k)} \right). \quad (5.34)$$

Since $D^T D$ is symmetric and the ratio $\frac{\beta}{2|E|\lambda}$ is positive, the $n_T \times n_T$ coefficient matrix of the linear system (5.34) is symmetric positive semi-definite.

5.4.3 Special Case

If $\eta \equiv 1$, then (5.1) simplifies to the following minimization problem

$$\begin{aligned} & \min_{\sigma} \mathcal{J}(\sigma; \lambda, a), \\ \mathcal{J}(\sigma; \lambda, a) & := \frac{\lambda}{2} \int_{\Omega} (J\sigma - V_m)^2 d\Omega + \frac{1}{2} \int_{\Omega} (\nabla\sigma)^2 d\Omega \end{aligned} \quad (5.35)$$

with the equivalent discrete form for \mathcal{J} corresponding to a Tikhonov regularization functional

$$\mathcal{J}(\sigma; \lambda, \eta, a) := |E|\lambda \|J\sigma - V_m\|_2^2 + \|D_{\Lambda}\sigma\|_2^2. \quad (5.36)$$

where $D_{\Lambda} = \sqrt{\Lambda}D$. The solution σ^* can therefore be found by solving the linear system arising from optimality condition

$$J^T (J\sigma - V_m) + \frac{1}{2|E|\lambda} D_{\Lambda}^T D_{\Lambda} \sigma = 0 \quad (5.37)$$

$$\left(J^T J + \frac{1}{2|E|\lambda} D_{\Lambda}^T D_{\Lambda} \right) \sigma = J^T V_m. \quad (5.38)$$

5.4.4 SAEiT _{η} : an ADMM-type algorithm

The ADMM-based algorithm for the Space Adaptive method for Electrical Impedance Tomography (SAEiT) is given in Algorithm 1. The stopping criterion is based on the relative change of the reconstructed conductivity

between two successive steps

$$\frac{\|\sigma^{(k+1)} - \sigma^{(k)}\|_2^2}{\|\sigma^{(k)}\|_2^2} < tol \quad (5.39)$$

Algorithm 1 SAEiT $_\eta$ for the solution of (5.1)

inputs: voltage measurements $V_m \in \mathbb{R}^{n_m}$, η -map $\eta : \mathcal{E} \rightarrow [0, 1]^{n_e}$,
output: reconstructed conductivity difference $\sigma^* \in \mathbb{R}^{n_T}$

parameters: MODEL: · concavity parameter $a \geq 0$ for $\phi(\cdot; a) : \mathbb{R}_+ \rightarrow \mathbb{R}_+$
· data fidelity parameter $\lambda > 0$
· electrode measure $|E| > 0$
ADMM: · $\beta > 0$

initialization: $\sigma^{(0)} = \text{zeros}(n_T, 1)$, $\rho^{(0)} = \text{zeros}(n_e, 1)$
compute gradient operator $D \in \mathbb{R}^{n_T \times n_e}$

for $k = 0, 1, 2, \dots$ *until convergence* **do:**
 for $j = 0, 1, 2, \dots$ *until* n_e **do:**
 % update parameters:
 · set $\alpha_j^{(k+1)}$ and $\tilde{r}_j^{(k+1)}$ by (5.21)
 · set $\xi_j^{(k+1)}$ by (5.30)
 % subproblem for t:
 · compute $t_j^{(k+1)}$ by (5.24)
 end
 % subproblem for σ :
 · compute $\sigma^{(k+1)}$ by solving the linear system (5.34)
 % update dual variables ρ :
 · compute $\rho^{(k+1)} = \rho^{(k)} - \beta (t^{(k+1)} - D\sigma^{(k+1)})$
end
 $\sigma^* = \sigma^{(k+1)}$

Chapter 6

Numerical Experiments

In this chapter we illustrate a group of examples that show the characteristics of the proposed Spatially Adaptive method for Electrical Impedance Tomography (SAEiT). Data are considered both with and without noise in order to assess the stability of the algorithm (the generation of synthetic noise is described in Subsection 6.1). The performance is compared to the one of the methods described and tested in Chapters 3 and 4.

All examples simulate a circular tank of radius $r_0 = 1$ with 1 ring of 16 electrodes. Drive current level in Ampere is set to 0.1 and the conductivity of the background liquid is set to $1Sm^{-1}$. Measurements are generated via the same *opposite injection - adjacent measurement* protocol used in Chapter 4 and illustrated in Figure 2.1a.

The most general scheme for the algorithm is described by the following three steps:

- SAEiT₀: the spatially adaptive method is applied with $\eta \equiv 0$ in order to generate the preliminary solution σ_0 that allows to compute the space-variant η -map;
- η -map detection performed via a thresholding procedure on the edge-based gradient of conductivity distribution σ_0 ;

- SAEiT $_{\eta}$: the spatially adaptive method is applied with space-variant η -map.

The performance is assessed both qualitatively and quantitatively. The quantitative analysis is performed via two of the error metrics described in Chapter 4: the *slice metric* that gauges how well the original conductivity distribution is reconstructed (it can only be applied when a Ground Truth is provided), and the *relative solution error* which determines how well the reconstructed conductivity can reproduce the input data. Unlike what described in Chapter 4, the *slice metric* is computed on a 576×576 slice matrix, as the experiments described in the present chapter are carried out on finer meshes.

6.1 Adding Noise to the simulated data

If the data model is

$$F(\sigma) = V_m$$

then introducing a noise vector $e \approx \mathcal{N}(0, s_e^2)$ with $\|e\|_2^2 = n_m s_e^2$ (n_m is the number of data) of additive white Gaussian noise (AWGN) of standard deviation s_e and zero mean yields the corrupted measurement vector

$$\tilde{V}_m = F(\sigma) + e.$$

In the considered framework of the difference imaging, the noise is added to the input difference data.

In order to estimate the Signal-to-Noise Ratio in dB we can use the following formula

$$\text{SNR}(\tilde{V}_m) = 10 \log_{10} \left(\frac{\|V_m - E[V_m]\|_2^2}{\|V_m - \tilde{V}_m\|_2^2} \right) = \quad (6.1)$$

$$= 10 \log_{10} \left(\frac{\|V_m - E[V_m]\|_2^2}{\|e\|_2^2} \right) \quad (6.2)$$

where the numerator equals the variance of the voltage differences s_V^2 and the denominator equals the variance of the noise s_e^2 . Thus SNR represents the ratio between the standard deviation of the data with respect to the noise variation.

Therefore, for a fixed expected SNR value in dB the standard deviation of the noise s_e can be expressed in terms of percentage value of the standard variation of the data s_V . Fixing $\text{SNR}(\tilde{V}_m)$ and substituting $s_e = \kappa s_V$ in (6.2), we get to

$$\text{SNR}(\tilde{V}_m) = 10 \log_{10} \left(\frac{s_V}{s_e} \right)^2 = 10 \log_{10} \left(\frac{1}{\kappa} \right)^2 \quad (6.3)$$

and inverting for κ we obtain

$$\kappa = \sqrt{1 / (10^{\frac{\text{SNR}(\tilde{V}_m)}{10}})}. \quad (6.4)$$

Substituting (6.4) in $s_e = \kappa s_V$ we obtain the noise standard deviation in terms of input data measurements variation and the imposed $\text{SNR}(\tilde{V}_m)$ value:

$$s_e = \sqrt{\|\tilde{V}_m - E[V_m]\|_2^2 n_m / (10^{\frac{\text{SNR}}{10}})}. \quad (6.5)$$

Table 6.1 shows some correspondences between $\text{SNR}(\tilde{V}_m)$ and κ values.

$\text{SNR}(\tilde{V}_m)$	κ
30 dB	3.16 %
33.98 dB	2 %
40 dB	1 %
50 dB	0.32 %
60 dB	0.1 %

Table 6.1: Correspondence table for the percentage of standard deviation of the input signal and the SNR level.

In EIDORS `v1 = add_noise(SNR , v1 , v2)` assigns to `v1` the noise calculated from `std(v1-v2)` to match given SNR for the difference data.

6.2 Example 1: SAEiT₀ vs PDIPM

In this example we compare the PDIPM algorithm and proposed SAEiT model with null η -map (named SAEiT₀) on the PC-test without addition of noise. The aim is to show the power of this special setting of the proposed model in sparsity promoting and reconstruction of complex piecewise constant conductivity distributions. The data are simulated on the generic forward mesh (which will from now on be referred to as GFM) with 39488 triangles and 19937 nodes shown in Figure 6.1, while the reconstruction is performed on the same mesh that is used in Chapter 3.

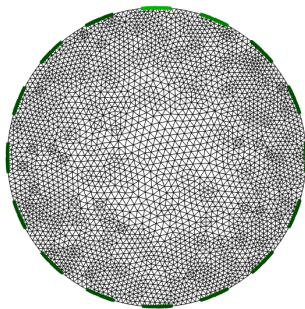


Figure 6.1: Generic Forward Mesh GFM

The benefits of choosing the proposed method can be seen in the reduced contrast loss, details loss and contour shrinkage that are gained thanks to the use of the nonsmooth nonconvex $\phi(t; a)$ function in the penalty term: the original conductivity values are indeed more accurately reconstructed as shown in Figure 6.3, the small circular shape is not completely flattened and the squared shape is not lost in favour of a more circular-like one. The reason behind these results is that TV allows for step changes but at the same time imposes on them a penalty that grows accordingly to their magnitude, which results in the introduction of intermediate step changes and reduced contrast. On the contrary, function $\phi(t; a)$ is identically equal to 1 from a certain t value, which means that all the highest step changes are equally

penalized or, equivalently, allowed.

ϵ_{slices}		ϵ_{sol}	
SAEiT	PDIPM	SAEiT	PDIPM
0.3115	0.3715	0.0663	0.0201

Table 6.2: **Example 1** Error Values

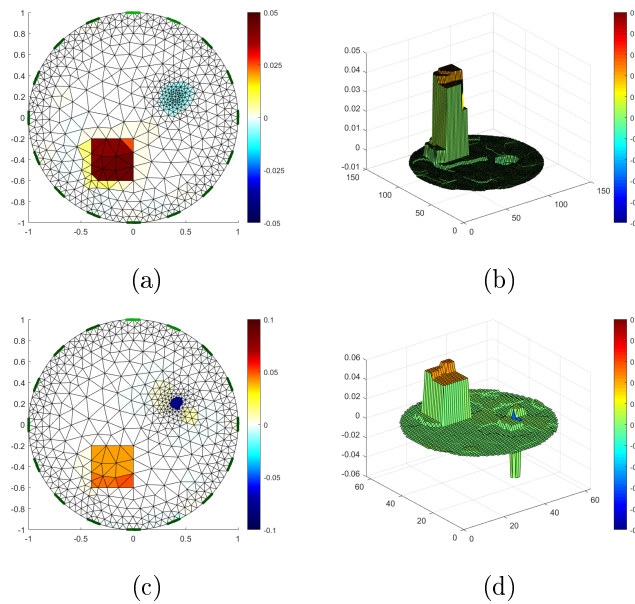


Figure 6.2: **Example 1**: SAEiT with $\eta = 0$ (named SAEiT₀) (c)-(d) behaves as TV-like- L_2 model which is compared with the TV- L_2 model implemented in the PDIPM method (a)-(b).

After showing the performance of the two algorithms on the usual setup with 16 electrodes, we now present how the choice of a different number of electrodes influences the solution: to this aim, the previous computation on the PC-test is repeated in a setting with 8 and 32 electrodes. The idea behind this example is that the more electrodes one introduces in the system, the more information is collected and, as a consequence, an enhancement in the resolution should be achieved. Yet, this holds true only when sufficient precision of the instrument is provided [19]. Furthermore, considering more electrodes translates into more measurements and therefore higher computational cost in solving the inverse problem.

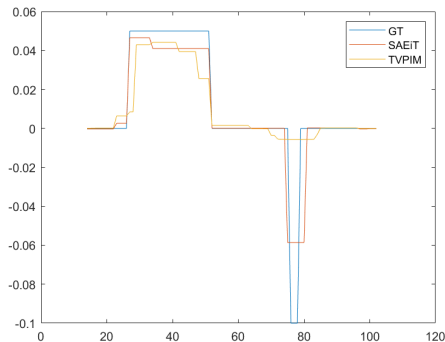


Figure 6.3: **Example 1:** 1D sections of the 3D surface reconstruction

Figures 6.4, 6.5 and 6.6 illustrate the reconstructions with the new electrode settings. The sensor array with 8 electrodes yields, as expected, a very poor solution that does not reproduce the original conductivity values and is not fit within the original shapes: both algorithms expanded and smoothed the contour of the positive squared conductivity variation and only reconstructed half of the height of the step change, while the small negative variation is only detected by SAEiT₀, but not properly reconstructed. The sensor array with 32 electrodes yields a good solution although not too much improvement is gained with respect to the 16 electrodes setup for the price of a higher computational cost, since the number of measurements sums up to 896 for a full measurement protocol with 32 electrodes, against 192 measurements with 16 electrodes, as reported in Table 2.2. In addition, a too high fidelity parameter in both algorithm results in the introduction of small artefacts in the reconstructed conductivity, as can be noticed in Figure 6.5. Table 6.3 updates table 6.2 with the error values for the setup with 8 and 32 electrodes.

6.3 Example 2: Benefit of η -map

The following group of examples is designed to show the ability of the proposed model with a space-variant η -map to reconstruct different and mixed

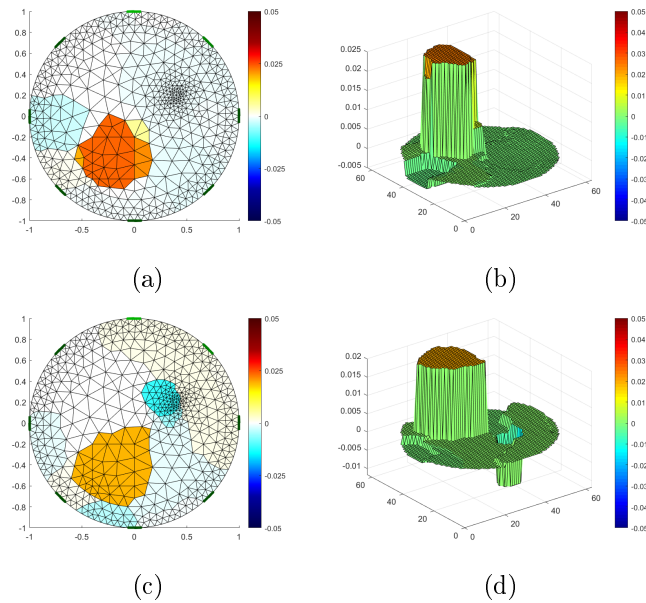


Figure 6.4: **Example 1**: PDIPM reconstruction of PC-test with 8 electrodes (a)-(b); SAEiT₀ reconstruction with 8 electrodes (c)-(d).

L	ϵ_{slices}		ϵ_{sol}	
	SAEiT	PDIPM	SAEiT	PDIPM
8	0.8298	0.7549	0.0131	0.0143
16	0.3115	0.3715	0.0663	0.0201
32	0.3596	0.4227	0.0216	0.0201

Table 6.3: **Example 1**: Error Values for different electrode numbers L

conductivity distributions. In this example we compare the PDIPM method and the proposed SAEiT method with a space-variant η map on the PCSM-test without addition of noise. The data are simulated on GFM, while the reconstruction is performed on an *ad hoc* mesh with 750 nodes and 1402 triangles. The space-variant η map illustrated in Figure 6.7 is obtained via a proper processing of the gradient of the reference solution obtained in a preliminary step of SAEiT₀.

The reconstruction shown in Figures 6.9(a)-(b) is from PDIPM and the

6. Numerical Experiments

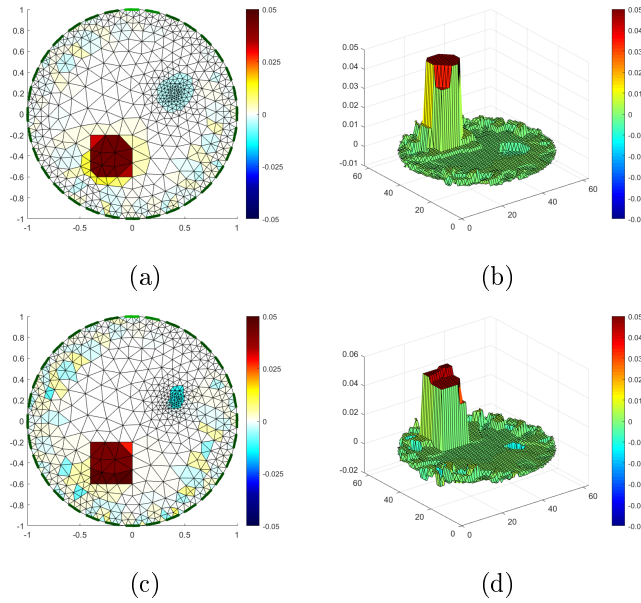


Figure 6.5: **Example 1**: PDIPM reconstruction of PC-test with 32 electrodes (a)-(b); SAEiT₀ reconstruction with 32 electrodes (c)-(d).

one in Figures 6.9(c)-(d) is from SAEiT. Clearly the proposed method performs better in reconstructing both the piecewise constant and the smooth conductivity variations: sparsification and contrast stretching are better achieved in the first case and smoothing in the second. Figure 6.8 shows in detail how well the contour of the piecewise constant inclusion are respected and the smooth decrease of the circular variation is reproduced, where PDIPM only allowed for two step changes.

ϵ_{slices}		ϵ_{sol}	
SAEiT	PDIPM	SAEiT	PDIPM
0.2747	0.3302	0.0545	0.0209

Table 6.4: **Example 2**: Error Values

We now assess the performance of the SAEiT algorithm with space-variant η -map for the same test but on a fine generic backward mesh with 2625 nodes and 5056 triangles. Results in Figure 6.12 show that even without

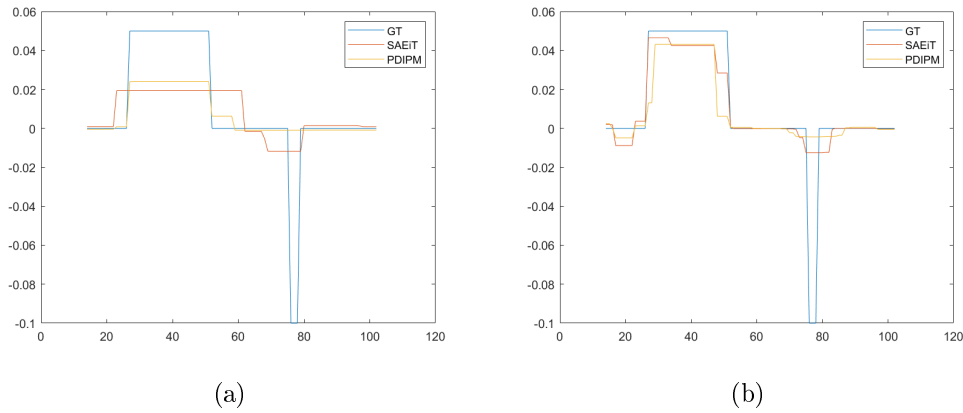


Figure 6.6: **Example 1**: 1D sections of the 3D surface reconstruction from a 8 (a) and 32 (b) electrodes EIT sensor array.

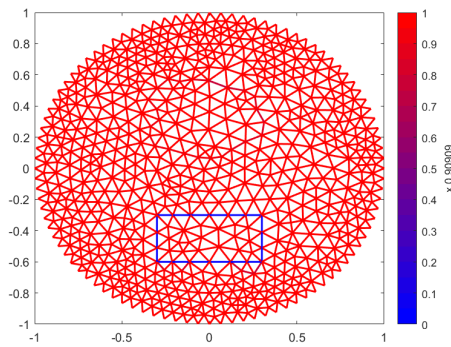


Figure 6.7: **Example 2**: Space-variant η -map.

prior information about the shape of the inclusions the algorithm is able to detect and differentiate them. Figures 6.12(a)-(b) show the projection of the ground truth on the backward mesh and Figures 6.12(c)-(d) show the SAEiT reconstruction: the piecewise constant inclusion is fit by the algorithm within a region that well reproduces the original rectangular shape, if one considers the inconsistent geometry of the mesh.

ϵ_{slices}	ϵ_{sol}
0.3667	06472

Table 6.5: **Example 2** with generic Backward mesh: Error Values

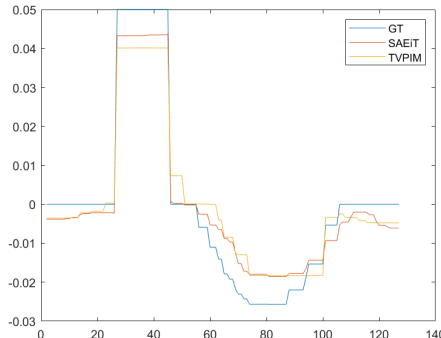


Figure 6.8: **Example 2:** 1D sections of the 3D surfac reconstruction.

6.4 Example 3: SAEiT $_{\alpha}$ vs IGNL

In this example we compare the IGNL algorithm which belongs to the class of EIT-NL-LR models and the proposed SAEiT method (which belongs to the class EIT-L-NLR) with a constant η -map with $\eta = \alpha$ on Ω , $\alpha \neq 1$, on a new version of the SM-test without addition of noise. We notice that η -map in this test would be 1 everywhere on Ω . The difference with SM-test in Chapter 4 is that the smooth features have a maximum resp. minimum point that is 0.013 higher resp. lower than scaffold level. The data are simulated on the same generic mesh as in the previous examples, while the reconstruction is performed on an ad hoc mesh with 1394 nodes and 2690 triangles.

The choice of a constant η -map aims to highlight the effect of the non-convex penalty term, which would otherwise be ignored: as previously described, when $\eta(x) \equiv 1$ for $x \in \Omega$, the proposed variational model reduces to a Tikhonov regularization. Figures 6.13(b)-(c) show the IGNL reconstruction, while Figures 6.13(e)-(f) show the result of SAEiT: the smooth behaviour of the inclusion is well reconstructed in both case, but the former method presents some oscillations in the background, while the latter method managed to flatten it. Furthermore, as shown in Figures 6.13(a)-(d), SAEiT reconstruction is slightly more precise than IGNL in retrieving the original conductivity values and this reflects in a significantly smaller *slices*

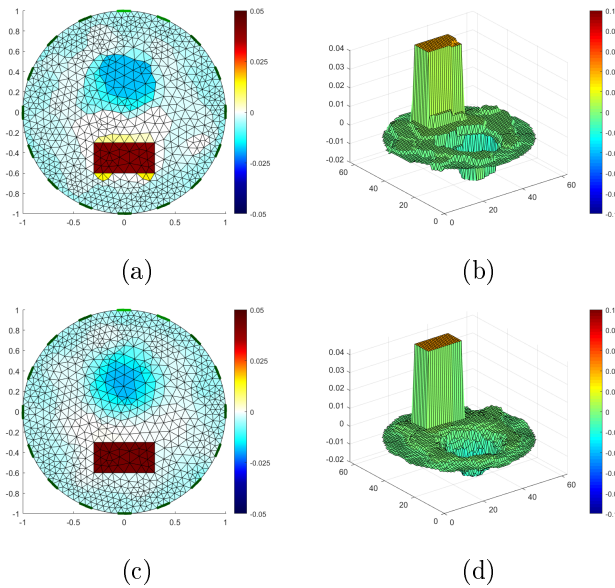


Figure 6.9: **Example 2**: PDIPM reconstruction (a)-(b); SAEiT reconstruction (c)-(d).

error value for SAEiT, as reported in Table 6.6.

ϵ_{slices}		ϵ_{sol}	
SAEiT	IGNL	SAEiT	IGNL
0.2377	0.3447	0.0454	3.0586e-05

Table 6.6: **Example 3**: Error Values

6.5 Example 4: Reconstruction of noisy data

In this example we compare the PDIPM method and the proposed SAEiT method with a space-variant η -map on the PCSM-test with addition of AWGN in the range $\{30 \text{ SNRdB}, 40 \text{ SNRdB}, 60 \text{ SNRdB}\}$. In Table 6.7 we report the standard deviation of the noise vector applied to the data for a given $\text{SNR}(\tilde{V}_m)$ value. We notice that higher values of SNR correspond to less degradation of the measured data. The data are simulated on the same generic mesh as in the previous example, while the reconstruction is

6. Numerical Experiments

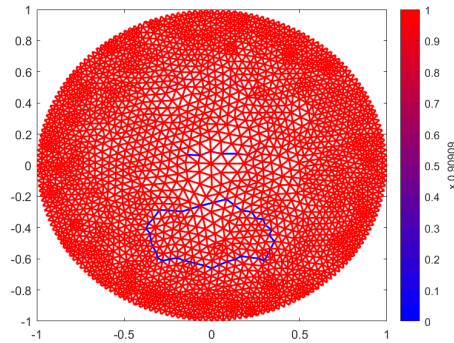


Figure 6.10: **Example 2** with Generic Backward Mesh: Space-variant η -map.

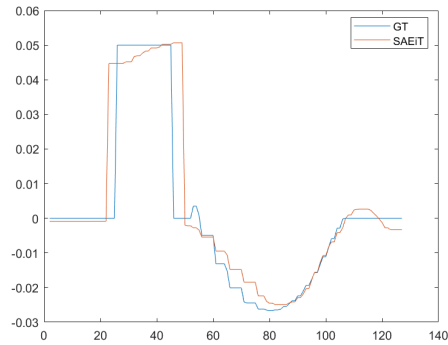


Figure 6.11: **Example 2**: with Generic Backward Mesh: 1D sections of the 3D surface reconstruction.

performed on the same mesh that is used in Chapter 3 for the considered test. The space variant η map is obtained via a proper processing of the gradient of the reference solution obtained in a preliminary step of SAEiT₀.

$\text{SNR}(\tilde{V}_m)$	30 dB	40dB	60 dB
s_e	8.0076e-04	2.5322e-04	2.5322e-05

Table 6.7: Standard deviation of AWGN for given SNR values

Results show that SAEiT can perform well even with noisy data in both recovering a proper η -map and successively reconstruct the conductivity dis-

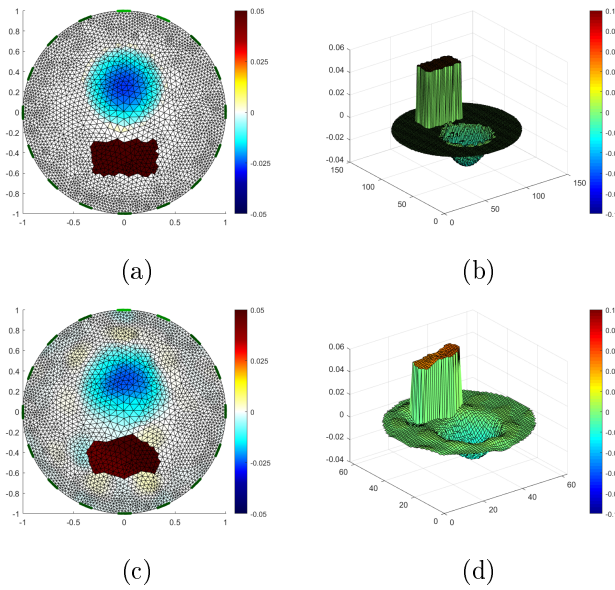


Figure 6.12: **Example 2**: with Generic Backward Mesh: GT projection on backward mesh (a)-(b); SAEiT reconstruction (c)-(d)

tribution. Error values are reported in Table 6.8: ϵ_{slices} for SAEiT increase in accordance with increasing noise level, but this can only be appreciated from the third decimal place, while PDIPM is significantly affected already on the second decimal place. It is also interesting to notice that even in case the edge detection procedure wrongly classifies some isolated edges, if they do not define a closed path (as shown in Figures 6.17-6.20), then the algorithm still manages to flatten the reconstruction in that area.

	ϵ_{slices}		ϵ_{sol}	
	SAEiT	PDIPM	SAEiT	PDIPM
60 dB	0.2795	0.3323	0.0548	0.0218
40 dB	0.2816	0.3764	0.0543	0.0205
30 dB	0.2832	0.4174	0.0543	0.0209

Table 6.8: **Example 4** with noisy data: Error Values

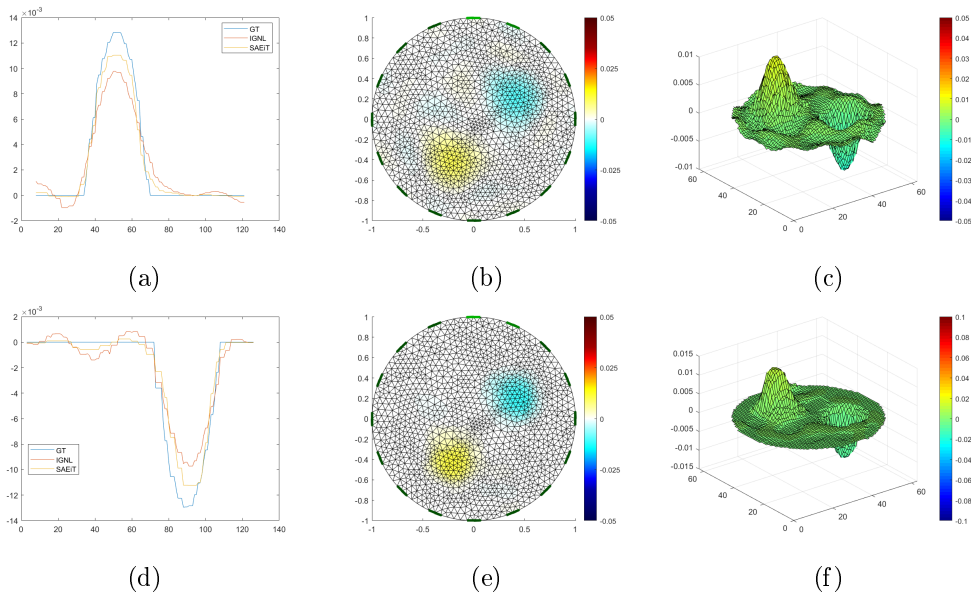


Figure 6.13: **Example 3**: 1D sections of the 3D surface reconstruction (a)-(d); IGNL reconstruction (b)-(c); SAEiT reconstruction with $\eta(x) = \alpha$ on Ω (e)-(f).

6.6 Example 5 - Image Fusion

In this example we show the performance of SAEiT with space variant η -map defined via the *Image Fusion Procedure* and compare it with the PDIPM method. Given an photograph of the experimental setup as shown in Figure 6.23a, the *Image Fusion Procedure* consists of the following steps:

- **Region Segmentation** of the interior of the tank to generate a labelling of the N regions inside the tank;
- **Edge detection** of the region inside the tank to generate closed contour curves of the regions $\mathcal{C} = \{C_s\}_{s=1}^N$;
- **Scaling** of the interior of the tank onto a unitary circle to construct the Backward Mesh;
- **Mapping** of \mathcal{C} onto the mesh to obtain the η -map, $\eta : \mathcal{E} \rightarrow [0, 1]$.

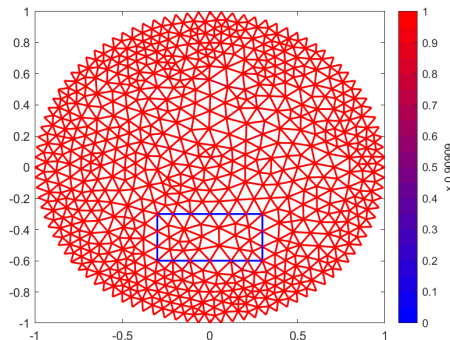


Figure 6.14: **Example 4 (60 dB Noise)**: Space variant η -map.

Figure 6.23a shows a tank with a sensor array of 16 electrodes and two inclusions, a hydrogel scaffold and a rubber triangle, immersed in a buffer for cell cultures that keeps the pH of the experiment under control; Figure 6.23b shows the segmented versions of Figure with three different labels for the background, the buffer solution and the inclusions; Figure 6.24 shows the contour curves of the regions inside the tank generated after the edge detection procedure on the segmented image.

Figures 6.25a and 6.25b show two different *ad hoc* meshes obtained from Figure 6.23b which are used for the simulation of the synthetic voltage measurement data and the reconstruction of the conductivity variation distribution with respect to the empty tank. The Forward Mesh is made of 6253 nodes and 12312 triangles, while the Backward Mesh contains 1301 nodes and 2504 triangles. Figure 6.26 shows an example of the space variant η -map.

The simulation was conducted considering an EIT array sensor with 16 electrodes and an injected current with intensity 0.1 A ; the background conductivity was set to 1.1 Sm^{-1} , the rubber triangle was assigned 1.05 Sm^{-1} so that it represented a downward jump in conductivity and the scaffold a smoothly increasing conductivity up to 1.1267 Sm^{-1} because in a realistic experiment with cell colonies, cells more likely populate the boundary due to

6. Numerical Experiments

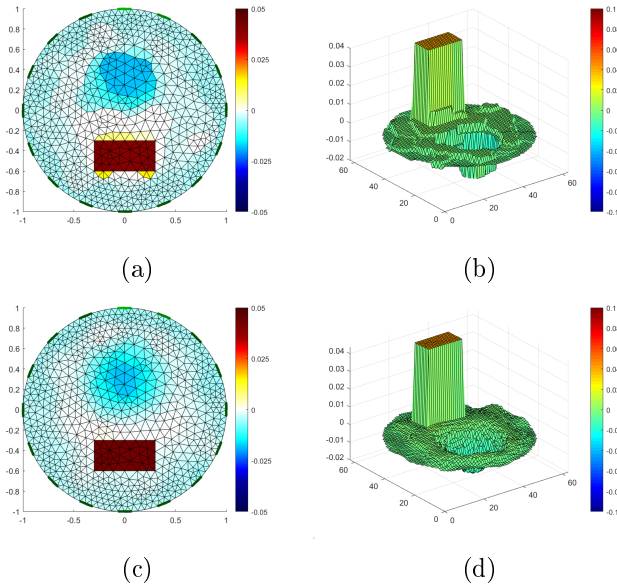


Figure 6.15: **Example 4 (60 dB Noise)**: PDIPM reconstruction (a)-(b); SAEiT reconstruction (c)-(d)

the presence of nutrients in the liquid solution, while the interior experiences some metabolic stress (low oxygen, low nutrients) that limits mineralization. The space variant η -map was defined as equal to zero on the boundary of the inclusions and the rest of the edges got a constant value $\alpha = 0.5$, as shown in Figure 6.26.

Results in Figure 6.28 show that both methods perform well in general, as long as shape and average behaviour are considered, but a more detailed analysis reveals that PDIPM generates some artifacts around the rubber triangle and completely flattens the variation inside the scaffold, while SAEiT reconstructs a clean step variation in the first case and a smooth increase in the second. This precision translates into a low ϵ_{slices} value for SAEiT as reported in Table 6.9.

ϵ_{slices}		ϵ_{sol}	
SAEiT	PDIPM	SAEiT	PDIPM
0.1605	0.2753	0.0683	0.0255

Table 6.9: **Example 5** Error Values

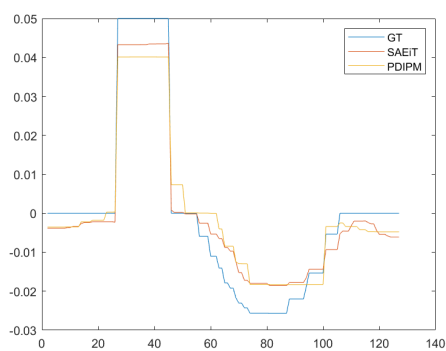


Figure 6.16: **Example 4 (60 dB Noise)**: 1D sections of the 3D surface reconstruction.

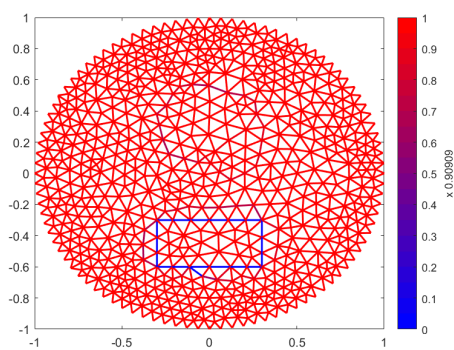


Figure 6.17: **Example 4 (40 dB Noise)**: Space variant η -map.

6. Numerical Experiments

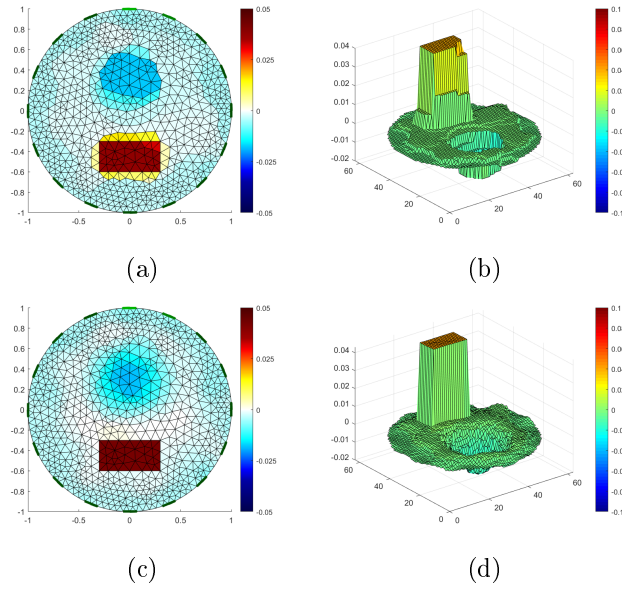


Figure 6.18: **Example 4 (40 dB Noise)**: PDIPM reconstruction (a)-(b);SAEiT reconstruction (c)-(d)

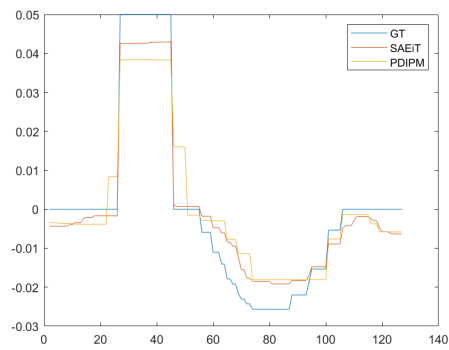


Figure 6.19: **Example 4 (40 dB Noise)**: 1D sections of the 3D surface reconstruction.

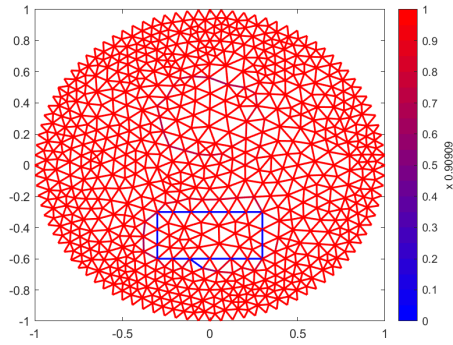


Figure 6.20: **Example 4 (30 dB Noise)**: Space variant η -map.

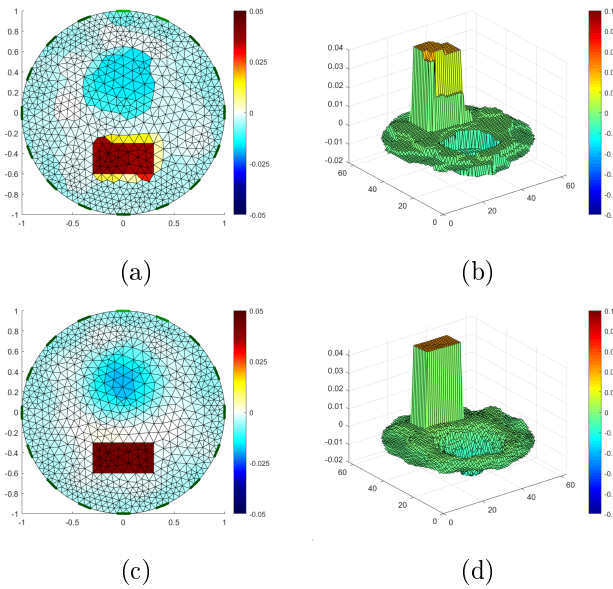


Figure 6.21: **Example 4 (30 dB Noise)**: PDIPM reconstruction (a)-(b); SAEiT reconstruction (c)-(d)

6. Numerical Experiments

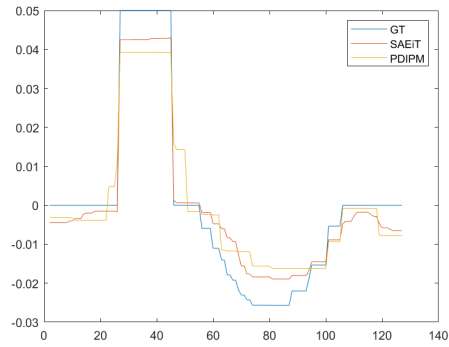


Figure 6.22: **Example 4 (30 dB Noise)**: 1D sections of the 3D surface reconstruction

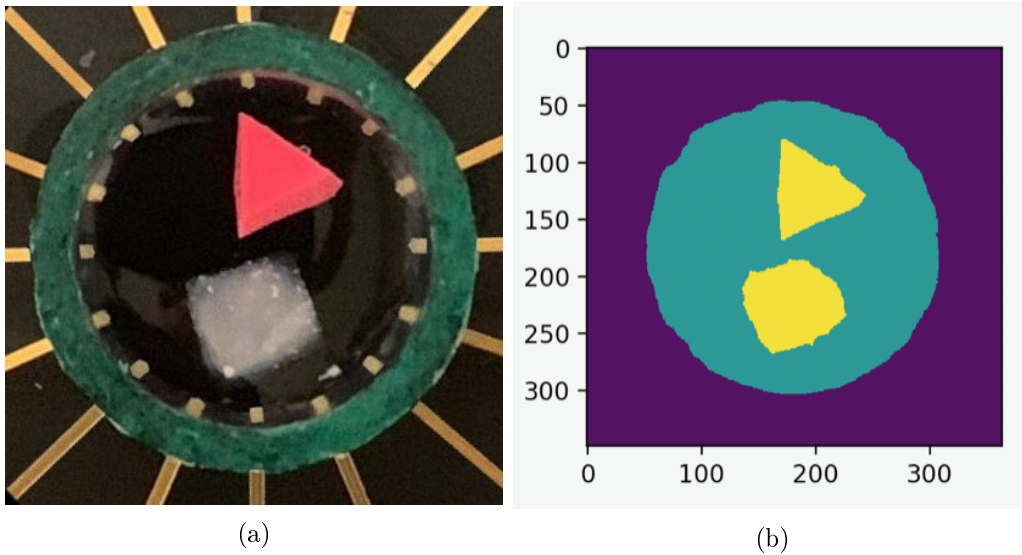


Figure 6.23: **Example 5** EIT tank with an 16 electrodes sensor array and 2 inclusion (a); segmented image (b).

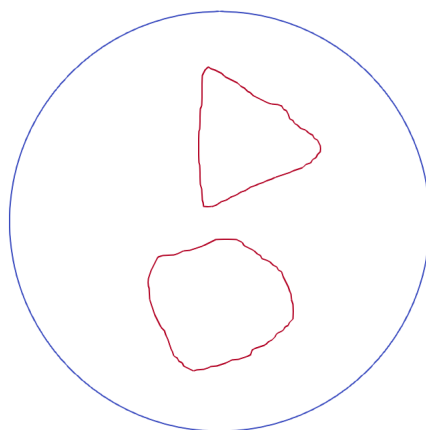


Figure 6.24: **Example 5**: Detected contours of the regions inside the tank.

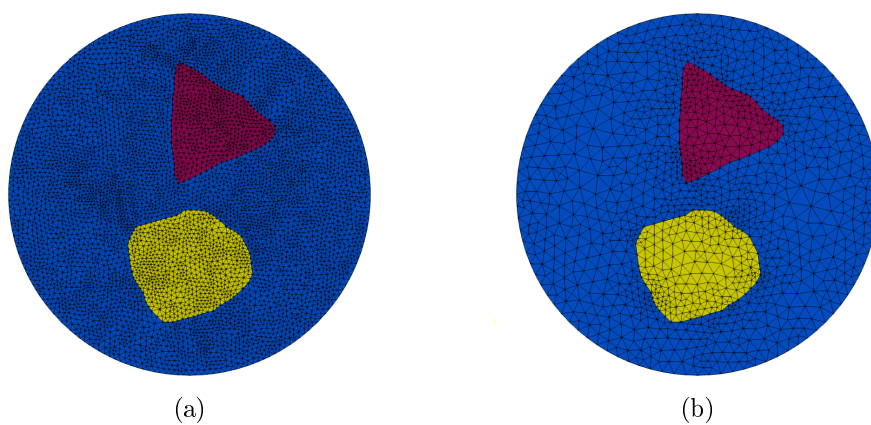


Figure 6.25: **Example 5**: Image Fusion Forward (a) and Backward (b) meshes.

6. Numerical Experiments

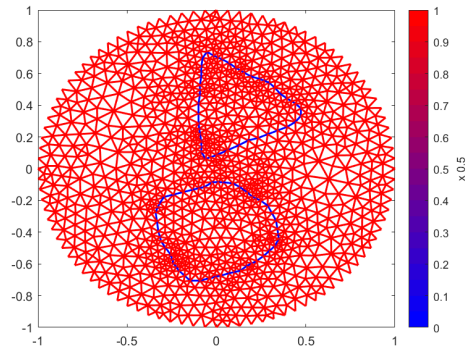


Figure 6.26: **Example 5:** Space variant η -map (a) from Image Fusion procedure.

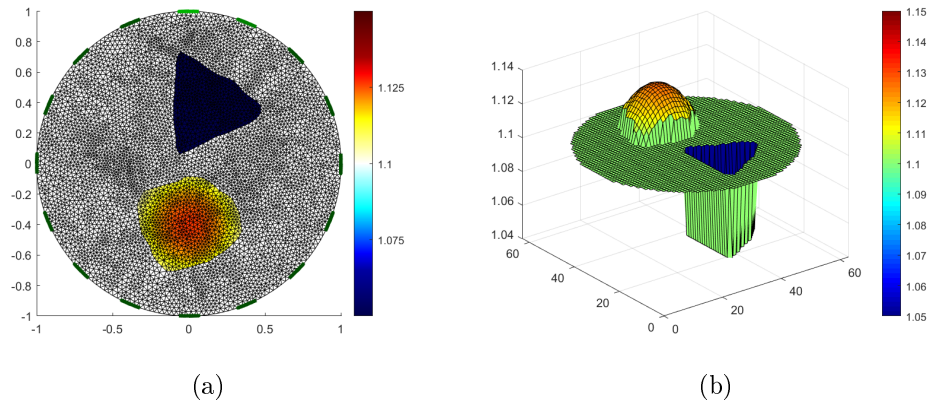


Figure 6.27: **Example 5:** Simulated data for the Forward problem.

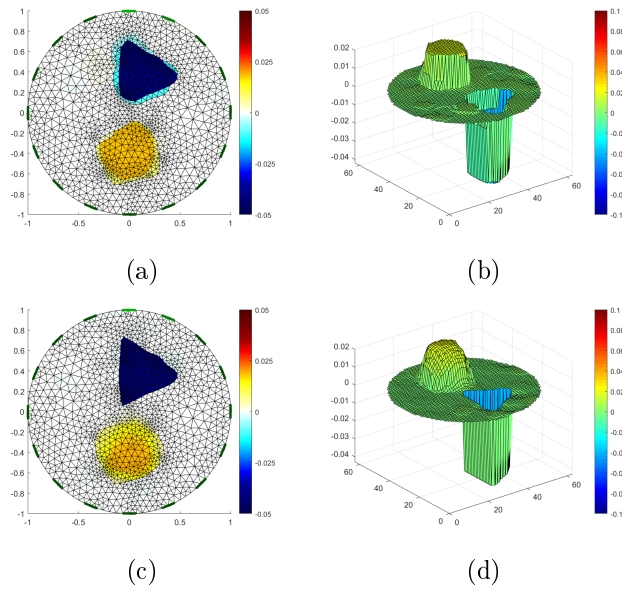


Figure 6.28: **Example 5**: PDIPM reconstruction (a)-(b); SAEiT reconstruction (c)-(d)

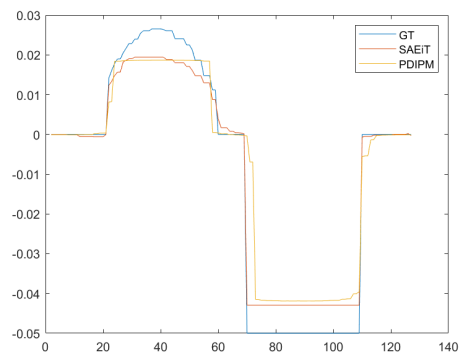


Figure 6.29: **Example 5**: 1D sections of the 3D surface reconstruction (b).

Conclusions

In this work the inverse problem of Electrical Impedance Tomography was investigated. In the first chapter, a brief summary of the history of the problem and its applications is presented, from the early studies of the distribution of electrical potentials inside layers of ground until the most recent employments in biomedical engineering.

In the second chapter we described the mathematical models for both the forward and the inverse problem. In particular we firstly presented the construction of the Complete Electrode Model and the conditions that ensure the uniqueness of the solution in this framework. Secondly, we described different regularization models for the inverse problem and classified them according to the linearity or nonlinearity of the fidelity (EIT-L/EIT-NL) and of the penalty (LR/NLR) term.

In the third chapter we showed the discretization of the spatial domain and of the models and different numerical methods to address the inverse problem which are implemented in EIDORS software , while in the fourth chapter we tested and compared the performance of the aforementioned methods for the recovery of various conductivity distribution. We concluded that on a general scale the TV based Primal Dual Interior Point Method (PDIPM) is the most accurate among the considered ones.

In the fifth chapter we proposed a new variational method for EIT inverse

problem with a spatially adaptive mixed penalty term (SAEiT), which includes a smoothing L_2 generalized Tikhonov regularization operator and a nonsmooth nonconvex TV-like sparsity promoting operator based a rescaled and reparameterized version of the minmax concave penalty function $\phi(t; a)$, as the aim is to jointly reconstruct both the piecewise constant regions and the smooth regions, according to an adaptive map. The particular choice for the nonconvex operator has the advantage over canonical TV of equally penalizing the highest step changes (function ϕ is identically equal to 1 from a certain t value that depends on the *concavity parameter* a) while, on the contrary TV penalizes step changes accordingly to their magnitude and this introduces intermediate steps and causes a reduction in contrast reconstruction. We successively showed how to define an edge-based space-variant trade-off between the penalties, depending on the amount of information that is provided on the experimental setup, and outlined an ADMM-based algorithm for the resolution of the minimization problem.

In the sixth chapter we compared the performance of SAEiT and other methods from the ones described in Chapter 3 on various conductivity distribution (smooth, piecewise constant and mixed) both with and without additive white gaussian noise. Quantitative and qualitative results showed the higher degree of accuracy of the SAEiT reconstructions, especially in case of mixed conductivity distributions, and stronger robustness against noisy data.

Ringraziamenti

Rivolgo un sincero ringraziamento alla professoressa Morigi per avermi dato la possibilità di realizzare questa tesi in un ambito ricco di stimoli dal punto di vista matematico e delle applicazioni: sono felice che abbia aperto i miei orizzonti sul ruolo giocato dalla matematica nella ricerca scientifica, in particolar modo quella biomedica. La ringrazio per la continua disponibilità e professionalità mostratami e per i costanti incoraggiamenti, grazie ai quali mi è ora più semplice pensare libero chi sarò.

Ringrazio Martin per l'interesse che ha dimostrato per questo lavoro, per il tempo dedicatomi, per le nuove idee, per i chiarimenti, le dritte, i consigli e per gli insegnamenti che ho tratto da questi mesi di collaborazione con lui. Ringrazio Andrea per aver proposto questo progetto sull'EIT e per l'entusiasmo davanti ad ogni nuova proposta, sfida o nuovo traguardo raggiunto.

Ringrazio la mia famiglia, mamma papà Checco e Robi, le zie e la nonna, per avermi sempre accompagnato in questi anni, per avermi sostenuto nelle mie scelte e avermi permesso di percorrere tutte le strade che ho ritenuto importanti per il raggiungimento dei miei obiettivi e per il perseguimento dei miei ideali.

Ringrazio la mia famiglia svedese, Maria Hans Nadja e Georg, per il legame che si è creato e abbiamo coltivato insieme in questi anni e per il sincero interesse e supporto per le mie scelte di vita: Tack, det är underbart att ni är en del av mitt liv.

Ringrazio gli amici di sempre, Poli Rita Ingrid Sam e Apo, perchè ogni traguardo personale con voi diventa un traguardo condiviso, vi ringrazio per le nuove prospettive che siete in grado di aprirmi sul mondo, per i discorsi infinti in cui ci perdiamo e lo scandaloso senso di libertà di cui godo quando sono insieme a voi.

Ringrazio Nunzia Nicco Greta e Ennio per la magia che ci lega e ci tiene uniti

Ringraziamenti

ovunque ci troviamo dispersi nel mondo e per l'influenza positiva e motivazionale che le vostre vite hanno sulla mia.

Ringrazio Bologna per essere stata la città perfetta in cui crescere e formarmi, ma soprattutto per aver permesso che il mio destino incrociasse quello di chi in un modo o nell'altro si è ritagliato uno spazio speciale nella costellazione dei miei affetti: grazie Michele per esserti dimostrato molto più che un coinquilino e per la positività che la tua compagnia trasmette; grazie Ste perchè mi insegni ogni giorno nuovi modi per cogliere ed amare la bellezza in quello che mi circonda; grazie Giuli per essere un'inesauribile fonte di stimoli e una fidata compagna di (dis)avventure; grazie Marghe per la contagiosità della tua energia e curiosità e per essere stata un'infaticabile e insostituibile compagna di studio; grazie Ele Cla Chia Ceci Ale e tutti gli amici di VPC per esservi rivelati una grande famiglia in cui non sono mai mancati senso di protezione e intrattenimenti; grazie Franci per la tua dolcezza e per l'esperienza condivisa dell'Erasmus che nell'allontanarci ci ha uniti.

Ringrazio Bergen per avermi riportato in Scandinavia, per la sua malinconica bellezza nei giorni di pioggia e la sua vivacità nei giorni di sole, per avermi fatto riscoprire il contatto con la natura e avermi regalato tre ineguagliabili (e insopportabili) compagne di viaggio come Marghe Chiarina e Chia.

Grazie infine a tutti coloro che hanno condiviso momenti insieme a me in questi anni, speciali o gloriosamente banali che essi fossero.

*"E hai visto all'improvviso è arrivato il futuro
E adesso sono qui
É un superpotere essere vulnerabili.
Sono al di là della paura
In quella prateria infinita
Piena di pericoli, strapiena di vita."*

Bibliography

- [1] A. Adler, T. Dai, W. R.B. Lionheart, "Temporal Image Reconstruction in Electrical Impedance Tomography", *Physiol. Meas.*, pp. 1-11, 2007
- [2] A. Adler, R. Gaburro, W. Lionheart, "Electrical Impedance tomography", in *Handbook of Mathematical Methods in Imaging*, 2nd ed., O. Scherzer (Ed), Springer, 2016
- [3] A. Adler, R. Guardo, "Electrical Impedance Tomography: Regularized Imaging and Contrast Detection", *IEEE Trans. Medical Imag.*, vol. 15, pp. 170-179, 1996
- [4] A. Adler, W. R. B. Lionheart, "Uses and abuses of EIDORS: An extensible software base for EIT", *Physiol. Meas.*, vol. 27, no. 5, pp. 25-42, 2006
- [5] R. H. Bayford, "Bioimpedance Tomography (Electrical Impedance Tomography)", *Annual Review of Biomedical Engineering*, vol. 8, pp. 63-91, 2006
- [6] A. Blake, A. Zisserman, *Visual Reconstruction*, MIT Press, 1987
- [7] L. Borcea, "Electrical Impedance Tomography", *Inverse Problems*, vol. 18, no. 6, 2002
- [8] A. Borsic, "Regularisation Methods for Imaging from Electrical Measurements", *PhD Thesis*, School of Engineering, Oxford Brookes University, UK, 2002

BIBLIOGRAPHY

- [9] A. Borsic, B. M. Graham, A. Adler, W. R. B. Lionheart, "Total Variation Regularization in Electrical Impedance Tomography", 2007
- [10] A. Borsic, B. M. Graham, A. Adler, W. R. B. Lionheart, "In Vivo impedance imaging with total variation regularization", *IEEE T Medical Imaging*, vol. 29, pp. 44-54, 2010
- [11] M. Botsch, L. Kobbelt, M. Pauly, P. Alliez, B. Lévy, *Polygon Mesh Processing*, A K Peters/CRC Press, 2010
- [12] F. Braun, M. Proenca, J. Sola, J. Thiran, A. Adler, "A Versatile Noise Performance Metric for Electrical Impedance Tomography Algorithms", *IEEE Transactions on Biomedical Engineering*, vol. 64, no. 10, pp. 2321-2330, 2017
- [13] B. H. Brown, A. D. Seager, "The Sheffield data collection system", *Clin. Phys. Physiol. Meas.*, vol. 9, pp. 91-97, 1987
- [14] A. P. Calderón, "On an inverse boundary value problem", *Seminar on Numerical Analysis and its Applications to Continuum Physics*, Rio de Janeiro, Editors W. H. Meyer and M. A. Raupp, Sociedade Brasileira de Matematica, pp. 65-73, 1980
- [15] M. Cheney, D. Isaacson, J.C. Newell, S. Simske, J. Goble, "NOSER: An Algorithm for Solving the Inverse Conductivity Problem", *Int. J. Imag. Syst. Technol.*, vol. 2, pp. 65-75, 1990
- [16] M. Cheney, D. Isaacson, C. Newell, "Electrical Impedance Tomography", *SIAM Review*, vol. 41, No. 1, pp. 85-101, 1999
- [17] M. Cortesi, A. Samorè, J. Lovecchio, S. Morigi, E. Giordano, "EIT for tissue engineering applications: a case for osteogenic differentiation", *20th International Conference on Biomedical Applications of Electrical Impedance Tomography (EIT 2019)*, London, UK

-
- [18] C. Gómez-Laberge, A. Adler, "Direct EIT Jacobian calculations for conductivity change and electrode movement", *Physiol. Meas.*, vol. 29, no. 6, 2008
- [19] D. S. Holder, *Electrical Impedance Tomography: Methods, History and Applications*, Institute of Physics Publishing: London, U.K., 2005
- [20] M. Huska, A. Lanza, S. Morigi, F. Sgallari, "Convex Non-Convex Segmentation of Scalar Fields Over Arbitrary Triangulated Surfaces", *Journal of Computational and Applied Mathematics*, vol. 349, pp. 438-451, 2019
- [21] A. Lechleiter, A. Rieder, "Newton regularizations for impedance tomography: a numerical study", *Inverse Problems*, vol. 22, 2006
- [22] N. Lesparre, A. Adler, D. Gibert, F. Nicollin, "Electrical impedance tomography in geophysics, application of EIDORS", *Proc. EIT*, pp. 1-4, 2011
- [23] P. Linderholm, T. Braschler, J. Vannod, Y. Barrandon, M. Brouard, O. Renaud, "Two-dimensional impedance imaging of cell migration and epithelial stratification", *Lab Chip*, vol. 6, pp 1155-1162, 2006
- [24] W. R. B. Lionheart, "Review: Developments in EIT reconstruction Algorithms: pitfalls, challenges and recent developments", *Physiol. Meas.*, vol. 25, pp. 125-142, 2004
- [25] W.R.B. Lionheart, K. Paridis, "Finite Elements and Anisotropic EIT reconstruction", *Journal of Physics: Conference Series*, vol. 224, 2010
- [26] Y. Mamatjan, A. Borsic, D. GURSOY, A. Adler, "An experimental clinical evaluation of EIT imaging with l^1 data and image norms", *Physiol Meas.*, vol. 34, no.9, 2013
- [27] J. Nocedal, S. J. Wright, *Numerical optimization* (2nd ed.), Berlin, New York: Springer-Verlag, 2006

BIBLIOGRAPHY

- [28] N. Polydorides, W. R. B. Lionheart, "A Matlab toolkit for three-dimensional electrical impedance tomography: a contribution to the Electrical Impedance and Diffuse Optical Reconstruction Software project", *Meas. Sci. Technol.*, vol. 13, 2002
- [29] J. K. Seo, E. J. Woo, *Nonlinear Inverse Problems in Imaging*, John Wiley and Sons, 2012
- [30] Y. Shi, X. Zhang, Z. Rao, M. Wang, M. Soleimani, "Reduction of Staircase Effect With Total Generalized Variation Regularization for Electrical Impedance Tomography", *IEEE Sensors Journal*, vol. 19, no. 21, 2019
- [31] E. Somersalo, M. Cheney, D. Isaacson, "Existence and uniqueness for electrode models for electric current computed tomography", *SIAM J. Appl. Math.*, vol. 52, pp. 1023-1040, 1992
- [32] S. Stefanescu, C. Schlumberger, M. Schlumberger, "Sur la distribution électrique potentielle autour d'une prise de terre ponctuelle dans un terrain à couches horizontales, homogènes et isotropes", *J. Phys. Radium*, Vol 1, no. 4, pp. 132-140, 1930
- [33] D. R. Stephenson, J. L. Davidson, W. R. B. Lionheart, B. D. Grieve, T. A. York, "Comparison of 3D Image Reconstruction Techniques using Real Electrical Impedance Measurement Data", *4th World Congress on Industrial Proceedings Tomography*, pp. 1-8, 2005
- [34] M. Vauhkonen, W. R. B. Lionheart, L. M. Heikkinen, P. J. Vauhkonen, J. P. Kaipio, "A Matlab package for the EIDORS project to reconstruct two-dimensional EIT images", *Physiol. Meas.*, vol. 22, pp. 107-111, 2010
- [35] M. Vauhkonen, D. Vadász, P. A. Karjalainen, E. Somersalo, J. P. Kaipio, "Tikhonov regularization and prior information in electrical impedance tomography", *IEEE Trans. Med. Imag.*, vol. 17, no. 2, pp. 285-293, 1998

- [36] J. G. Webster, *Wiley Encyclopedia of Electrical and Electronics Engineering*, John Wiley and Sons, 2010
- [37] C. H. Zhang, "Nearly unbiased variable selection under minimax concave penalty", *Annals of Statistics*, vol. 38, no. 2, pp. 894-942, 2010
- [38] H. Wu, W. Zhou, Y. Yang, J. Jia, P. Bagnaninchi, "Exploring the Potential of Electrical Impedance Tomography for Tissue Engineering Applications", *Materials*, vol. 11, no. 6, 2018